Hall A Annual Report - 2009

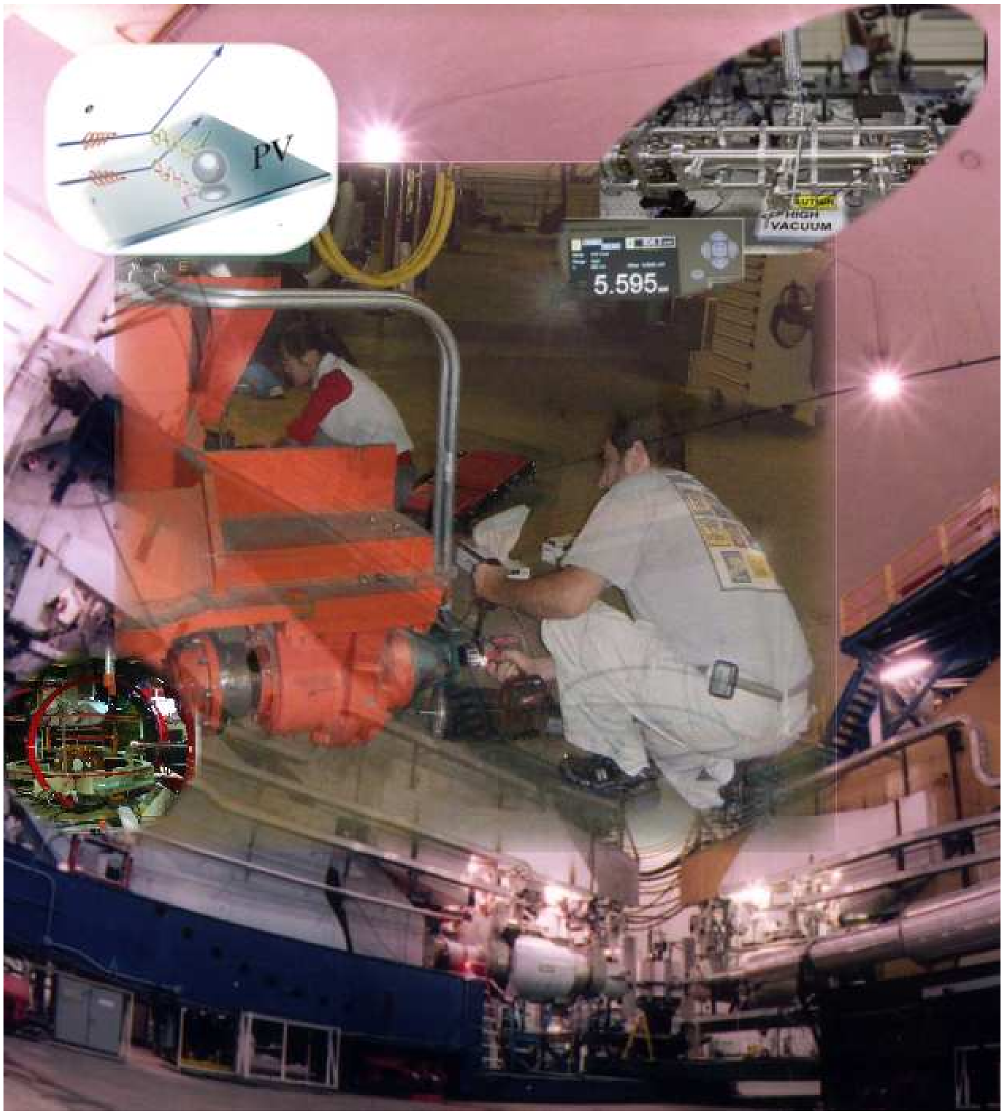

Edited by Kees de Jager and Guy Ron

Contents

List of Figures

1 Introduction

In the first half of 2009 we successfully completed the running of the BigFamily, a series of experiments that used the polarized ^{3}He target, most of the time in conjunction with the BigBite spectrometer. First we ran the second part of E06-010, the neutron transversity experiment, with E07-013, a measurement of the target SSA in DIS to study two-photon exchange effects, running parasitically. This was followed, after a brief reconfiguration, by E06-014, an accurate measurement of d_2^n, again with the target polarized transversely. Then, in a four-week down in March/April, BigBite was moved back over the right HRS, in the so-called Big Hop, a truly impressive accomplishment in such a short time. Thanks to the required running budget becoming available, the remaining three BigFamily experiments were run, all studying quasi-elastic scattering. The first, E05-015 studied two-photon effects in the target SSA with E08-005 running parasitically to extract information on the final-state interaction in the ^{3}He$(e,e'n)$ reaction. Finally, E05-102 will provide detailed understanding of the three-body ground-state wave-function. By utilizing the small Hall A neutron detector HAND, this experiment will also yield a highly accurate measurement on the neutron charge form factor G_E^n.

In the summer down the polarized target and the BigBite spectrometer were removed and the Hall was returned to its basic configuration of the two HRSs in combination with the cryotarget. In the fall two parity-violation experiments were run, E05-109 (HAPPEx-III), a measurement of the strange form factor of the proton at 0.6 GeV^2, and E08-011, a measurement of parity violation in deep-inelastic scattering. Both experiments obtained between 70 and 80% of the scheduled production data, mainly due to difficulties in producing parity-quality beam.

In 2009 essential progress was made with the research program in Hall A with the 12 GeV upgrade. Hall A now has seven fully approved and three conditionally approved proposals for the 12 GeV upgrade. For the upcoming PAC35 six proposals and three Letters of Intent have been submitted. For the SuperBigBite (SBS) project a funding proposal was submitted to DOE in November by a group of eight universities, including Norfolk State University, the University of Virginia and the College of William and Mary, and Jefferson Lab. The funding proposal was then sent out by DOE for a mail review of the quality of the physics, while a second Technical Review is being prepared by JLab. The MOLLER experiment to study parity violation in scattering of longitudinally polarized 11 GeV electrons from the atomic electrons in a liquid hydrogen target (Møller scattering) will be subjected to a Director's Review on January 14 and 15. The PVDIS experiment to measure A_{PV} in the deep-inelastic scattering of polarized electrons to high precision in order to search for physics beyond the Standard Model in lepton-quark neutral current interactions was conditionally approved at PAC34 and has been resubmitted for PAC35.

I would like to recognize the expertise, dedication and just plain hard work that made all this possible, by the design and engineering staff, Al Gavalya, Susan Esp, Joyce Miller, Macon Hodges and Paul Brindza and the technical staff Ed Folts, Jack Segal, Heidi Fansler, Scot Spiegel, Todd Ewing and Gary Dezern. Scot decided halfway through the year to transfer to Hall D and we wish him success in his new position. We welcome Howard Smith and David Galinski as valuable additions to Ed's staff.

2 General Hall Developments

2.1 The Compton Polarimeter Upgrade

(Contributed by Sirish Nanda)

2.1.1 Overview

The Hall A Compton Polarimeter provides electron beam polarization measurements in a continuous and non-intrusive manner via Compton scattering of polarized electrons from polarized photons trapped in a Fabry-Perot cavity. A schematic lay-out of the Compton polarimeter is shown in Fig. 1. The electron beam is transported through a vertical magnetic chicane consisting of four dipole magnets. At present, a high-finesse Fabry-Perot cavity built by CEA Saclay serves as the photon target. The Saclay cavity achieves an intra-cavity gain of about 1500. Injected with a 750 mW, 1064 nm infrared laser after accounting for beam transport and cavity coupling losses, the present cavity achieves power of about 900 W. The Compton back-scattered photons are detected in an electromagnetic calorimeter consisting of lead tungstate crystals. The recoil electrons, separated from the primary beam by the fourth dipole of the chicane are detected in a silicon micro-strip detector. The electron beam polarization is deduced from the counting-rate asymmetries of the detected particles.

The Saclay design is capable of 1-2% accuracy in determining the electron beam polarization over an energy range of 3 to 6 GeV. In order to boost the accuracy to 1% or better over a broader energy range of 1 to 11 GeV the Hall A Compton Polarimeter is undergoing an upgrade.

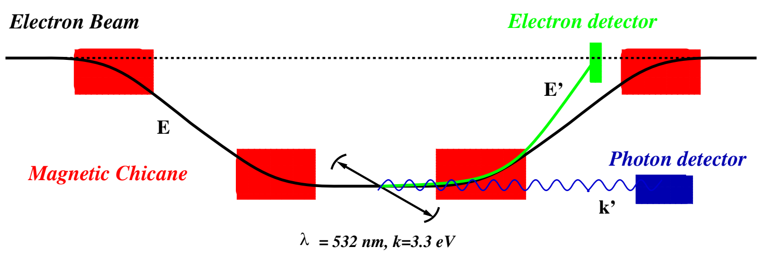

Figure 1: Schematic layout of the Hall A Compton polarimeter.

2.1.2 Upgrade

In addition, improvements to the electron detector and photon calorimeter combined with the development of a new integrating data acquisition method shows promise of absolute accuracies approaching 1% at 0.85 GeV beam energy. The main parameters of the green Compton upgrade are shown in Table 1.

Parameter	Present	Upgrade
Wavelength [nm]	1064	532
Cavity Power [W]	900	1500
FOM (σ.A^2) @0.85Gev	0.57	2.2
Energy Range [GeV)]	3 - 6	0.8 - 11
δP$_e$/P$_e$ @0.85Gev	-	1%

Table 1: Main design parameters of the green Compton polarimeter upgrade compared to the present infrared system

The conceptual design of the green Compton polarimeter utilizes much of the the existing infrastructure of the present Compton polarimeter. In the following, the subsystems being upgraded are described.

2.1.3 Electron Detector

The electron detector upgrade is being carried out by Laboratoire de Physique Corpusculaire IN2P3/Université Blaise Pascal (Clermont-Ferrand). The new detector has 4 planes of 192 silicon micro-strip with a 240 μm pitch. The expected resolution is about 100 μm. A high-precision vertical motion of 120 mm for the detector has been incorporated in the design to facilitate covering the recoil electrons corresponding to the Compton edge over a broad range of energies. The electron detector as well as its support structure and vacuum chamber were fabricated and later assembled at Clermont-Ferrand in early 2008. The package was delivered to Jefferson Lab in the summer of 2008. Installation of the new detector in the Hall A beam line was carried out by a team visiting from Clermont-Ferrand and Jefferson Lab engineering services group during August-September 2008. Several difficulties were encountered during installation of the electron detector vacuum chamber, in particular concerning vertical clearance of the mechanical structures from the nominal electron beam orbit. The CEBAF electron beam was successfully transported through the Compton chicane at 5.9 GeV through the new installation in October 2008. Detecting Compton scattered electron in the new

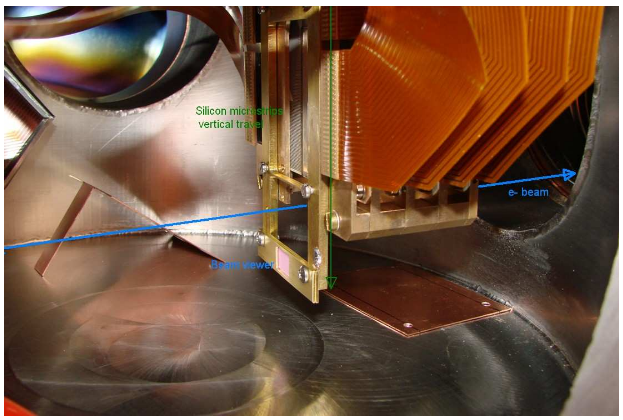

Figure 2: The silicon microstrip electron detector inside the vacuum chamber along with the additional Chromax beam viewer.

detector proved to be elusive in early 2009 due to the uncertainty in the position of the detector from the primary beam in the dispersive plane. In April 2009, a Chromax beam viewer target. 27 mm below the silicon microstrip detectors was installed in order to ascertain the position of the micro-strips relative to the electron beam. Illustrated in Fig. 2 is the beam viewer with respect to the silicon microstrip detector planes. As shown in Fig. 3, the electron beam was successfully transported to hit this viewer revealing nearly perfect horizontal alignment, but a 4 mm vertical offset for the detector. Armed with precise knowledge of the position of the electron detector, the first Compton-scattered electron spectrum was obtained with the new detector in late April 2009. Shown in Fig. 4 are the count rates observed in the third plane of the electron detector with the 1064 nm laser on (red) and off (black). A clear Compton edge is observed at microstrip number 14, corresponding to the expected position of the edge for 3 GeV electrons. However, the detection efficiency of the micro-strips was found to be poor, at about 10-20%. Further details of the commissioning effort are given in Section 2.2.

2.1.4 Photon Detector

The new photon detector consists of a single GSO crystal, 60 mm in diameter and 150 mm in length. The GSO crystal was delivered by Hitachi Chemicals Ltd. to Carnegie Mellon University (CMU) in 2008. The compete photon calorimeter as shown in Fig. 5, was put together at CMU led by Gregg Franklin.

The GSO calorimeter was installed in the Hall A beam line in November 2008. Commissioning of the detector with the existing Compton Polarimeter DAQ in counting mode, as well as the Flash ADC based integrating DAQ continued in 2009. A preliminary spectrum of Compton-scattered photons from 5.9 GeV polarized electron beam obtained with the detector is shown in Fig. 6. The spectrum shows a sharp Compton

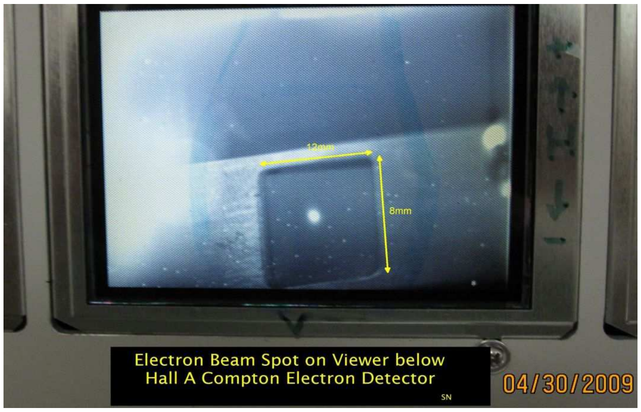

Figure 3: Electron beam spot on the installed Chromax beam viewer confirming the proper installation and alignment of the new electron detector.

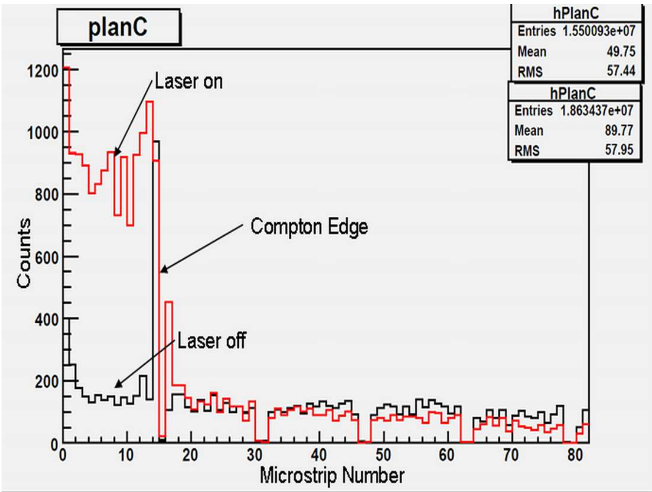

Figure 4: First Compton scattering electron spectrum obtained from the newly installed silicon microstrip detector with 3 GeV electron beam and 1064 nm laser beam.

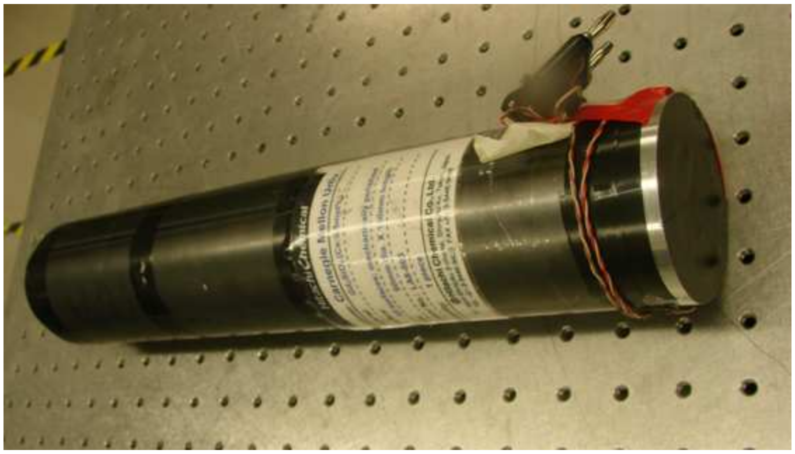

Figure 5: GSO Calorimeter assembled and tested at Carnegie-Mellon University

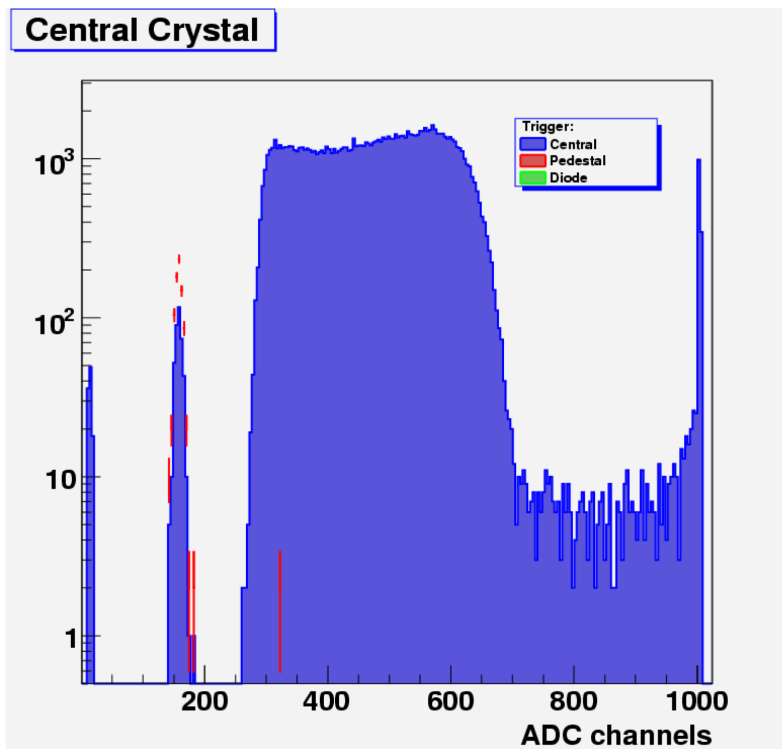

Figure 6: Compton scattering spectrum of 5.9 GeV electrons from 1064 nm laser beam obtained with the new GSO Calorimeter, demonstrating better than 100 signal-to-background ratio.

edge indicative of the high energy resolution of the new detector. In addition, excellent signal to background of over 100 was recorded with the new calorimeter. The GSO calorimeter proved to live up to our design goals of providing superior counting and integrating abilities over a broad range of energies. Data analysis is being carried out by Diana Parno and Megan Friend from CMU.

In Spring of 2009, the old $PbWO_4$ calorimeter was decommissioned and a new support structure and motion control scheme for the GSO calorimeter was implemented. Driven by the needs of the upcoming PREX experiment a redesign of the photon beam line was carried out by Brian Quinn, CMU. The beam pipe was broadened to 1.5" from the existing 1" diameter to increase the acceptance for 1 GeV Compton scattering. In addition, a new adjustable lead collimator was designed for the GSO calorimeter. With the new hardware changes, satisfactory performance for the GSO calorimeter was obtained during the running of the Compton polarimeter during HAPPEX-III and PVDIS experiments during the latter part of 2009.

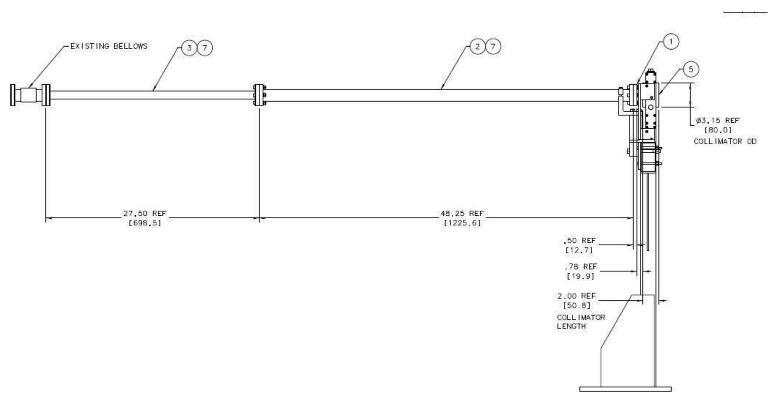

Figure 7: Photon beamline upgrade for larger acceptance carried out by Carnegie-Mellon University. The beam pipe was expanded to 1.5" diameter in order to accommodate lower energy Compton scattering for the PREx experiment.

2.1.5 Fabry-Perot Cavity

Recent advances in the manufacturing of high reflectivity and low-loss dielectric mirrors as well as availability of narrow line-width green lasers facilitates the feasibility of our challenging design goal. High-gain cavities at 532 nm have been successfully constructed by the PVLAS[3] group that has a geometry and gain comparable to our proposed design. A schematic lay-out of the optical set-up for the upgrade is shown in Fig. 8. The heart of the upgrade plan is to replace the infrared cavity with a 532 nm green cavity fed by the new laser. Our solution for the laser is a fiber-coupled Nd:YAG laser (Innolight Mephisto S [4]) seeding a 10 W Ytterbium doped fiber amplifier (IPG Photonics[5]) which pumps a 50 mm Periodically Poled Lithium Niobate (PPLN) supplied by HC Photonics [6] which produces up to 2 W of 532 nm beam with less than 10 kHz linewidth. The green beam is amplified in a 850 mm long Fabry-Perot cavity with adjustable mirrors.

A new cavity structure (Fig. 9) with adjustable mirrors and ultra-high vacuum capabilities has been fabricated and tested in our Lab to facilitate the development of high-gain cavity studies. Significant progress has been made in the development of the green Fabry-Perot cavity with the conversion of the ARC Compton Lab into a class 1000 cleanroom and acquisition of high-finesse mirrors from General Optics (GSI) and Advanced Thin Films (ATF).

Development of the home-grown fiber amplifier pumped PPLN laser continued in 2009. Mohamed Hafez, Old Dominion University, joined our team as a post-doc to carry on the efforts on the PPLN laser. Long-term stability tests of the PPLN beam up to 1 W green power with 4 W of IR pump power were carried out for 24 hour periods. Green power stability was recorded at a satisfactory 3% rms deviation over the period. A new enclosure for the PPLN setup was fabricated and implemented in the Summer of 2009. Full temperature and power scan calibration of the PPLN laser was completed during the same time.

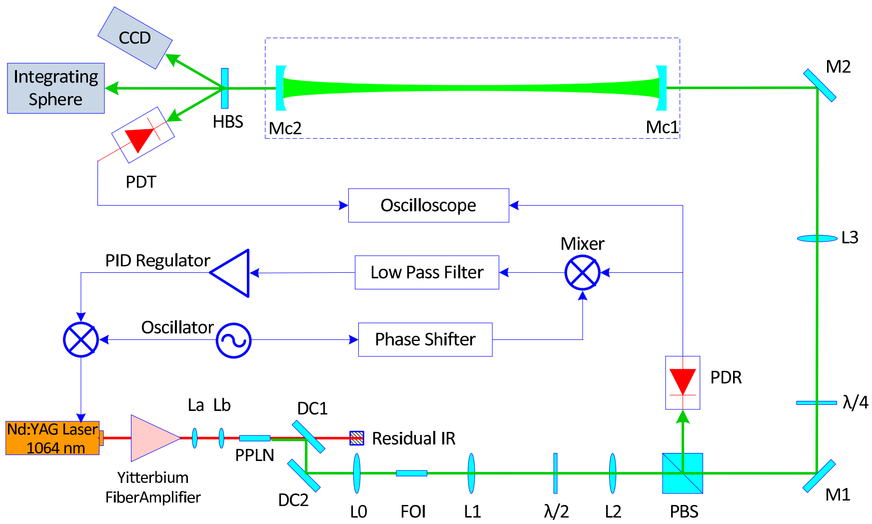

Figure 8: Optical set-up of the green Compton polarimeter.

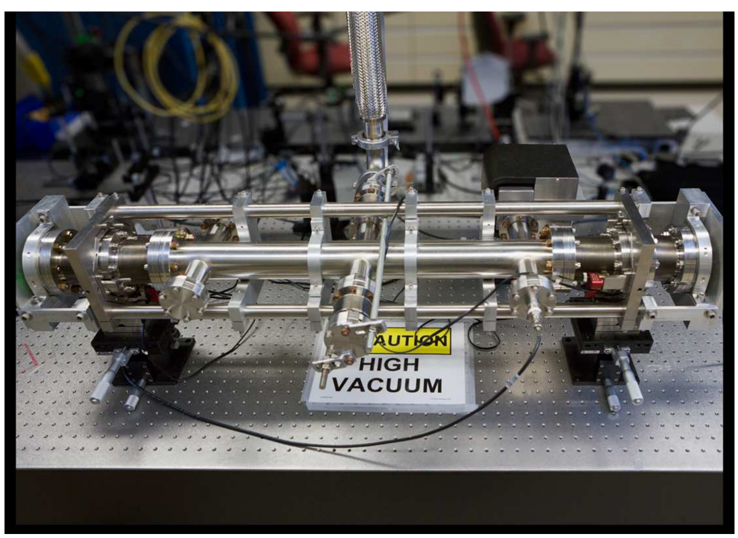

Figure 9: The green Compton Polarimeter Fabry-Pero cavity under test in the Compton Lab.

The 240 ppm mirrors that we successfully acquired lock with the amplified PPLN beam in late 2008, were further tested this year for high gain and high power studies. Successful long-term (over 24 hours) lock was acquired with GSI 240 ppm mirrors at low cavity power. However, the mirrors failed to sustain higher than 700 W of cavity power due to mirror heating from excessive loss. The next set of GSI mirrors with 100 ppm transmission were also plagued with high loss. Although we acquired lock successfully with these mirrors, we were not able to obtain higher that 500 W power with the GSI-100 mirrors. The GSI mirrors had losses far in excess of our 10 ppm loss specification to meet our high power needs.

The new ATF mirrors with 100 ppm transmission and less than 10 ppm total loss as per our specification were delivered to our Lab in September 2009. Modifications to the cavity mirror mount were completed by October to house the new smaller mirrors. Modifications were made to the Cavlock servo electronics to reduce noise and improve bandwidth of the feedback loop in order to respond to the high gain of the ATF mirrors. We acquired successful lock with the mirrors at with 100 mW laser power in November 2009. Illustrated in Fig. 10 is the oscilloscope trace of short-term lock acquisition. Ch. 1 (yellow) shows the green power transmitted through the cavity; Ch. 2 (blue) is the power reflected by the cavity; Ch. 3 (magenta) is the slow feedback signal and Ch. 4 (green) is the fast feedback signal send to the laser to sustain lock. As seen from the flatness of the transmission photodiode and the complementary reflection photodiode signals cavity lock was steady on the peak of the fundamental mode.

Decay time of the cavity was measured by monitoring the power of the beam transmitted from the cavity with a fast photodiode after turning off the laser. The transmitted power as a function of time as recorded by a digital storage oscilloscope is shown in Fig. 11. The measured decay time of 28.4 μs corresponds to a cavity finesse of 26,805. We further measure a transmittance and loss of 87 and 14 ppm as opposed to our specification of 100 and 10 ppm, respectively.The specifications and the measured parameters for the ATF mirrors are summarized in Table.2. The cavity power gain achieved was about 7500.

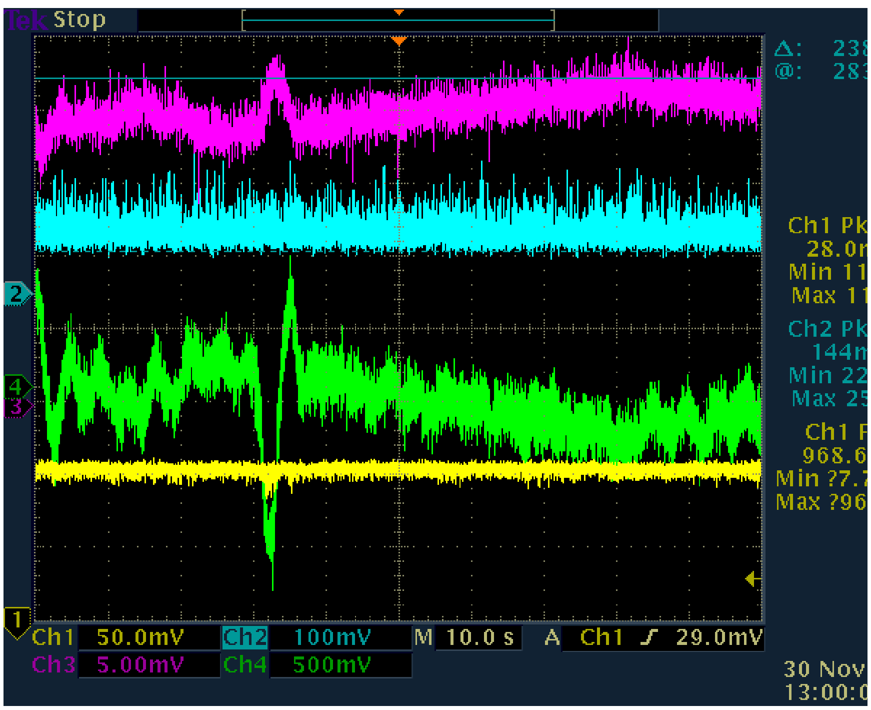

Figure 10: Short-term lock acquisition with the ATF 80 ppm mirrors. Ch. 1 (yellow) shows the green power transmitted through the cavity; Ch. 2 (blue) is the power reflected by the cavity; Ch. 3 (magenta) is the slow feedback signal and Ch. 4 (green) is the fast feedback signal send to the laser to sustain lock.

High-power tests of the cavity were conducted in early December 2009. We ramped the input power from about 0.1 to 1 W and measured near linear scaling of the cavity power. The highest power recorded was

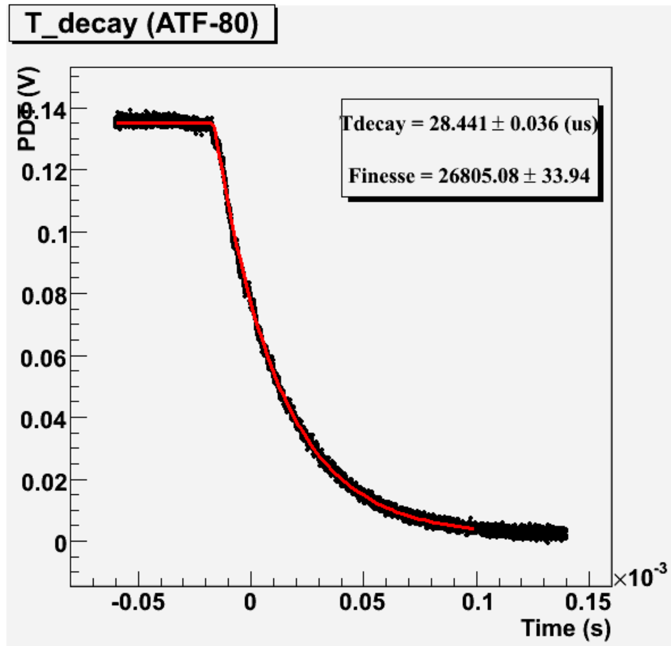

Figure 11: Characteristic decay time of the cavity power measured with a photodiode monitoring the power transmitted from the cavity. The measured decay time of 28.4 μs corresponds to a cavity finesse of 26,805.

	Specification	Measured
Diameter [m]	7.75	
Thickness [mm]	4	
ROC [mm]	500	
Coating	HR@532 nm	
Transmittance [ppm]	100	87
Loss [ppm]	10	14
Finesse	28560	26800
Gain	8000	7500

Table 2: Performance of the ATF low loss mirrors

5.6 kW with 0.93 W laser power. This easily exceeds our design goal of 1.5 kW and is the highest published power in a 532 nm Fabry-Perot cavity to the best of our knowledge.

Long-term stability tests of the cavity were conducted at 400 W. With a few minor drop-outs, as illustrated in Fig. 11, the cavity power held steady with about 2.5% σ fluctuation. High-power stability tests are planned in the future.

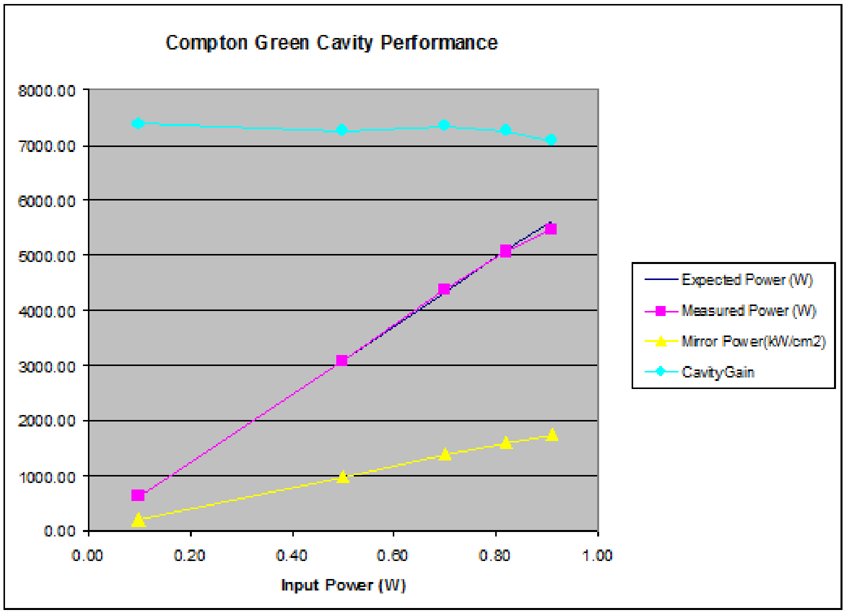

Figure 12: Power scan result for the green Fabry-Perot cavity demonstrating linear intra-cavity power scaling with input laser power. The solid black curve is the expected cavity power based on linear scaling with input laser power; the squares (magenta) are the measured cavity power; the closed circles (cyan) are for the corresponding cavity gain; and the solid triangles (yellow) are for the corresponding power density on the cavity mirrors.

2.1.6 Conclusion

The electron and photon detector upgrades for the Compton polarimeter have been successfully installed. Commissioning of the detectors is nearly complete. The electron detector falls short of expectations plagued with low detection efficiency. Solutions are being probed. On the other hand, the GSO photon detector performance exceeds expectations.

On the cavity front, we have demonstrated that with our home-made PPLN laser, newly acquired ATF mirrors, adjustable mirror invar cavity, and home-made cavlock servo electronics up to 5 kW of intra-cavity green power is possible. This is to the best of our knowledge the highest power recorded in a 532 nm Fabry-Perot cavity. Much work remains to be done to deliver this high power in a stable and reliable manner for Compton polarimetry in Hall A.

References

[1] S. Nanda and D. Lhuillier, Conceptual Design Report for Hall A Compton Polarimeter Upgrade, Unpublished.

[2] Jlab Experiment E06002, Paul Souder, Robert Michaels, Guido Urciuoli spokespersons.

[3] M. Bregant *et al.*, arXiv:hep-ex/0202046 v1 28 Feb 2002.

[4] Innolight GmbH, http://www.innolight.de/

[5] IPG Photonics, http://www.ipgphotonics.com/

[6] HC Photonics, http://www.hcphotonics.com/

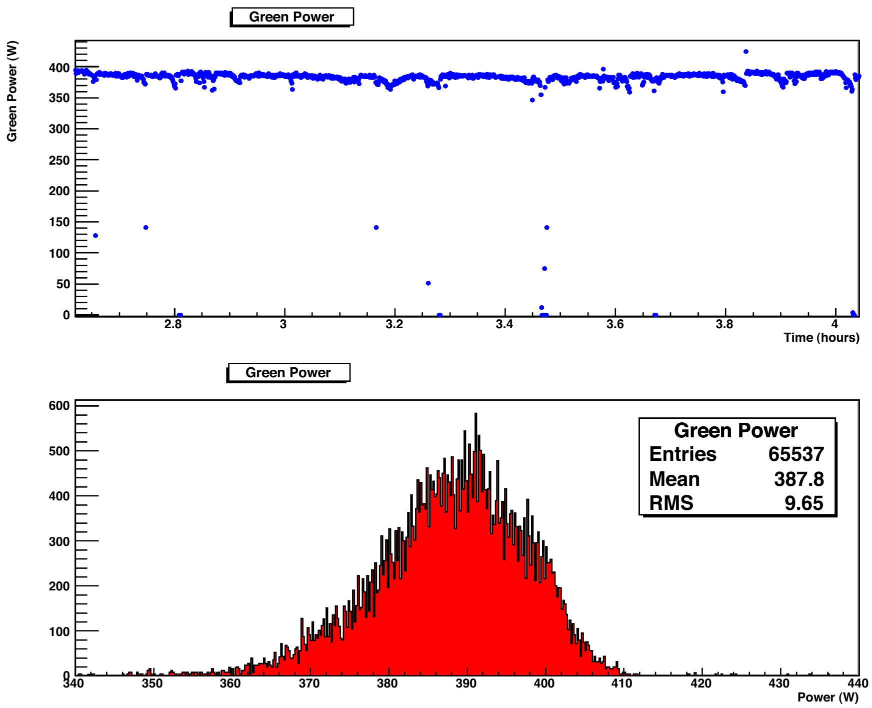

Figure 13: Long-term stability of green cavity lock. The top curve shows cavity power as a function of time over more than one hour period while the bottom curve is a histogram of the cavity power over the same interval. About 2.5% σ fluctuation in power is observed.

2.2 Compton Electron Detector

(Contributed by A. Camsonne)
S. Nanda, C. Hyde, M. Brossard, R. Michaels, D. Wang, R.S. Holmes

A new silicon microstrip detector for electrons ("Edet") was deployed for the Compton polarimeter in 2009. The detector worked partly and provided useful calibration of the photon detector response function during HAPPEX-III; however, there were many problems.

The Edet consists of 4 planes of silicon microstrips, 240μm pitch, 192 strips per plane. Signals from the strips are amplified, passed through discriminators, and digitally processed in a custom VME board (the "ETROC"). The detector is placed a few millimeters from the beam and detects the electrons from Compton scattering. It may provide a calibration for the photon detector, as well as an independent measurement of the asymmetry. We saw asymmetries but the precision was not sufficient to make an impact on the overall error budget.

The first major problem encountered is low-energy background making the detector draw a large amount of current. We had to increase the amount of shielding up to 500 μm of copper to be able to operate the detector in the 1 to 4 GeV range. This amount of shielding seemed to be not sufficient to run at 100 uA at 6 GeV.

When the detector has sufficient shielding and beam quality is good, the electron detector was able to operate but it turned out that its efficiency was low, around 10% per strip (Fig. 14). Pulser tests of the ETROC were performed to verify the FPGA logic and the integrity of the read-out and decoding. The Edet efficiency is difficult to measure. The best way we found was to use tracks and demand there are hits on 2 of the 3 planes (the first plane "A" was usually not working). With a track candidate established by 2 planes, one queries whether the third had a hit or not.

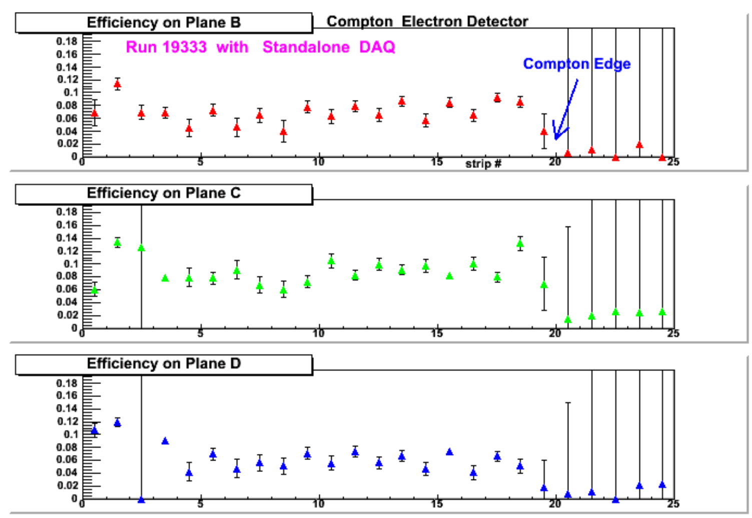

Figure 14: Strip efficiency as a function of strip number for run 19333.

During the down-time tests were carried out using Strontium and Ruthenium sources. The source studies gave efficiencies that were consistent with the low efficiency measured with beam. In order to investigate this problem, analog amplifier boards were built, allowing to see the signal of the detector before discrimination. However, it is hard to conclude on the amplitude of the minimum-ionizing electrons because of the beta energy distribution.

With a coincidence with a scintillator triggering the oscilloscope we estimated the signal to be about 12 mV using the Ruthenium source (Fig. 15).

Probably the best of these attempts was with an Americium α source, where we had to measure and correct for the energy loss.

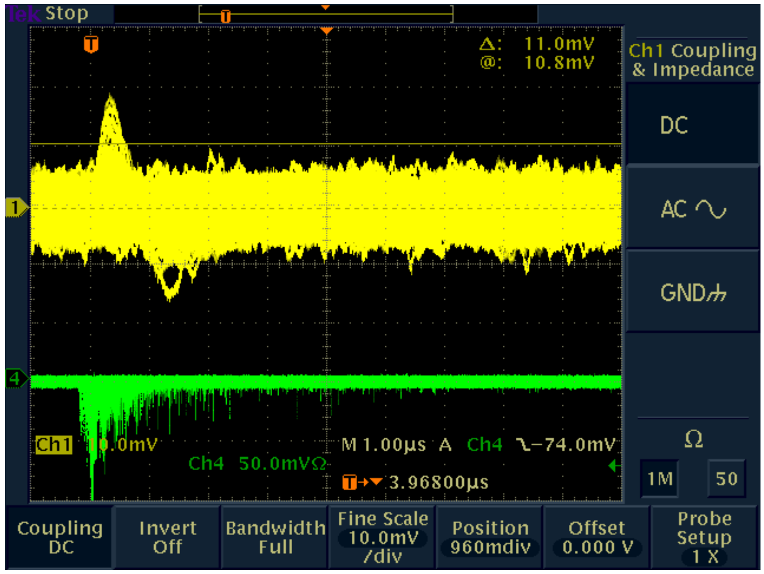

Figure 15: Analog signal of ^{106}Ru source triggered by a scintillator behind the detector to detect electrons going through the plane.

Some analog traces were also recorded on the electron detector with actual beam, this time triggered by Compton photons, which seemed to confirm the source results.

The amplitude of a minimum-ionizing Compton electron was around 12 mV (Fig. 17) with an efficiency at the level of 10%.

The reason for the inefficiency was subsequently understood and could be estimated as being due to the high capacitance of the electronic circuit associated with the amplitude of the signal giving a poor signal over background ratio.

A future upgrade may be to put the amplifiers much closer to the strips to avoid the noise induced by the extra capacitance from the cables or the electronic backplane reducing the sensitivity to electronic noise.

The main focus for HAPPEX-III experiment was to cross-calibrate the photon detector with the electron detector to obtain a response function and extract the polarization from the photon analysis. This goal was partly met, but not without difficulties. Since the simultaneous data taking of electron data and photon data was showing a not-understood widening in the charge asymmetries, most of the data were taken as photon-only in order to act as monitoring of the polarization for cross check. Some dedicated runs were taken with the electron detector. It turned out that the coincidence trigger operated only at lower current, its efficiency of flagging coincidence events decreasing rapidly as rates were increased. This still has to be fully understood but two suspects are dead time and the problem of synchronizing the clocks between the photon and electron events. The work-around was to take dedicated runs at lower current. The coincidence between Compton photons and electrons could be clearly seen on the correlation plots (Fig. 18) of photon amplitude as a function of electron strip number.

A few single-arm runs where taken for testing. They allowed to see Compton asymmetries (Figs. 20 and 22) but the systematical error due to the low efficiency and the polarized background from the shielding are yet to be determined.

On the hit pattern one can clearly see the Compton events and a rapid rise of the counts at low strip numbers, meaning getting closer to the beam (Figs. 19 and 21). This rise would be attributed to beam halo making it directly to the detector. On the coincidence run one can see a bump in the Compton photon ADC at what seems lower energy than the electron detector silicon acceptance. Since low energy in photons means higher energy electrons and a lower strip number, it would correspond to energies outside the sensitive silicon area where the shielding at the bottom of the detector is located. Those higher energy electrons re-scatter in the detector thus generating a trigger where no sensitive area is present.

We found a discrepancy of the position of the zero-crossing in the asymmetry which we attribute to the

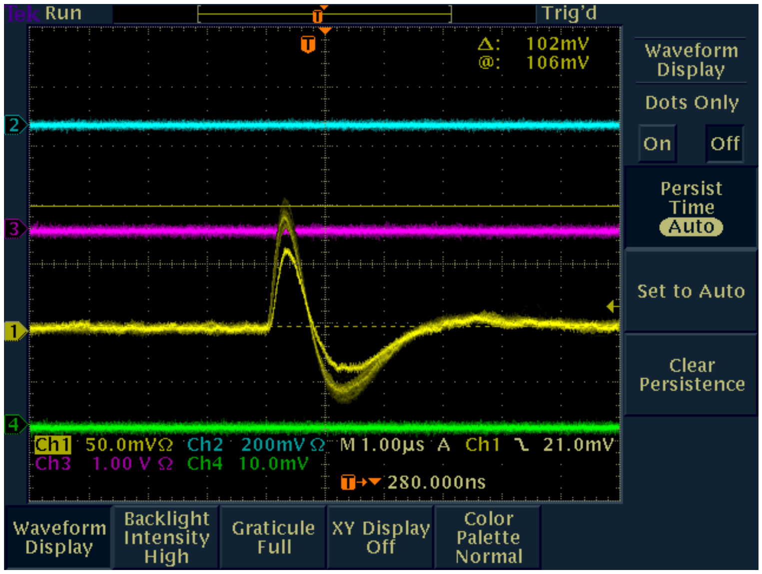

Figure 16: Analog signal of ^{241}Am source.

afore-mentioned effect of the shielding giving a polarized background, this effect would have to be unfolded in a simulation to extract the polarization of the single-electron data. This effect seems to be able to be reduced requiring multiple coincidences (Fig. 23) through several planes but statistics becomes rapidly scarce because of the intrinsic low efficiency of each planes. The extracted number (Fig. 24) is consistent with the Møller measurement of around 87% but is very inaccurate.

Using the response functions determined from the coincidence data, Richard Holmes extracted the polarization from the photon single arm data. In Fig. 25, we have the extracted polarization as a function of run number. The dispersion is quite large, hinting at some still unknown systematical errors. Analysis is still ongoing to improve the result and will be used to cross check the data obtained by the photon FADC DAQ.

The DAQ has also been a problem. It is based on obsolete components and has some irreplaceable custom parts with no spares in some cases. We have a plan to deploy a simplified version of the DAQ system using a Trigger Supervisor (TS) to coordinate the Edet readout and the CMU-FADC readout, which are in separate crates. The TS will also allow us to run at a 240 Hz helicity-flip rate, something we can not do with the old DAQ. The TS-based DAQ will be deployed alongside the old DAQ in such a way that they don't interfere, though they cannot run simultaneously. The intention is to keep the old DAQ functional during PREX and to make a smooth transition to the new DAQ.

We can conclude that the detector worked at some level for HAPPEX-III but it is not clear how good that data will help the standard photon analysis. The major work that still needs to be done :

- on the detector side to improve the signal over background
- on the electronics to reduce the electronic noise, cross-talk and pick-up
- on the data acquisition to improve the overall stability, study dead-time systematics and develop a reliable way of taking coincidence data continuously.

The current situation is that the low efficiency compels us to run with very low thresholds making us sensitive to all sources of noise, electronics or physical. So a thorough study of the detector response and sources of background and optimization of the shielding are needed. This will probably lead to a major redesign to have a reasonably working detector.

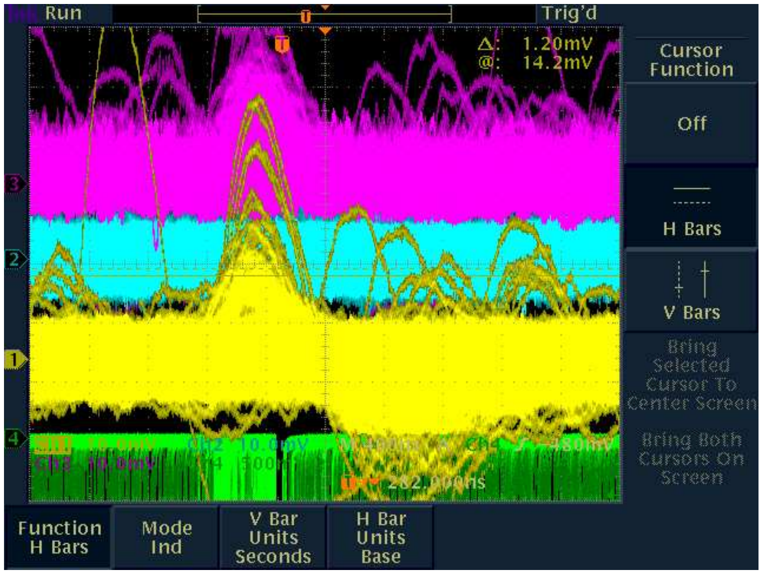

Figure 17: Analog signal of the electron detector triggered by the Compton photon with a long persistence.

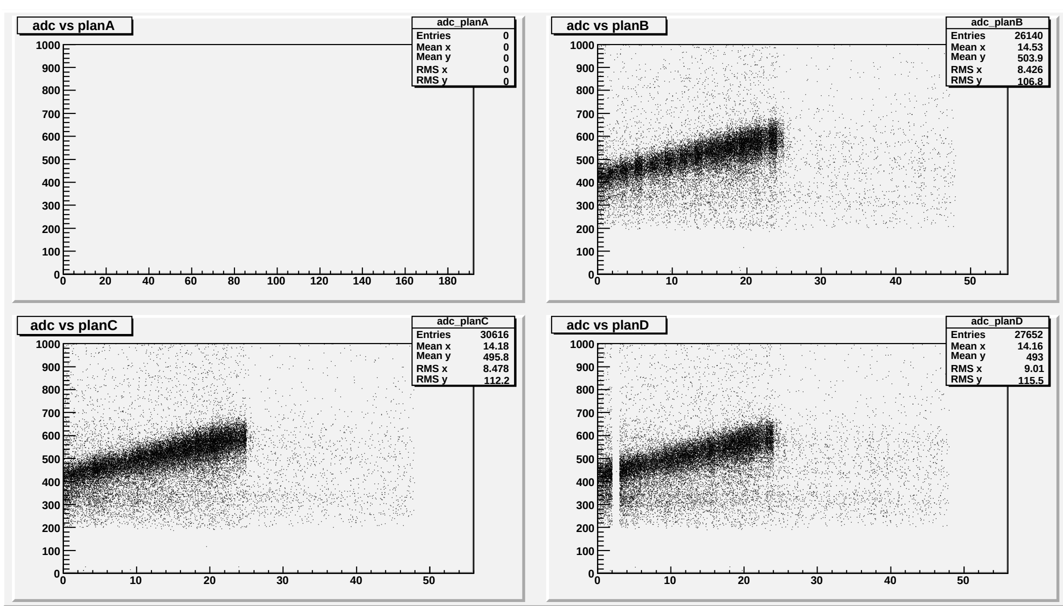

Figure 18: Plot of photon amplitude as a function of strip number: the correlation of the Compton events is seen.

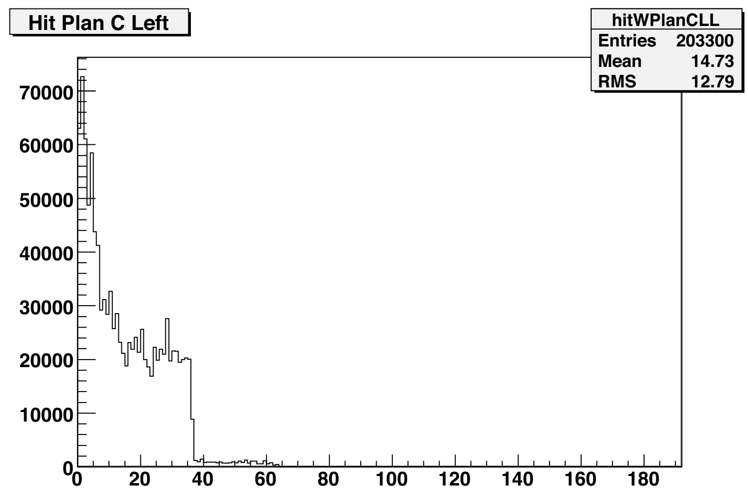

Figure 19: Hits in plane C of the electron detector as a function of strip number for run 20388

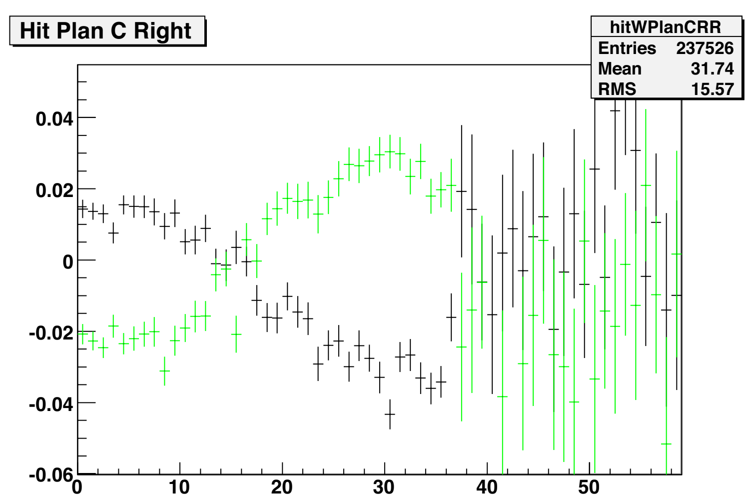

Figure 20: Asymmetry in plane C of the electron detector as a function of strip number for run 20388.

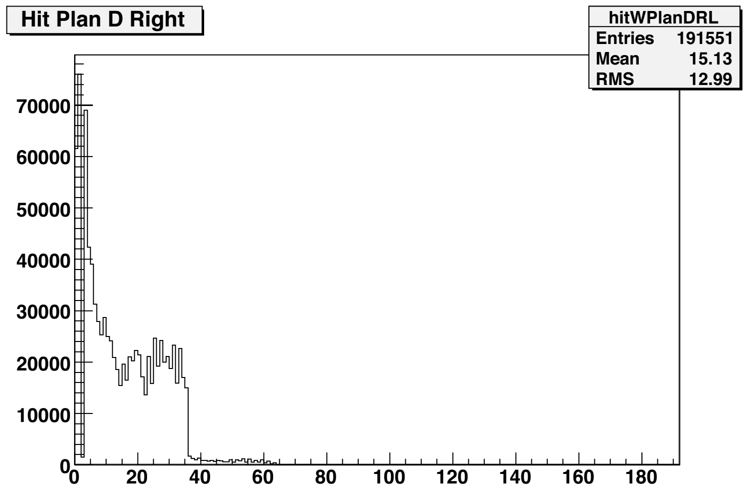

Figure 21: Hits in plane D of the electron detector as a function of strip number for run 20388.

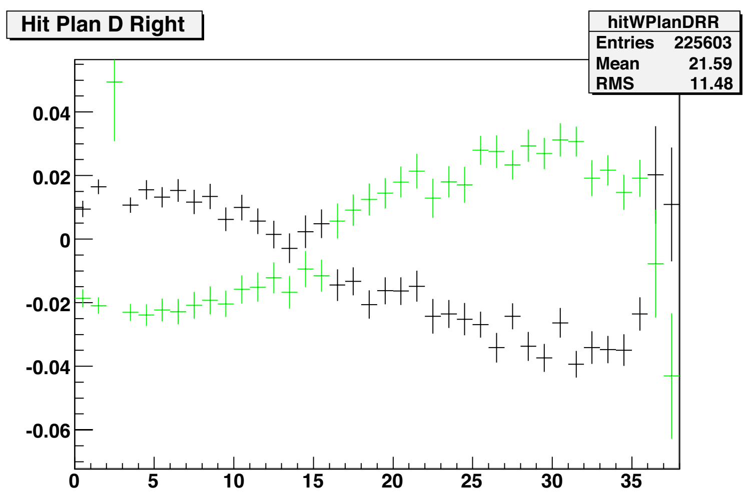

Figure 22: Asymmetry in plane D of the electron detector as a function of strip number for run 20388,

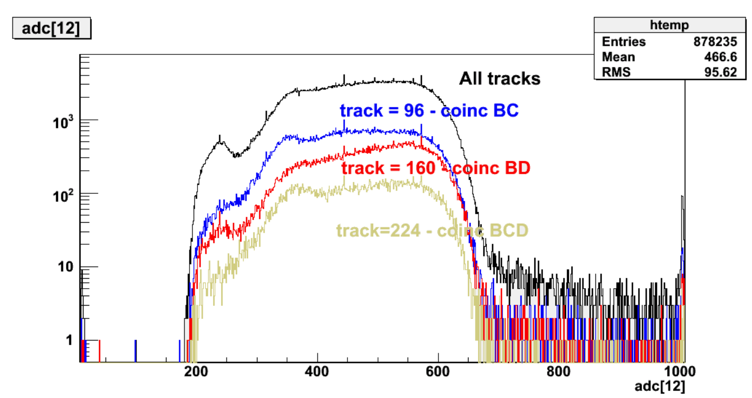

Figure 23: Coincidence photon ADC spectrum requiring conditions on the number of planes hit.

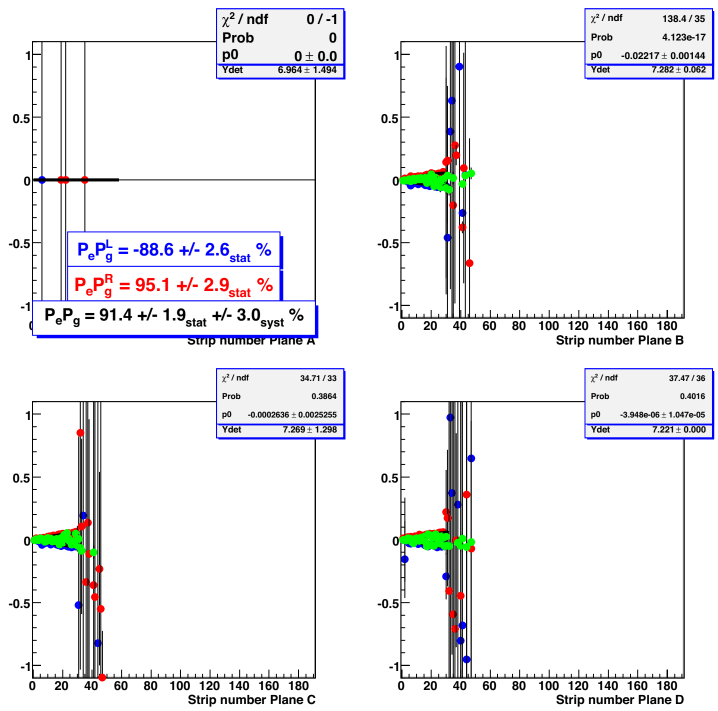

Figure 24: Extracted polarization from the raw electron asymmetry.

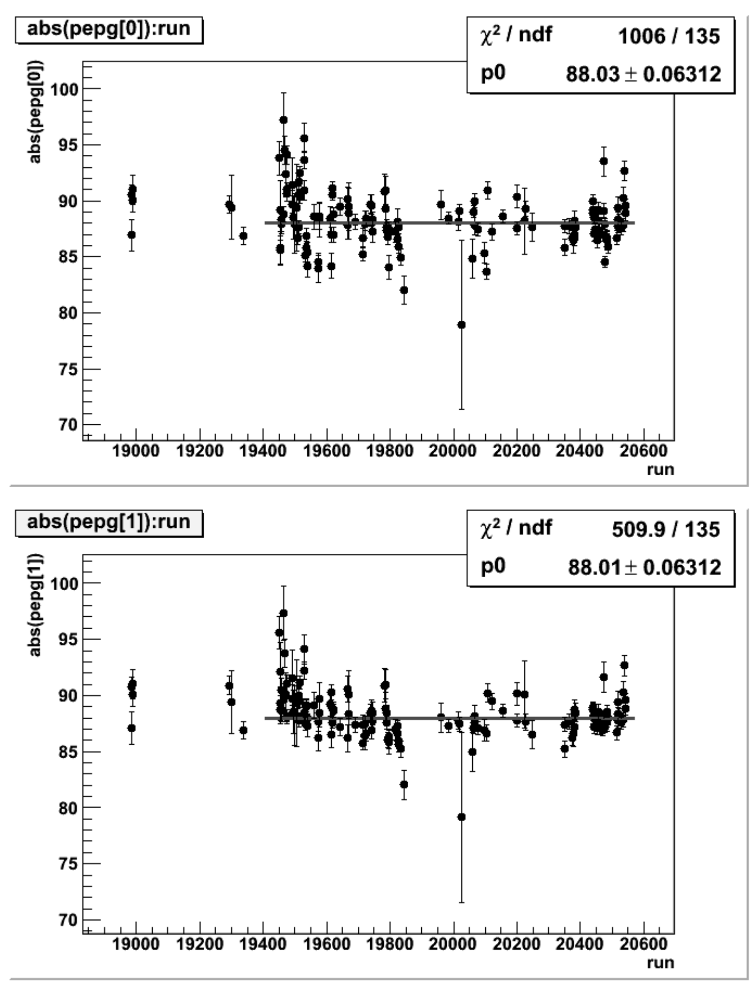

Figure 25: Extracted polarization from the photon asymmetry using the response functions determined with the coincidence data as a function of run number.

2.3 Møller FADC DAQ Upgrade

B. Sawatzky, Z. Ahmed, C-M Jen, E. Chudakov, R. Michaels
D. Abbott, H. Dong, E. Jastrzembski

A Møller DAQ upgrade based on the JLab-built FADC has been in progress in 2009 and is nearly complete. It is part of the upgrade of the Møller polarimeter aimed at achieving a systematic error less than 1%.

2.3.1 Application to Møller Polarimetry

The Hall A Møller polarimeter detects the two scattered electrons in two spectrometer arms. Each arm consists of 4 calorimeter blocks arranged in a column and a scintillator aperture counter positioned on the upstream side. When the upgrade is complete there will be 4 aperture counters per arm. The electrons are swept along the column by a dipole magnet so their positions depend on their energy. The HV on the PMTs are tuned to equalize the calorimeter outputs from all 4 blocks, allowing a common threshold to provide an efficient trigger. We hope to run at 50 μA peak current and 5% duty cycle; this will reduce the uncertainty due to extrapolation from higher currents where the experiments run and the 2 μA where Møller normally runs to keep target heating low. A higher speed DAQ is needed to accommodate maximum expected rates above the thresholds of 1 MHz per arm with a coincidence of 400 kHz. Since the FADC processes all the data and no samples are lost, it has the prospect of greatly reducing or even eliminating the deadtime, which historically was an important systematic error for Møller and which would potentially limit the high-peak-current application.

To first order the deadtime probability "ϵ" of one discriminator channel is $\epsilon = RT$ for a rate R and a discriminator width T (typically $T = 20$ ns for the old DAQ). For the full DAQ the deadtime is a much more complex expression because several discriminator channels are involved and the rate is a mixture of singles-arm and coincidence Møller with different asymmetries and rates, as well as unpolarized background mainly from radiative Mott. Historically the systematic error due to ϵ was no better than $d\epsilon = 0.3\%$ at the low currents where the old DAQ ran. Note, the deadtime correction to the observed asymmetry $A_{\rm obs}$, arriving at the physics asymmetry $A_{\rm phy}$ is:

$$A_{\rm phy} \;=\; A_{\rm obs}\,[1-\epsilon] \tag{1}$$

For the new DAQ we may hope that ϵ is very small or zero and that $d\epsilon \ll 1\%$. This will be demonstrated by showing how the observed rate and asymmetry varies with beam current.

With the old setup, the calorimeter signals arrive at an analog fan-out unit, the analog sums from the columns as well as the signals from the scintillation counters pass through discriminators, and various coincidence signals are formed with a Programmable Logic Unit (PLU). The coincidence rates are recorded with scalers and read out every helicity cycle at 30 Hz. Additionally, the raw signals are measured with ADC and TDC units, triggered by a selected combination of the pulses from the PLU. The first 3–10 of such events per helicity cycle were recorded, in order to make sure that the data are good, but without overloading the DAQ system. The Møller asymmetry can be measured only with the scalers, since the statistics of the ADC/TDC events is 100–1000 times shorter than needed for that. The "helicity triggers" contain additional information: scalers for a beam current monitor (BCM, VtoF), a 100 kHz pulser in order to measure the helicity window, encoders for the target positions etc. All the triggers contain the trigger info, the helicity state and the beginning of a helicity quad pattern (QRT), recorded via input registers.

One 16-channel FADC unit should be able to replace nearly all the electronics from the old setup. In addition, it would allow a reduction of the systematic errors by:

- measuring the asymmetries using all the event data;
- analyze the pile-up effects and compensate for them.
- reducing the deadtime correction and associated systematic error

The FADC implementation does the following

- Make logical signals when combination of the input signals exceed certain thresholds;

- Write out the FADC "event" data using a logical signal for the trigger with an adjustable prescaler, at a rate up to the maximum rate allowed by the existing FADC systems (160 kHz); the rate capability of the new FADC is expected to exceed 300 kHz.
- Makes internal scalers in the FADC unit counting the coincidence signal; the scalers are read out at every helicity cycle;
- The readout includes the "event triggers" (< 160 kHz) and the "helicity triggers" (30–2000 Hz). Both additionally contain the helicity bit and the QRT bit;
- The "helicity trigger" readout includes additional scalers/ADC for the BCM, pulser, BPM, encoders etc.

2.3.2 Signal Processing Logic and DAQ Architecture

The input signals are typically -2 Volts and 40 nsec wide with a fall time of 5 nsec. Let P_i^j be the calorimeter PMT data for samples j and ADC input channel i, and let S_i^j be the scintillator data. The data are summed over 2 samples $j = 1, 2$ because the signals are aligned in time sufficiently well that they should peak within adjacent 4 nsec windows. We have set two programmable parameters: threshold$_1$ and threshold$_2$ in order to build logical combinations:

- **CL** $= \sum_{i=1,4} \sum_{j=1,2} P_i^j \ \geq \text{threshold}_1$
- **CR** $= \sum_{i=5,8} \sum_{j=1,2} P_i^j \ \geq \text{threshold}_1$
- **SL** $= \left(\sum_{j=1,2} S_1 \geq \text{threshold}_2\right)$ .OR. $\left(\sum_{j=1,2} S_2 \geq \text{threshold}_2\right)$ .OR. $\left(\sum_{j=1,2} S_3 \geq \text{threshold}_2\right)$ .OR. $\left(\sum_{j=1,2} S_4 \geq \text{threshold}_2\right)$
- **SR** $= \left(\sum_{j=1,2} S_5 \geq \text{threshold}_2\right)$ .OR. $\left(\sum_{j=1,2} S_6 \geq \text{threshold}_2\right)$ .OR. $\left(\sum_{j=1,2} S_7 \geq \text{threshold}_2\right)$ .OR. $\left(\sum_{j=1,2} S_8 \geq \text{threshold}_2\right)$

The triggers, which initiate a readout of the FADC raw data, are a mixture of the coincidence (CL.and.CR) and singles (CL, CR) with prescale factors from 1 to 2000. The FPGA produces a kind of a scaler, counting

- CL
- CR
- CL.AND.CR
- CL.AND.SL
- CR.AND.SR
- CL.AND.CR.AND.SL.AND.SR
- CL.AND.CR.AND.(SL.AND.SR delayed>100ns)

These scalers are read out by a separate trigger at the helicity cycle at 30Hz to 2kHz. In essence, the scalers are a deadtime-free integration of the data, integrated over the helicity period. A standard externally supplied helicity gate defines the integration time.

The DAQ is a standard CODA-based system using high-performance components for handling the high rates: a 64x VME crate, a 6100 VME cpu, Gigabit ethernet, and fast PC and disks.

2.3.3 Status and Results

The new Møller DAQ was first put in the Hall in July 2009 and has been tested parasitically during the HAPPEX-3 and PVDIS experiments whenever a standard Møller polarimetry measurement was performed. The signals from the calorimeters are fanned out, with a copy going to the new DAQ while the old DAQ was preserved. The scintillators in the aperture were not yet available to the new DAQ. The rate capability was 20 MByte/sec to disk and can possibly be doubled in the future.

During the initial running, several small problems were noted which led to further testing of a copy of the FADC in the DAQ test lab and subsequent upgrades and bug-fixes for the FPGA firmware. At the moment, there are still a few mysteries which appear under certain running conditions and the FADC is under active development and testing. Nevertheless, for normal running conditions we have seen promising results. Figure 26 shows some typical snapshots of the FADC for calorimeter signals: voltage versus time. We integrate these pulses to obtain an energy deposition. Figure 27 shows the sum of the integrals of four calorimeter blocks in one spectrometer arm. Essentially this is the total energy deposited in the spectrometer. The data are reasonable and agree with the old DAQ. The rates are about 50% higher than for the old DAQ, but this is probably because the new DAQ does not yet use the aperture scintillator counters. This will be remedied during the January shutdown when we install new segmented scintillator counters. Fig 28 shows a 5% asymmetry from Møller scattering. This is slightly different (2% relative) to the old DAQ, again probably because of the aperture counters. We have taken some data with different beam currents and target thicknesses to begin studying the deadtime; preliminary results are encouraging.

As of this writing, there is much more work needed before the new DAQ is fully reliable and its advantages are demonstrated. During the January shutdown, pulser tests will be performed. The deadtime needs to be measured with higher precision. The new segmented scintillators from Syracuse University will be deployed. In addition, the GEANT Monte Carlo will be revived and used to study systematic effects such as acceptance and magnet misalignments. It might also be possible to simulate the deadtime of the system.

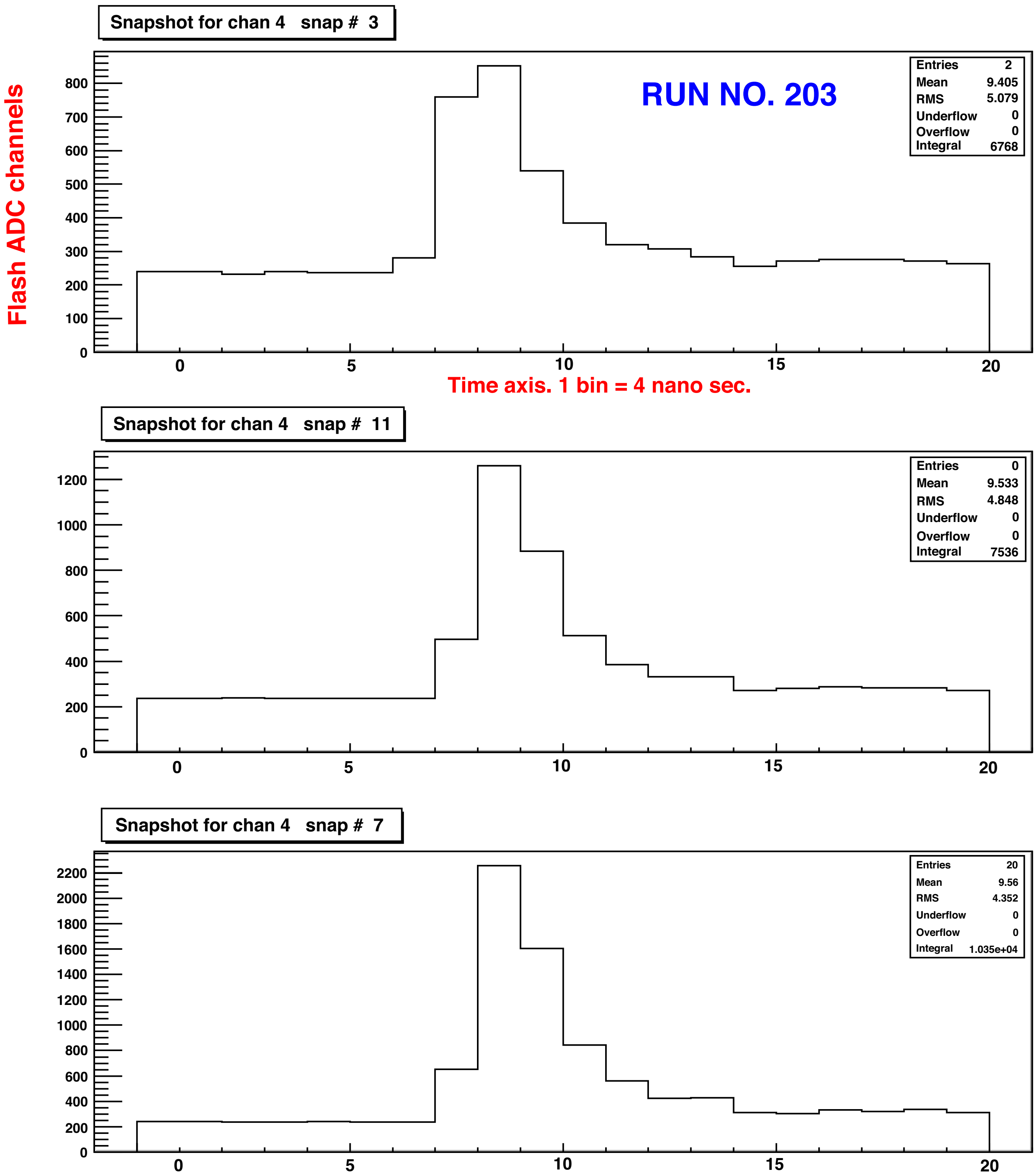

Figure 26: Typical pulses from the Møller calorimeter. Each snapshot shows the voltage versus time in the FADC.

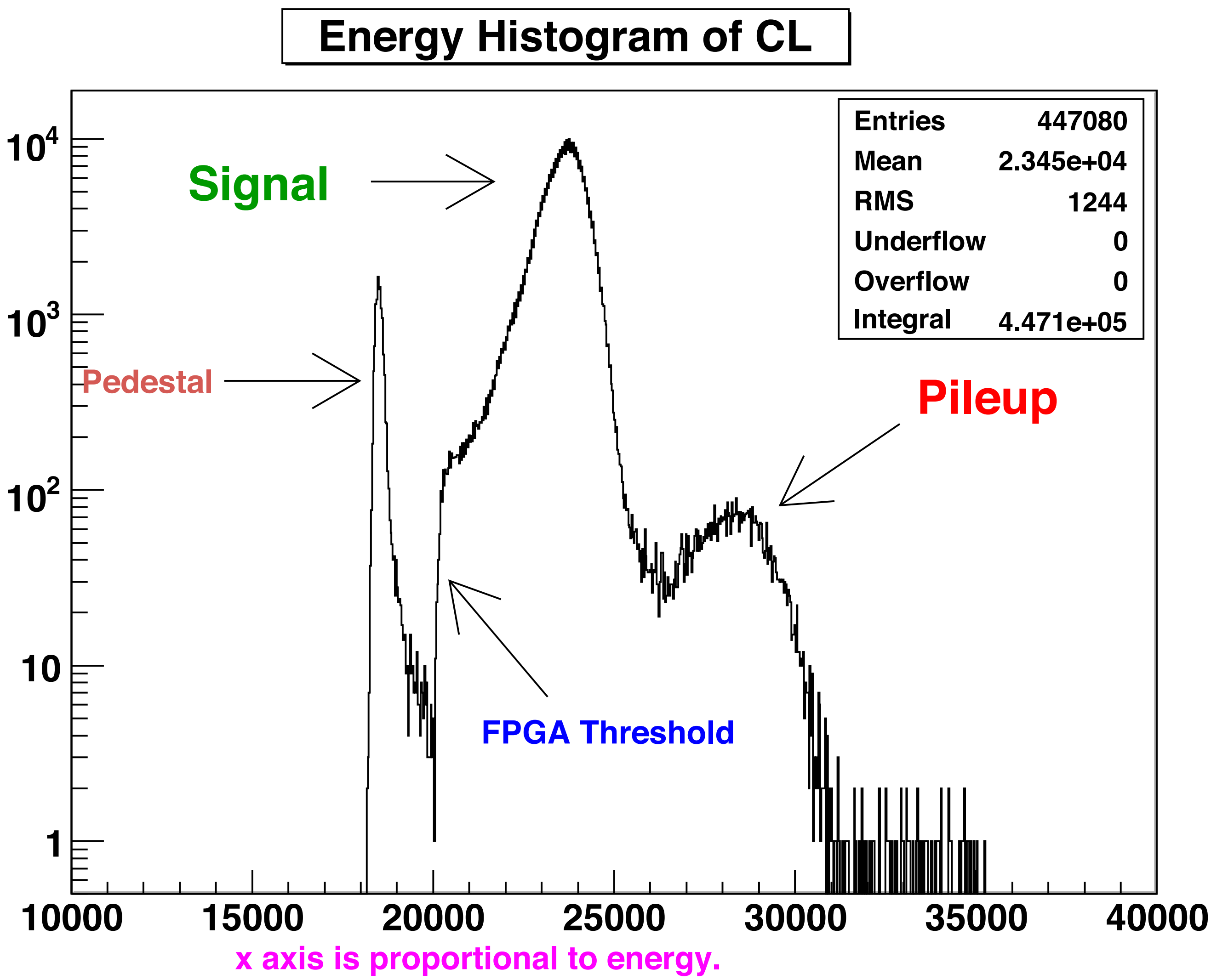

Figure 27: Integrated energy in one spectrometer from Møller calorimeters as processed by the FADC.

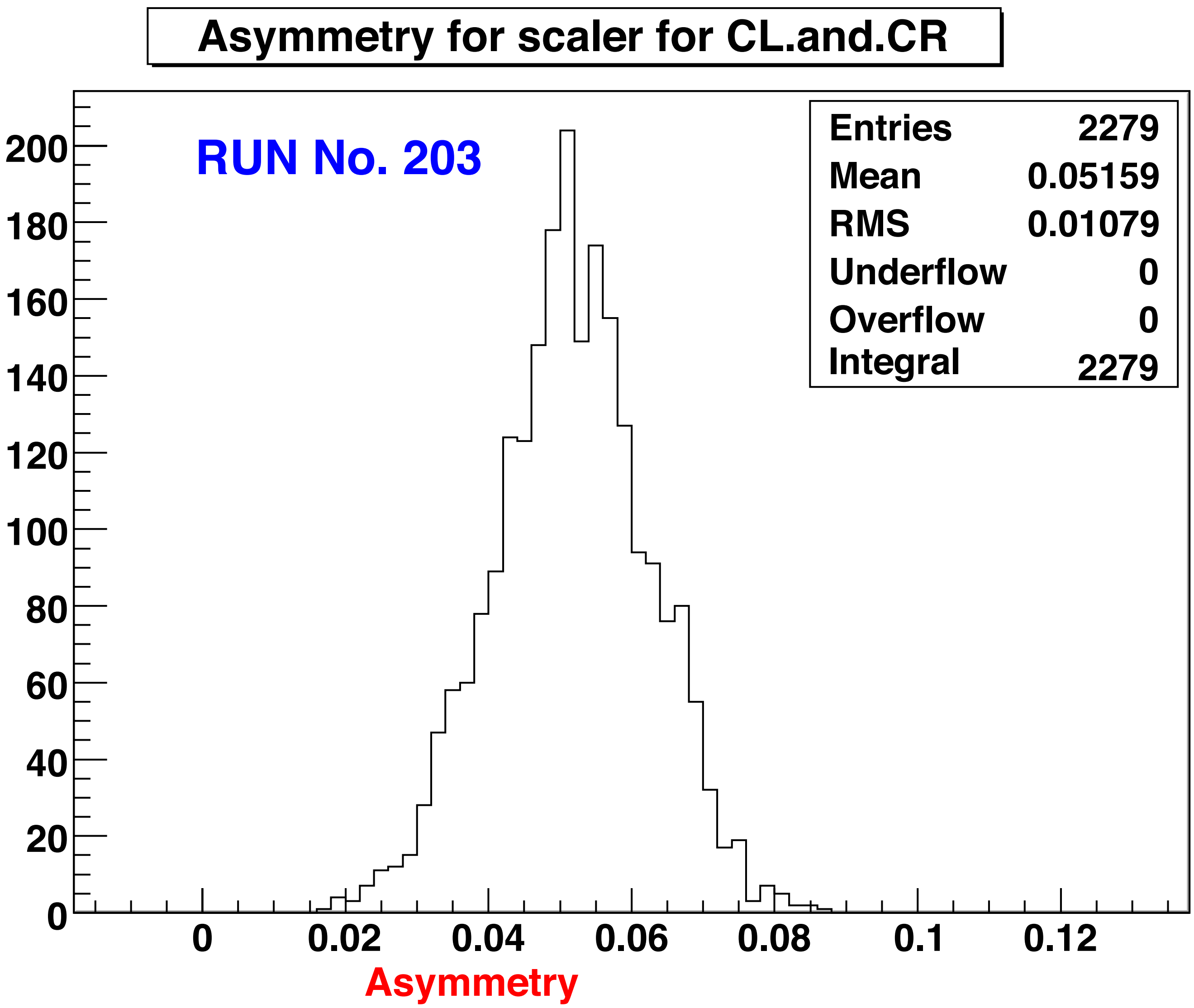

Figure 28: Møller asymmetry measured with on-board scalers in FADC. The 5% asymmetry is normal.

3 Summaries of Experimental Activities

3.1 E94-107

E94-107: High-Resolution Hypernuclear 1p-Shell Spectroscopy

F. Garibaldi, S. Frullani, J. J. LeRose, and P. Markowitz, spokespersons,
and
the Hall A Collaboration.
contributed by F. Cusanno.

The results of the investigation of $^{16}O(e,e'K^+)^{16}_{\Lambda}N$ using a waterfall target [1] are recently published [2], as well as the results of the $^{12}C(e,e'K^+)^{12}_{\Lambda}B$ spectroscopy [3, 4].

The results of the analysis of the $^{9}Be(e,e'K^+)^{9}_{\Lambda}Li$, reported here, are still preliminary. In Fig. 29, the theoretical curve is superimposed on the fitted data. The theoretical cross sections are obtained using the Saclay-Lyon (SLA) model [5] for the elementary $p(e,e'K^+)\Lambda$ reaction. Shell-model wave functions are determined using a parametrization of the ΛN interaction that fits the precise γ-ray hypernuclear spectra of $^{7}_{\Lambda}Li$ [6].
A fit with three peaks is guided by the three main structures predicted by the theory. The fit procedure is described elsewhere [3]. A 600 keV FWHM spread is used for the peaks of the theoretical curve, in agreement with the fitted width of the third peak and with the resolution obtained on $^{12}C(e,e'K^+)^{12}_{\Lambda}B$ and $^{9}Be(e,e'K^+)^{9}_{\Lambda}Li$. The results are reported in the Tab. 3. The value of χ^2/NDF for the fit is 1.34.
If a fit with only two peaks is performed, the FWHM widths of the peaks are 1.0 MeV and 1.7 MeV respectively, and the value of χ^2/NDF is 1.40.

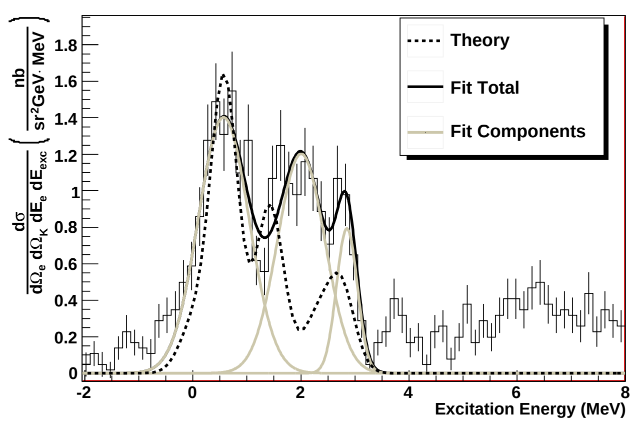

Figure 29: Excitation energy spectrum of the $^{9}Be(e,e'K^+)^{9}_{\Lambda}Li$ fitted with three Voigt functions, compared with theoretical predictions. The width of the peaks in the fit is a free parameter, the width of the single states in the theoretical model is set to 600 keV FWHM.

An attempt to disentangle the different contributions coming from the multiple levels calls for a fit with five peaks, as guided by the theoretical model. Since in principle the width of the peaks should be the same for the single states, determined by the experimental resolution, in this case the fit is performed assuming the same resolution for the single states. The result of this fit for the width of the individual peaks is 710 ± 140 keV FWHM, in agreement with the measurements on $^{12}_{\Lambda}B$ and $^{16}_{\Lambda}N$. The result is shown in Fig. 30. The value of χ^2/NDF for the fit is 1.14.
In any case, the discrepancy between the experimental data and the theoretical curve is rather evident. The comparison of the predictions with the preliminary results is summarized in the Tab. 4.
Precise determination of the binding energy might be possible using the data obtained from the Beryllium windows in the waterfall target, or using the better known binding energy of the $^{12}_{\Lambda}B$, measured during the same beam time with the same setup.

Table 3: Preliminary results of levels obtained by fitting the ${}^{9}\mathrm{Be}(e,e'K^{+})^{9}_{\Lambda}Li$ spectrum assuming three peaks of different widths. The determination of the absolute value of excitation energy, very preliminary, is based on theoretical calculation, assuming the first peak to be the second element of the predicted doublet of the ground state.

	E_x [MeV]	Cross Section[nb/sr^2/GeV]	Width FWHM [MeV]
First Peak	0.58 ± 0.04	1.25 ± 0.15	1.10 ± 0.18
Second Peak	1.96 ± 0.07	1.12 ± 0.15	1.02 ± 0.21
Third Peak	2.83 ± 0.05	0.38 ± 0.11	0.44 ± 0.12

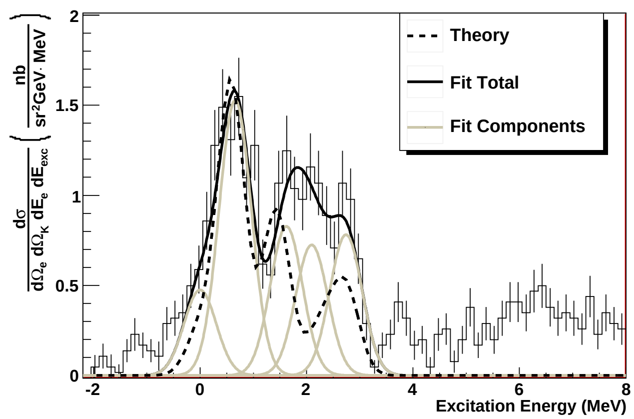

Figure 30: Excitation energy spectrum of the ${}^{9}Be(e,e'K^{+})^{9}_{\Lambda}Li$ fitted with five Voigt functions of the same width, compared with theoretical predictions. The width of the single states in the theoretical model is set to 600 keV FWHM, in agreement with the fit result of 710 ± 140 keV.

References

[1] F. Garibaldi *et al.*, Nucl. Inst. Meth. A **314**, 1 (1992).

[2] F. Cusanno *et al.*, Phys. Rev. Lett. **103**, 202501 (2009).

[3] M. Iodice *et al.*, Phys. Rev. Lett. **99**, 052501 (2007).

[4] J.J. LeRose *et al.*, Nucl. Phys. A **804**, 116 (2008).

[5] T. Mizutani *et al.*, Phys. Rev. C **58**, 75 (1998).

[6] M. Ukai *et al.*, Phys. Rev. C **73** 012501(R) (2006).

Table 4: Preliminary results of levels obtained by fitting the ^{9}Be$(e, e'K^{+})^{9}_{\Lambda}Li$ spectrum assuming five peaks of the same width (first two columns). They are compared to the theoretical predictions, reported in the last three columns.

E_x [MeV]	Cross Section [nb/sr^2/GeV]	E_x [MeV]	J^π	Cross Section [nb/sr^2/GeV]
0.00	0.25 ± 0.13	0	$3/2^+$	0.159
0.73 ± 0.07	1.02 ± 0.25	0.58	$5/2^+$	1.04
1.73 ± 0.34	0.45 ± 0.15	1.43	$1/2^+$, $3/2^+$	0.591
2.12 ± 0.11	0.41 ± 0.14	2.27	$5/2^+$	0.169
2.82 ± 0.04	0.48 ± 0.12	2.73	$7/2^+$	0.311

3.2 E00-102

Testing the Limits of the Single-Particle Model in ^{16}O(e,$e'p$)

A. Saha, W. Bertozzi, L.B. Weinstein, and K. Fissum, spokespersons,
and
the Hall A Collaboration.
contributed by J. L. Herraiz.

Experiment E00-102 is a continuation of the Hall A experiment E89-003: A Measurement of the Cross Section, R_{LT}, and A_{LT} for the ^{16}O(e,$e'p$) Reaction. Experiment E89-003 made measurements at an energy and momentum transfer of ω = 0.445 GeV and Q^2= 0.8 GeV^2 respectively, up to p_m = 0.345 GeV/c [1, 2, 3, 4]. In E00-102, we expanded the existing measurements up to p_m = 0.755 GeV/c at ω = 0.449 GeV and Q^2 = 0.902 GeV^2.

3.2.1 Objectives

The goals of these measurements were to determine:

- the limits of validity of the single-particle model of valence-proton knockout,
- the effects of relativity and spinor distortion on valence-proton knockout using the diffractive character of the A_{LT} asymmetry, and
- the bound-state wave function and spectroscopic factors for valence-proton knockout.

The cross section will be determined from p_m = −0.515 GeV/c to p_m = 0.755 GeV/c, in order to investigate where (and if) single-nucleon knockout calculations fail and two-nucleon effects become important. R_{LT} and A_{LT} will be separated for p_m up to ±0.515 GeV/c to further test relativistic DWIA calculations.

3.2.2 Experimental Setup

Data were taken at a fixed beam energy of 4.620 GeV, q = 1.066 GeV/c, and θ_q = 56.22°. Throughout the entire experiment, the electron arm (HRS-L) was fixed at 12.5° with a central momentum of 4.121 GeV/c, allowing it to be used as a luminosity monitor. The hadron arm (HRS-R) angle was varied from 28.3° to 96.1° to cover the necessary missing-momentum range. These kinematics are shown in Fig. 31. Both detector stacks were used in their standard configurations (Fig. 32). Each stack contained an additional S0 scintillator for checking trigger efficiency, and the HRS-L contained a pion rejector to be used for e/π separation.

The target used was the Hall A self-normalizing three-foil waterfall target [4, 5, 6]. Each water foil was approximately 200 mg/cm^2 thick and separated by 25.4 mm from the other foils. The foils were positioned at an angle of 57.4°with respect to the beam direction, as shown in Fig. 33. Electron scattering from the hydrogen in the water molecule enabled precise calibrations of the experimental apparatus to be made. Further, these measurements also made normalization of the measured ^{16}O(e,$e'p$) cross section to known ^{1}H(e,$e'p$) and ^{1}H(e,e') cross sections possible.

Detector calibrations, beam-position determinations, and beam-energy calibrations have been performed. Optimized detector maps have been created, and the analysis of the spectrometer mispointing has been performed. The water-foil thicknesses have been determined by comparing ^{16}O(e,$e'p$) yields to those obtained from a BeO target of a well-known thickness [7].

3.2.3 Theory

Table 5 contains the parameters of the theoretical models used to describe the ^{16}O($e,e'p$) process. These parameters are the same ones used with good results in the E80-007 experiment [2]. The effect of the nuclear spinor distortion caused by relativistic dynamical effects in this reaction depends on the shell from which the proton is removed. Figure 34 shows that the $p_{1/2}$ shell is more affected by this spinor distortion and that the longitudinal-transverse asymmetry A_{LT} is the best observable to check these effects. Note that this figure represents bare theory, without any experimental acceptance averaging. The spectroscopic factor used in these calculations for both shells was 0.65.

3.2.4 Data Analysis and Simulations

Extensive progress was made at Old Dominion University in adapting the E00-102 analysis [8] to the new ROOT/C++ Hall A Analyzer. This included transferring the optics calibration database used in ESPACE to the new format, creating a model of the waterfall target to calculate energy-loss corrections, and incorporating the LeRose R-functions for detector-acceptance cuts. The results from the new Hall A Analyzer have been sufficiently checked against both ESPACE results and the data, so that we are now confident in their accuracy. We are thus now ready to proceed to use the Hall A Analyzer to analyze all the data acquired during the E00-102 experiment.

Madrid University, in collaboration with Lund University, integrated a fully unfactorized RDWIA model [9] into the MCEEP simulation package. A multidimensional interpolatable grid of nuclear response functions calculated by Udias was generated over a broad range of kinematics and used to weight MCEEP events [10]. This allowed the calculation to be averaged correctly over the finite acceptance of the spectrometers. MCEEP was used to incorporate radiation losses and radiative effects taking into account target thickness and target chamber walls. MCEEP simulations were then converted into ROOT files to ease the comparison with the data.

A C++ macro was developed at Old Dominion University and Madrid University to obtain the cross section from the ROOT files containing the data events obtained with the Hall A Analyzer and the ROOT files containing the simulated events obtained with MCEEP. This macro performs the R-function cuts, the luminosity normalization, the efficiency correction, and the phase-space normalization of both the data files and the simulated files. The macro also applies a cut in missing energy which enables the $1p_{1/2}$, $1p_{3/2}$, or $1s_{1/2}$ shells to be selected. Furthermore, the σ_{ep} factor necessary to determine the reduced cross section is also evaluated based on the prescription of De Forest [11] using the form factors from the Rosenbluth data fitted in [12]. A step-by-step overview of the analysis to date is shown in Fig. 35.

The output of the C++ macro contains histograms of the five-fold differential cross section and reduced cross section for both the data and the simulation for proton removal from ^{16}O. The cross sections so obtained are a function of the physical variables q, ω, p_m, and the out-of-plane angle between the reaction plane and the ejectile plane ϕ. The last step in the data analysis is to determine the differential cross section and the longitudinal-transverse asymmetry A_{LT} as a function of the missing momentum p_m from these multidimensional histograms as shown in Eq. 2

$$\frac{d^5\sigma}{d\omega d\Omega_e d\Omega_p}(q,\omega,\phi,p_{miss}) \rightarrow \left\{ \begin{array}{l} \frac{d^5\sigma}{d\omega d\Omega_e d\Omega_p}(p_{miss}) \\ A_{LT}(p_{miss}) \end{array} \right. \tag{2}$$

We used the reduced cross section to remove the dependence of the five-fold differential cross section on q and ω. Figure 36 shows how the experimental reduced cross section obtained is fairly independent of q and ω. In these results, a cut in ϕ was applied to assure that all p_m bins had the same ϕ range.

We plan to use the reduced five-fold differential cross section together with the full range of ϕ to extract information about the response functions using a fitting procedure.

3.2.5 Preliminary Results

Preliminary results of the reduced cross section and A_{LT} in the p_m region [-350,350] MeV/c have been obtained. The high p_m measured data are currently under analysis. In Fig. 37, the reduced cross section for the $p_{1/2}$ shell as a function of p_m is displayed. Error bars represent statistical uncertainty only. The simulation based on the fully relativistic DWIA model shows good agreement with these results.

Figure 38 shows the longitudinal-transverse asymmetry A_{LT} measured in this experiment, together with A_{LT} from the fully relativistic DWIA simulation and the results from the previous E89-003 experiment. It should be noted that slightly different results from previous experiment are expected, as the kinematical settings are different. The agreement between these data and the simulation is good. The high-p_m data under analysis will reduce the uncertainty in the region $p_m > 300$ MeV/c.

References

[1] W. Bertozzi, K.Fissum, A. Saha, and L. Weinstein, spokespersons, JLab Experiment E89-003 Study of the Quasi-Elastic (e,ep) Reaction in ^{16}O at High Recoil Momentum.

[2] J. Gao *et al.*, Phys. Rev. Lett. **84**, 3265 (2000).

[3] N. Liyanage *et al.*, Phys. Rev. Lett. **86**, 5670 (2001).

[4] K. Fissum *et al.*, Phys. Rev. C **70**, 034606 (2004).

[5] F. Garibaldi *et al.*, Nucl. Instum. Methods. A **314**, 1 (1992).

[6] E. Cisbani *et al.*, A Waterfall Target System for Hall A at JLab, INFN/ISS 97/04 (1997).

[7] B. Reitz *et al.*, E00102 status report, (2005).

[8] J. Lachniet, private communication.

[9] J.M. Udias *et al.*, Phys. Rev. Lett. **83**, 5451 (1999).

[10] J.L. Herraiz, Jefferson Lab Technote JLAB-TN-07-068.

[11] T. de Forest, Jr., Nucl. Phys. A **392**, 232 (1983).

[12] J. Arrington, Phys. Rev. C **69**, 032201(R) (2004).

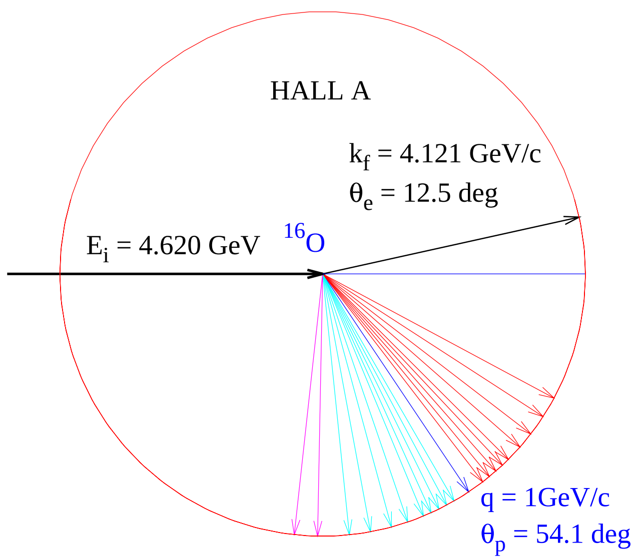

Figure 31: E00-102 kinematics. The beam energy was fixed at 4.620 GeV, and the HRS-L remained fixed at 12.5° with a central momentum of 4.121 GeV/c. The HRS-R was varied around the direction of parallel kinematics to cover the necessary missing-momentum range.

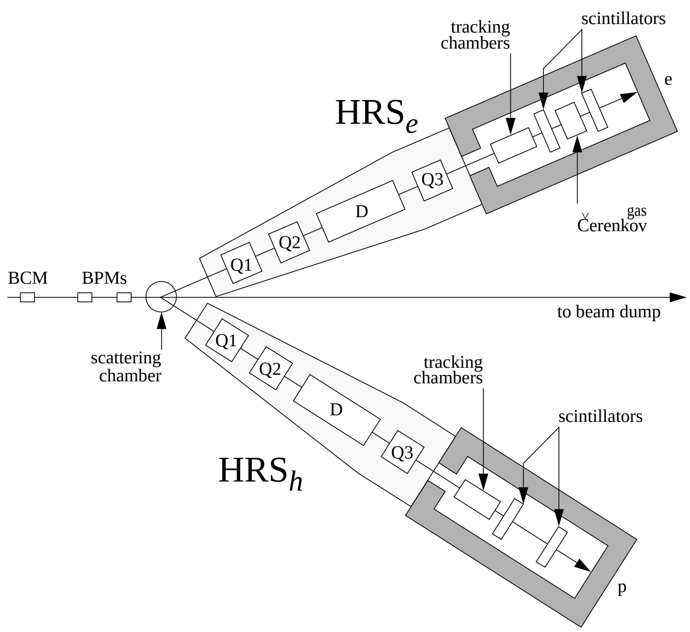

Figure 32: E00-102 HRSs. Detector configuration of the High Resolution Spectrometers during the E00-012 experiment. The A1, A2, and RICH detector were not used in the Left HRS and the Gas Cerenkov detector was not used in the Right HRS.

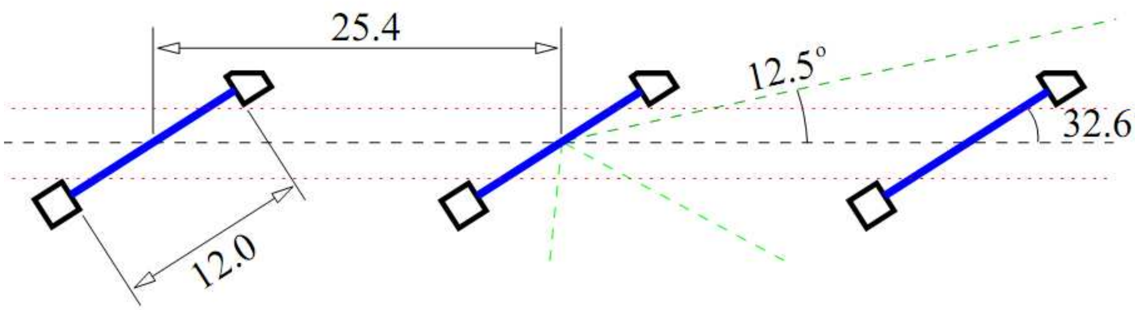

Figure 33: E00-012 waterfall target

Table 5: Parameters of the theoretical models used to compare with the measured data.

Input Parameter	Option
Bound-Nucleon Wave Function	NLSH
Optical Model	EDAI-O
Nuclear Spinor Distortion	Relativistic / Non-Relativistic
Electron Distortion	NONE (yet)
Kinematics	Relativistic
Current Operator	CC2
Nucleon Form Factors	Rosenbluth data fit [11]
Gauge	Coulomb

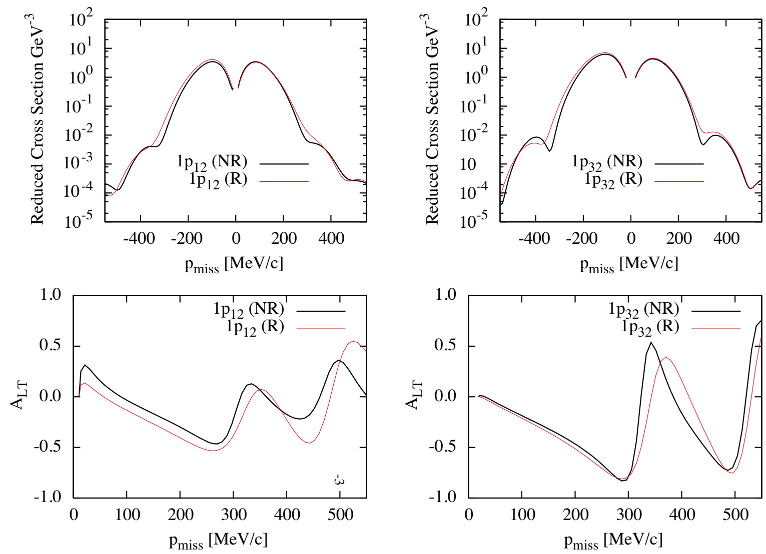

Figure 34: Theoretical predictions with relativistic (red) and non-relativistic (black) dynamical effects. (Top) Reduced cross section (Bottom) Longitudinal-transverse asymmetry A_{LT}. (Left) $p_{1/2}$ shell and (Right) $p_{3/2}$ shell. Note that this represents bare theory without any experimental acceptance averaging.

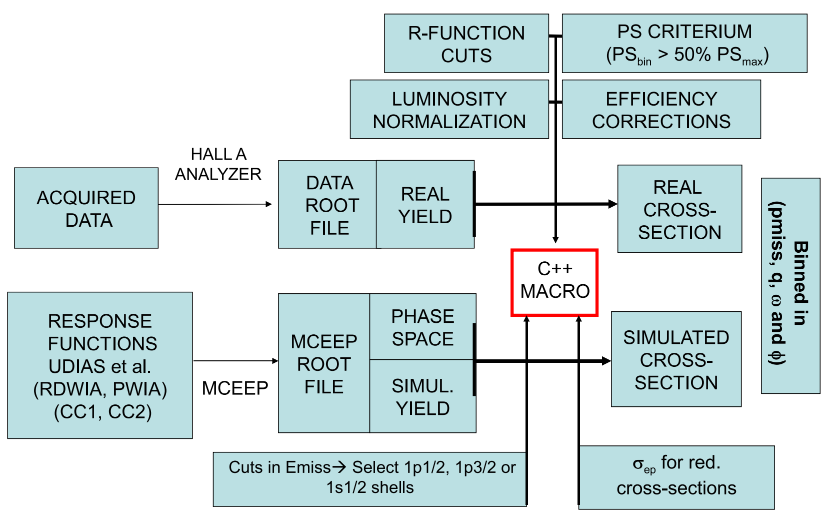

Figure 35: An illustration of the steps followed during the analysis of the E00-102 data.

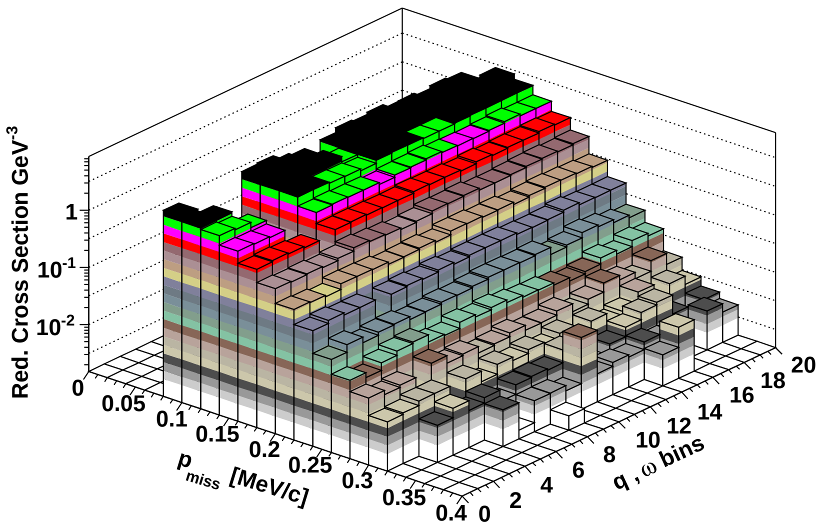

Figure 36: Preliminary results from the E00-102 experiment. Reduced cross section as a function of p_m, q, and ω. The reduced cross section removes the dependence on q and ω.

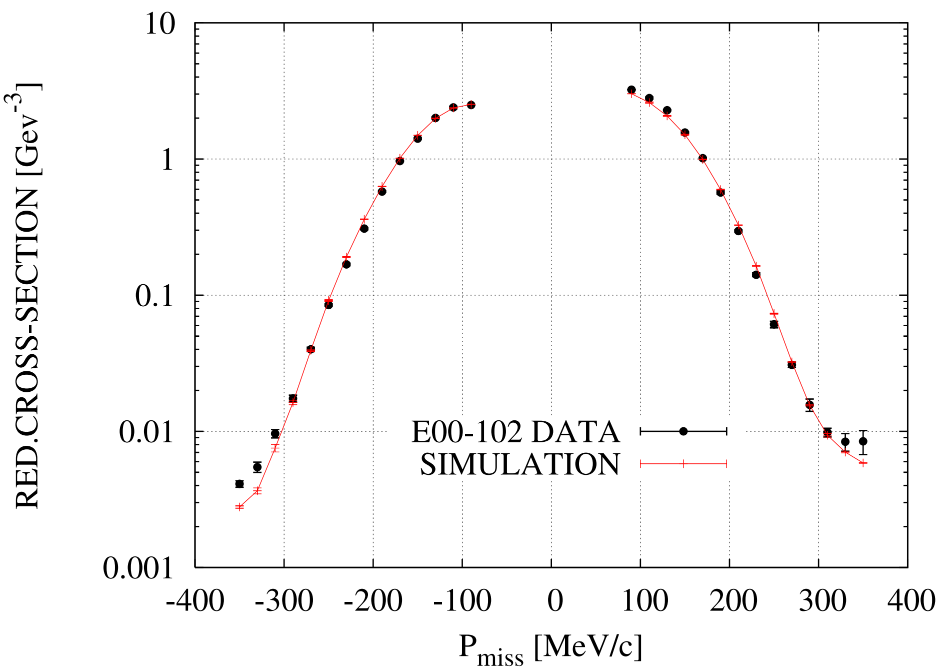

Figure 37: Preliminary results from the E00-102 experiment. Measured (black circles) and simulated (red line) reduced cross section for the removal of protons from the $1p_{1/2}$ shell of ^{16}O. Simulations are based on fully relativistic DWIA response functions

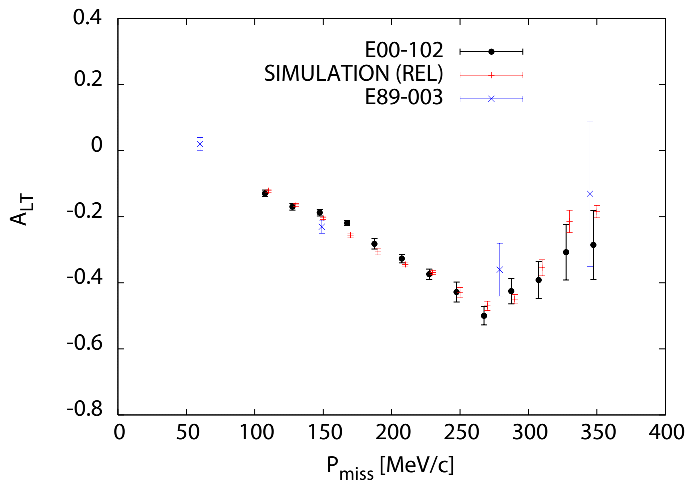

Figure 38: Preliminary results from the E00-102 experiment. Longitudinal-transverse asymmetry measured (black circle) and simulated (red cross) results. The A_{LT} measured in the previous E89-003 experiment is also shown (blue). Simulations are based on fully relativistic DWIA response functions.

3.3 E02-013: Measurement of the Neutron Electric Form Factor G_E^n at High Q^2

Contributed by S. Riordan
G. Cates, N. Liyanage, and B. Wojtsekhowski, spokespersons,
and the E02-013 and the Hall A Collaborations.

3.3.1 Introduction

Nucleon form factors contain crucial information on the structure of nucleons, providing insight into the underlying processes of QCD. They are a useful testing ground for fundamental nucleon models and are currently a crucial source of information in the development of the parameterization of generalized parton distributions [1, 2].

Traditionally, the electric form factor of the neutron, G_E^n, has been the most difficult to measure of the four nucleon form factors. This is due to the relative smallness of G_E^n, as the neutron is an overall neutral particle, and the fact that there are no sufficiently dense free neutron targets, and so the neutron must be bound in a nucleus, typically deuterium or ^{3}He. Prior to E02-013, precision data on G_E^n was limited to momentum transfers of Q^2 less than 1.5 GeV^2. This missing piece has hindered the reliable separation of the Dirac and Pauli form factors for the neutron, F_1^n and F_2^n, which contain unpolarized and polarized transverse structure of the neutron in the infinite momentum frame [3, 4], and of the u and d valence quark form factors.

The E02-013 experiment is a determination of G_E^n through the measurement of the helicity-dependent cross section asymmetry from the reaction $^3\overrightarrow{\mathrm{He}}(\vec{e}, e'n)pp$, quasi-elastic scattering from a transversely polarized ^{3}He target [5]. The measurements were performed at four Q^2 points, 1.2, 1.7, 2.5, and 3.4 GeV^2.

This year the G_E^n collaboration completed the analysis of the three highest Q^2 points and is in the process of submitting a publication to PRL. Primary efforts in finalizing the analysis included studying and improving the method of differentiating recoiling protons and neutrons, using simulations to deconvolute inelastic events from quasi-elastic events, and the completion of calculations of nuclear effects and final state interactions (FSI).

3.3.2 Experiment Overview

Experiment E02-013 measured the electric form factor of the neutron by studying spin asymmetries in quasi-elastic scattering in the reaction $^3\overrightarrow{\mathrm{He}}(\vec{e}, e'n)pp$ at four values of Q^2 up to 3.4 GeV^2. The scattered electron was detected using an open-geometry electron spectrometer, BigBite, with a solid-angle acceptance of 76 msr. The recoiling nucleon was detected in coincidence with a large neutron detector which, with an active detection area of around 8 m^2 at a distance $9 - 12$ m, provides adequate acceptance for quasi-elastic neutrons. A diagram of the physics concept is shown in Fig. 39.

The asymmetry A_{phys} relates to G_E^n through the equation

$$A_{\mathrm{phys}} = -\frac{2\sqrt{\tau(\tau+1)}\tan(\theta/2)G_E^n G_M^n \sin\theta^\star \cos\phi^\star}{(G_E^n)^2 + (G_M^n)^2(\tau + 2\tau(1+\tau)\tan^2(\theta/2))} - \frac{2\tau\sqrt{1+\tau+(1+\tau)^2\tan^2(\theta/2)}\tan(\theta/2)(G_M^n)^2\cos\theta^\star}{(G_E^n)^2 + (G_M^n)^2(\tau + 2\tau(1+\tau)\tan^2(\theta/2))},$$

where $\tau = Q^2/4M^2$, and θ^* and ϕ^* are the polar and the azimuthal angles, respectively, between the polarization direction of the ^{3}He nucleus and the three-momentum transfer, $\vec{q}$. A missing momentum p_{miss}, $(\vec{q} - \vec{p}_N)$, where $\vec{p}_N$ is the momentum of the nucleon, is used for selection quasi-elastic process. The $p_{\mathrm{miss},\perp}$, the component of $\vec{q} - \vec{p}_N$ perpendicular to $\vec{q}$, provides suppression of final state interactions (FSI), allowing for the treatment of quasi-free neutron scattering.

Table 6 shows the kinematics for which data are taken and accumulated beam charge.

3.3.3 Completion of Analysis

Analysis of the G_E^n data for the three highest Q^2 points has been completed. In the last year the three largest efforts were placed on the the development of a GEANT4 based Monte Carlo simulation of the neutron arm,

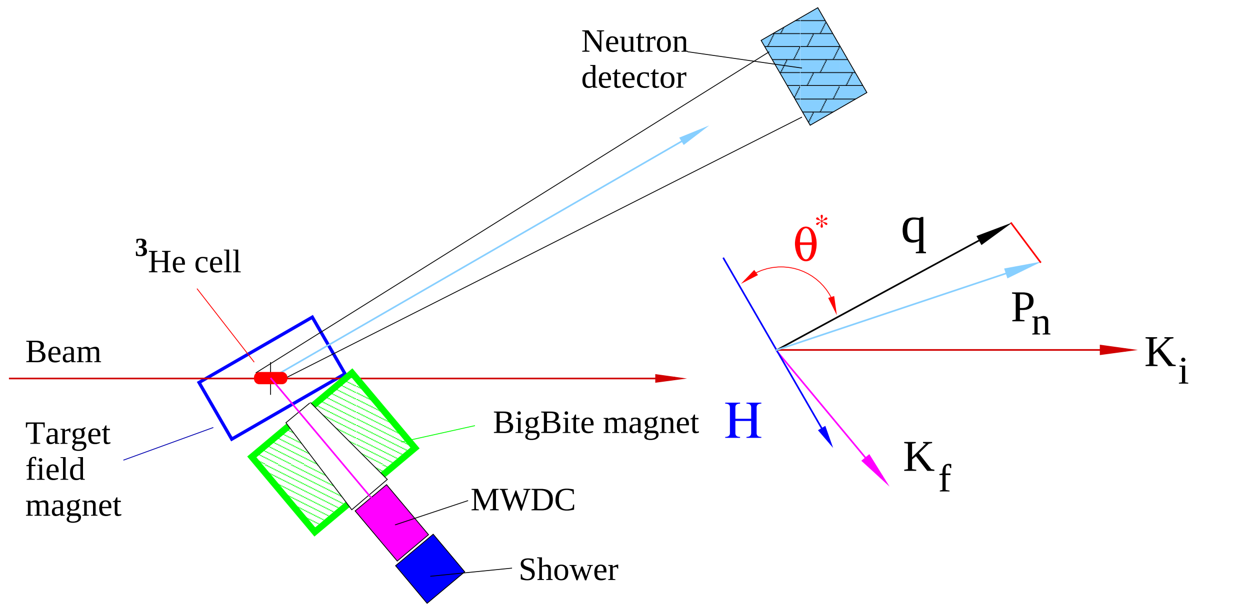

Figure 39: Conceptual lay-out of the E02-013 experiment. Here, $\vec{H}$ indicates the target holding magnetic field; K_i and K_f are the initial and a final electron momenta; $\vec{q} = \vec{K_i} - \vec{K_f}$ is the momentum transfer; $\vec{P_n}$ is the neutron momentum, θ^* is the angle between directions of the magnetic field and the momentum transfer.

Q^2 [GeV^2]	E_{beam} [GeV]	Avg. θ_e [deg]	Q_{beam} [C]
1.2	1.519	56.26	1.2
1.7	2.079	51.59	2.2
2.5	2.640	51.59	5.5
3.4	3.291	51.59	11.4

Table 6: The four kinematics of G_E^n measurements in E02-013 and accumulated beam charge.

the deconvolution of inelastic events from the quasi-elastic sample, and the completion of the calculation of nuclear effects and final state interactions (FSI).

Quasi-elastic Selection The selection of quasi-elastic events is performed by placing cuts on (pseudo-)invariant mass, components of missing momentum, and the missing mass of the reaction $e^3\text{He} \to e'nX$. This allows us to suppress FSI and inelastic events in our sample. Due to finite detector resolution there is some choice in where these cuts are placed, trading quantity of statistics for the purity of quasi-elastic sample. This becomes particularly important at the highest Q^2 points where pion electroproduction plays a more significant role.

In Fig. 40 the quasi-elastic peaks can be clearly seen for the $Q^2 = 1.7$ GeV^2 point, with the selected cuts shown in red. As one goes to higher Q^2, the momentum resolution becomes more degraded due to the higher nucleon momentum measured through time of flight. This degraded resolution increases the presence of inelastic events as our cuts must be widened to compensate the loss of quasi-elastics. The contribution from inelastic events to the asymmetry are then corrected for using a Monte Carlo simulation. The total uncertainty from statistics and the systematic uncertainty in the simulation is minimized by varying the cuts in W and M_{miss}.

Nucleon Charge Identification For a given quasi-elastic scattering event, the detected nucleon in the neutron arm is assigned a charge based on signals in two front-most scintillator planes, known as the veto

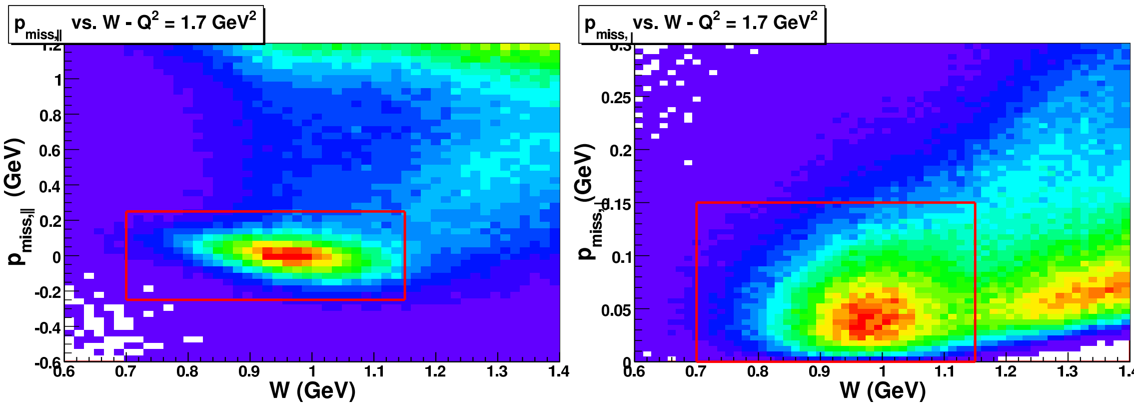

Figure 40: The parallel and perpendicular components of the missing mass, $p_{\text{miss},\parallel}$ and $p_{\text{miss},\perp}$, vs. invariant mass for $Q^2 = 1.7$ GeV^2. The quasi-elastic cut selection is outlined in red.

planes. Several effects may cause charge misidentification which need to be accounted for to properly calculate the neutral sample asymmetry. The dominant effects are natural detector inefficiencies in the veto planes, the interaction of the nucleon while in flight with materials such as the target cell wall and neutron arm shielding, and accidental background producing a false signal in the veto planes.

For all but the last effect, we have developed a technique that allows us to determine the relevant overall conversion probabilities directly from the data, providing knowledge of the purity of our sample. To perform this analysis, we utilize three targets with different nuclear ratios of protons and neutrons, H_2, ^{3}He, and N_2, and examine the response of the neutron arm. By looking at the ratio of the number of identified uncharged to charged nucleons for each of the three targets, it is then possible to sufficiently constrain these conversion rates using the expected uncharged to charged ratios if there was no misidentification.

Due to the differences in the initial momentum distributions of protons and neutron in ^{3}He, placing cuts on missing momentum will produce changes in the relative rates between protons and neutrons. To calculate this, we developed a simulation utilizing realistic nucleon momentum distributions bound in ^{3}He and relating these to the final measured momentum distributions for quasi-elastic scattering. By placing cuts on these final momenta, the effective ratio of protons to neutrons can be determined. For our cuts, the ratio of protons to neutrons was typically 20-40% higher than the naive expectations.

For N_2, a separate PWIA Monte Carlo was performed by J. Udias *et al.* The initial uncharged-to-charged ratio was determined to vary about 10% from naive expectations.

A GEANT4-based Monte Carlo simulation was also used to evaluate the response of the neutron arm for protons and neutrons in our momentum range. Here GEANT4 simulates event-by-event the particle interactions and potential showers and then provides information on the energy deposition in each of our bars. The energy deposition is then converted into time-dependent virtual PMT signals based on responses of the individual detector bars and PMTs. This includes attenuation, reflection, and quantum efficiency effects. This signals are then processed through a set of virtual discriminators and a set of data similar to the real data is produced. Electronic dead-time effects were included as measured from the data for each channel. The rate of additional accidental background was normalized to measured rates from the data. The evaluated time resolution contained some additional smearing to produce a time resolution identical to the data.

This can then be used to give information on the frequency proton and neutron events are assigned to be neutral or charged. The final results of the Monte Carlo simulation for all three points were within the statistical accuracy from the analysis of data in our three-target approach.

Inelastic Separation Our Monte Carlo code was also used to simulate quasi-elastic and inelastic scattering from ^{3}He. In these calculations we were particularly interested in pion electroproduction rates and asymmetries. As a result we were able to increase our quasi-elastic statistics by a factor of 2 from our preliminary values by widening our cuts and then correcting the asymmetry based on the values from the Monte Carlo.

The simulation reproduced the counting rates for elastic H_2 and quasi-elastic ^{3}He scattering, as well as for single pion electroproduction from these targets using the parameterization from the MAID project. This simulation has provided somewhat accurate results up to invariant masses of about 1.4 GeV. The agreement between the data and simulation in the invariant mass spectrum and asymmetry vs. invariant mass is relatively good, Fig. 41. A systematic uncertainty was assigned to the counts and asymmetry based on comparison to a range larger than our cuts in W and two components of missing momenta (each about twice larger than the QE cuts).

An evaluation of the cuts was made to minimize the total uncertainty contributions from the statistics and the systematic error from the Monte Carlo. For the highest Q^2, point where this correction was most relevant, we used cuts which lead about 15% of the events in the final sample as inelastic. For all three points it was observed that the inelastic asymmetry was the same sign and typically within a factor of two of the quasi-elastic asymmetry, reducing the size of the overall correction. For the highest Q^2 point, where the relative systematic uncertainty was 9.7%, the contribution the inelastic events due to normalizations in the Monte Carlo was 5.8%.

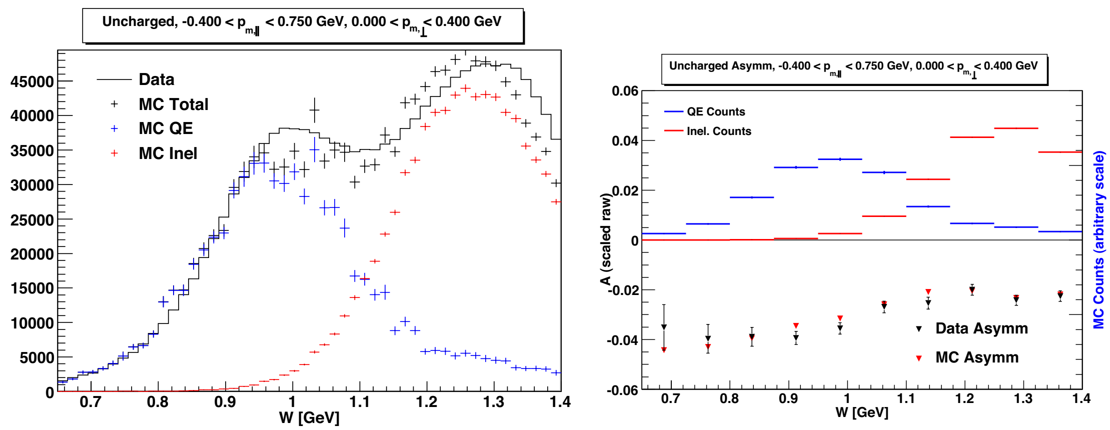

Figure 41: Comparison between the data and the simulation for the invariant-mass spectrum and asymmetry vs. invariant mass with broad cuts for ^{3}He data at $Q^2 = 1.7$ GeV^2.

Effective Neutron Polarization and FSI Since the neutron must be studied bound in a nuclear target, nuclear effects must be taken into account. For quasi-elastic scattering from ^{3}He in our Q^2 range, these are due predominantly to rescattering from spectator nucleons and charge exchange effects. Additionally, the neutron carries some effective polarization and is sensitive to cuts on missing momentum, as these can select on different ^{3}He wave function contributions. For the analysis of E02-013, these were calculated by M. Sargsian in the GEA framework [6].

In this framework, four main diagrams were considered: plane wave impulse approximation, meson exchange currents (MEC), delta isobar currents (IC), and nucleon-nucleon rescattering. At high Q^2 and small missing momenta, MEC and IC effects are highly suppressed. At $p_N > 1$ GeV the proton-proton and proton-neutron cross sections become roughly constant, suggesting that rescattering effects are not necessarily small.

In ^{3}He, a wavefunction can be calculated using a nucleon-nucleon potential from a variety of techniques. For the E02-013 analysis, this was done using the Argonne V18 potential and the wave function calculated by the Bochum group. Also required to describe the photon coupling to a nucleon in a given diagram are nucleon form factor parameterizations, which were taken from a fit by J. Kelly [7] for G_E^p, G_M^p, and G_M^n, and the Galster parameterization for G_E^n. Parameters for our cuts and detector acceptances were included in the calculation. Results were tested to ensure independence of the choice of assumed G_E^n value.

Results for the measured E02-013 points can be found in Table 7. What is notable is that the effective neutron polarization (A PWIA/A Free n) is greater than 95%, significantly higher than the previously assumed 86% effective polarization. The 86% polarization was the result of several calculations which averaged over the entire ^{3}He wavefunction, which is not the case when selecting on specific missing momenta [8]. For the ^{3}He wavefunction, there are two predominant states, and S state where the two proton spins are anti-aligned, and a D state where all three nucleon spins are aligned against the nucleus spin. By selecting on small missing momentum, required to ensure quasi-elastic scattering, one selects more heavily on the S state providing a higher effective neutron polarization.

$\langle Q^2 \rangle$ (GeV^2)	A Free n	A PWIA	A FSI+CHX	$P_{n,\mathrm{eff}}$	$P_{\mathrm{pol+FSI}}$
1.7	-0.2163	-0.2079	-0.1952	0.9612	0.9025
2.5	-0.1635	-0.1592	-0.1509	0.9737	0.9229
3.4	-0.1081	-0.1080	-0.1042	0.9991	0.9648

Table 7: Calculation of combined effective neutron polarization and FSI effect on the final asymmetry compared to that of a free nucleon.

Final Results and Future Analysis The final results for the three highest Q^2 points can be found in Fig. 42 and are to be submitted to PRL very soon. Also plotted are G. Miller's light front cloudy bag model [9], C. Robert's DSE quark-diquark calculation [10], and E. Lomon's VMD model [11], which have been successful in describing the remaining form factors. The three points do not clearly favor any of the three plotted curves. To varying degrees, each of these models use the nucleon form factors as inputs and these new points can be used to to improve agreement.

An interesting point is that at higher Q^2, the DSE/q(qq) model and LFCBM diverge (not shown), with the DSE model predicting a zero-crossing between $Q^2 = 9$ and 10 GeV^2. Planned higher Q^2 measurements will be able to differentiate between these two models providing information on the relevant physics behind the neutron's structure.

Also interesting is to look at the expected perturbative QCD (pQCD) scaling behavior determined by Belitsky et al. [12], which in the case of the proton, appears to set in surprisingly early at about 2 GeV^2. Scaling this curve of the same form to a point between the highest Madey point and our lowest Q^2 point, we do not see such behavior implying that we are not yet in the pQCD regime for this range of momentum transfer.

In Fig. 43 we have performed a separation of the Dirac and Pauli form factors and a quark flavor separation based on charge symmetry. Plotted are results from a lattice calculation [13] and a GPD parameterization from M. Diehl [1] which uses the form factors as a constraint. We see agreement with our data and the lattice calculation. For the GPD model there is agreement with the F_1^d/F_1^u ratio, which is dominated by G_M at high Q^2, but must be refit using our data for F_2^d/F_2^u.

Analysis for the $Q^2 = 1.2$ GeV^2 point is also underway and is expected to also be completed in 2010. Work on a longer paper detailing our experiment and analysis of all four points is underway and is anticipated to be submitted to Phys. Rev. C sometime in 2010.

References

[1] M. Diehl et al., Eur. Phys. J. C **39** 1, 2005.

[2] M. Guidal et al., Phys. Rev. D **72** 054013, 2005.

[3] G. Miller and J. Arrington, Phys. Rev. C **78** 032201, 2008.

[4] C. Carlson and M. Vanderhaegen, Phys. Rev. Lett. **100** 032004, 2008.

[5] Jeffereson Lab Hall A E02-013, G. Cates, N. Liyanage, and B. Wojtsekhowski

[6] M. Sargsian, Int. Jour. of Mod. Phys. E **10** 405, 2001.

[7] J.J. Kelly, Phys. Rev. C **70** 068202, 2004.

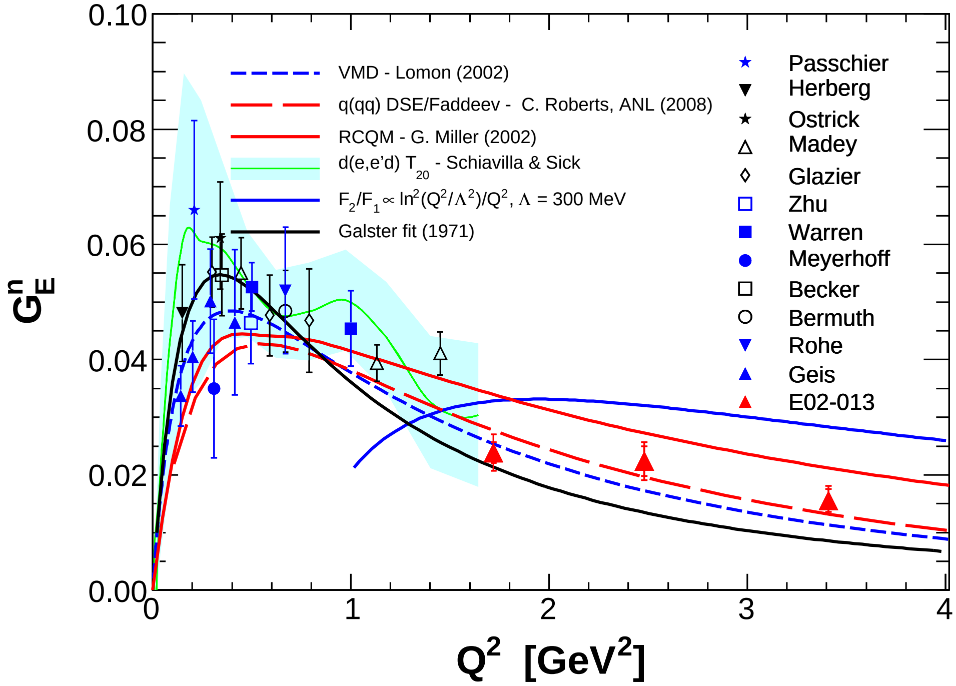

Figure 42: Results for the three highest Q^2-points for E02-013. Included are various theory curves, discussed in the text.

[8] J. Carlson and R. Schiavilla, Rev. Mod. Phys. **70** 743, 1998.

[9] G. Miller, Phys. Rev. C **66** 032201, 2002.

[10] C.D. Roberts *et al.*, Eur. Phys. J. **ST 140** 53, 2007; I.C. Cloët *et al.*, Few-Body Systems **46** 1, 2009.

[11] E. L. Lomon, Phys. Rev. C **64** 035204, 2001.

[12] A. Belitsky, X. Ji and F. Yuan, Phys. Rev. Lett. **91** 092003, 2003.

[13] M. Göckeler *et al.*, PoS **LAT2006** 120, 2006.

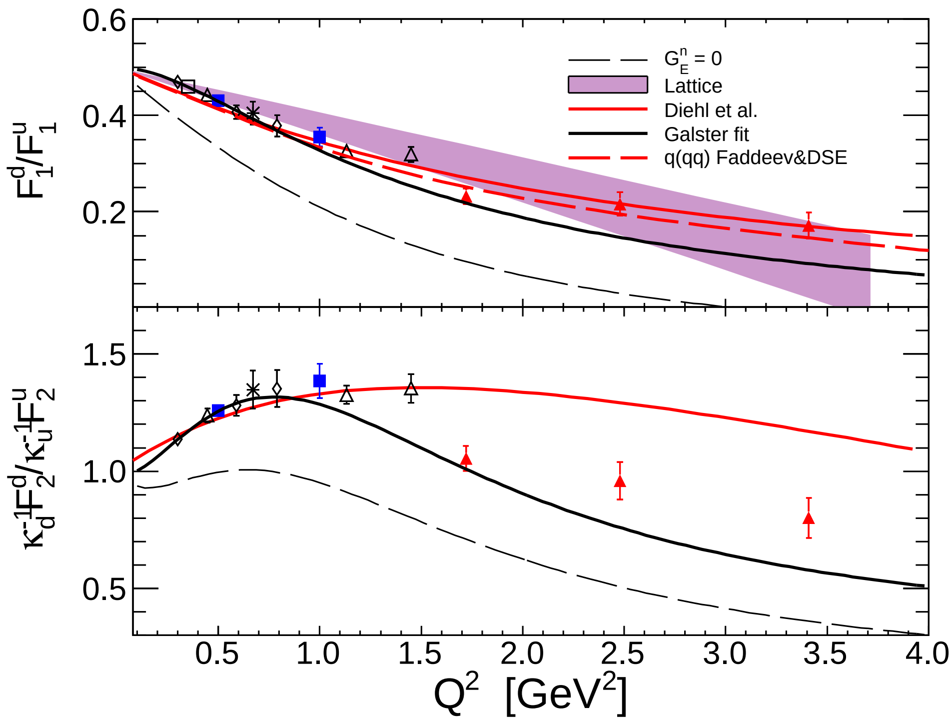

Figure 43: Dirac and Pauli quark flavor ratios using the Kelly parameterization [7] for the remaining form factors. Included are various theory curves, discussed in the text.

3.4 E03-101

Hard Photodisintegration of a Proton Pair

R. Gilman and E. Piasetzky, spokespersons,
D.W. Higinbotham, S. Strauch and
the Hall A Collaboration.
contributed by I. Pomerantz.

Extensive studies of high-energy deuteron photodisintegration over the past two decades have probed the limits of meson-baryon descriptions of nuclei and reactions [1, 2, 3, 4, 5], and the effects of the underlying quark-gluon degrees of freedom. At low energies, up through the region of Δ resonance excitation, photodisintegration of the deuteron is well understood, although certain detailed problems remain [6, 7, 8, 9]. Above $\sim$1 GeV, deuteron photodisintegration cross sections have been shown to follow the constituent counting rules [10, 11, 12, 13, 14], which have been derived from dimensional analysis, QCD and AdS/CFT correspondence [13, 15, 16].

We define a hard photodisintegration of a nucleon pair as a process in which a high energy photon is absorbed by a nucleon pair and as a result the pair is disintegrated by emitting two nucleons with large transverse momenta, greater than about 1 GeV/c. As defined, in this process the Mandelstam parameters s and t (the square of the total energy in the c.m. frame, and the four-momentum transfer from the photon to the nucleon), are large.

In an attempt to more clearly identify the underlying dynamics at play in high-energy photodisintegration, E03-101 measured the hard photodisintegration of two protons, using ^{3}He. The basic idea is that theoretical models should be able to predict the relative size of pp versus pn disintegration [17]. Also, if the pp and pn disintegration are related to the corresponding pp and pn elastic scattering via hard re-scattering [18], deviations from power scaling in the elastic scattering should be reflected in corresponding differences in the photodisintegration processes.

Experiment E03-101 ran in Hall A during the summer of 2007 and measured the cross section of the photodisintegration of a proton pair in ^{3}He at $\theta_{c.m.} = 90^\circ$ for photon energies in the range of 0.8 - 4.7 GeV [19]. Figure 44 shows the $\gamma + \mathrm{d} \to p + n$ and $\gamma + {}^3\mathrm{He} \to p + p + n$ cross section at $\theta_{c.m.} = 90^\circ$ scaled by s^{11}. The ^{3}He(γ,pp)n events were selected with $p_n < 100$ MeV/c. The cross section is compared to theoretical models, discussed below, that produced predictions for the photodisintegration of both pn and pp pairs [17].

Our new data along with previous low-energy data indicate that the ^{3}He two-proton disintegration can be divided into three energy regions. At *low* photon energies (below $E_\gamma \approx 0.5$ GeV), the dynamics of $\theta_{c.m.} = 90^\circ$ proton-pair breakup is governed by hadron and meson degrees of freedom and the cross section has a large three-body component [20].

In a *transition* region (1 GeV < E_γ < 2.2 GeV) the scaled cross section for deuteron (pn pairs) breakup is flat while for pp pairs a significant structure is observed. This structure may be the result of resonances in the γN or γNN systems. The energy dependence in the transition region more closely resembles the energy behavior of the photo-induced pion production [21, 22, 23] than that of deuteron photo-disintegration. It has been suggested that the structure might result from a meson photo-produced on a proton and then absorbed on a pn pair [24].

In the *scaling* region the cross section for both pn and pp breakup scales in agreement with the constituent counting rule [13, 15, 16]. For proton-pair break-up, the onset of the scaling is at $E_\gamma \approx 2.2$ GeV, while for pn pairs scaling commences at $E_\gamma \approx 1$ GeV [5]. The scaling in the ^{3}He case indicates that in this regime the two-body process is dominant. It further suggests (in a relatively model-independent way) that the relevant degrees of freedom that govern the dynamics are the quarks. In a hadronic picture, two-body/one-step processes are strongly suppressed since no charged pion can be exchanged between the protons.

The reduced nuclear amplitude (RNA) formalism after normalization to the deuteron data [17] yields cross sections that are about 200 times larger than the present data. The quark-gluon string model (QGS) [25, 26], as estimated in [17], predicts cross sections about a factor of 5 larger than measured. The QCD hard re-scattering model (HRM) [27] allows an absolute calculation of the cross sections for both pn and pp pair photodisintegration from nucleon-nucleon measured cross sections without adjustable parameters. It reproduces reasonably well the deuteron data and the proton pair cross section. The HRM model predicts a deviation from the scaling of the cross section that the data is not accurate enough to either confirm or reject.

An explanation for the low magnitude of the scaled cross section of proton-pair breakup is given in the HRM [18] by a cancellation of the opposite sign of the NN helicity amplitudes ϕ_3 and ϕ_4 in the *pp* breakup [1]. The energy dependence predicted by the HRM in the scaling region agrees well with the data. Therefore, hard re-scattering is a plausible explanation for the origin of the large transverse momenta. Models that hold compact NN pairs in the initial state to be the reason for the large transverse momenta [28] would have to assume either a fairly low abundance of *pp* pairs within the ^{3}He wave function or the same type of nuclear amplitude cancellation in order to explain the low magnitude of the *pp* break-up scaled cross section.

Another possible explanation for the cross-section magnitude may lie in tensor correlations [29, 30, 31]. These nucleon-nucleon correlations cause the ratio of *pp* to *np* pairs to be $\sim$5% in the relative momentum range of 300-600 MeV/c for both high-energy electron and proton scattering [32, 33, 34]. Starting with such a pair and final state re-scattering might lead to the observed relative transverse momentum and would explain the relatively small cross sections.

References

[1] E. Schulte *et al.*, Phys. Rev. Lett. **87**, 102302 (2001).

[2] J. Napolitano *et al.*, Phys. Rev. Lett. **61**, 2530 (1988); S.J. Freedman *et al.*, Phys. Rev. C **48**, 1864 (1993).

[3] J.E. Belz *et al.*, Phys. Rev. Lett. **74**, 646 (1995).

[4] C. Bochna *et al.*, Phys. Rev. Lett. **81**, 4576 (1998).

[5] E. Schulte *et al.*, Phys. Rev. C **66**, 042201R (2002).

[6] H. Arenhoevel, E. M. Darwish, A. Fix, and M. Schwamb, Mod. Phys. Lett. A **18**, 190 (2003), nucl-th/0209083.

[7] M. Schwamb and H. Arenhovel, Nucl. Phys. A **696**, 556 (2001), nucl-th/0105033.

[8] M. Schwamb and H. Arenhovel, Nucl. Phys. A **690**, 647 (2001), nucl-th/9912017.

[9] R. Schiavilla, Phys. Rev. C **72**, 034001 (2005), nucl-th/0505066.

[10] P. Rossi et al., Phys. Rev. Lett. **94**, 012301 (2005), hep-ph/0405207.

[11] S. J. Brodsky and B. T. Chertok, Phys. Rev. Lett. **37**, 269 (1976).

[12] S. J. Brodsky and B. T. Chertok, Phys. Rev. D **14**, 3003 (1976).

[13] S. J. Brodsky and G. R. Farrar, Phys. Rev. Lett. **31**, 1153 (1973).

[14] V. A. Matveev, R. M. Muradian, and A. N. Tavkhelidze, Nuovo Cim. Lett. **7**, 719 (1973).

[15] G. P. Lepage and S. J. Brodsky, Phys. Rev. D **22**, 2157 (1980).

[16] J. Polchinski and M. J. Strassler, Phys. Rev. Lett. **88**, 031601 (2002), hep-th/0109174.

[17] S. J. Brodsky et al., Phys. Lett. **B578**, 69 (2004), nucl-th/0305068.

[18] M. M. Sargsian and C. Granados, Phys. Rev. C **80**, 014612 (2009), 0812.4590.

[19] E03-101, http://hallaweb.jlab.org/experiment/E03-101.

[1] ϕ_3 and ϕ_4 are the NN elastic-scattering helicity amplitudes that connect zero helicity in the initial states to zero helicity in the final state, ϕ_3 does it with no helicity exchange, while ϕ_4 exchanges helicity between the scattered nucleons. This cancellation of ϕ_3 and ϕ_4 was not recognized in [17].

[20] J. M. Laget, Phys. Lett. **B151**, 325 (1985).

[21] H. J. Besch, F. Krautschneider, K. P. Sternemann, W. Vollrath, Z. Phys. C **16**, 1 (1982).

[22] P. Benz, et al., Nucl. Phys. B **65**, 158 (1973).

[23] L. Y. Zhu, et al., Phys. Rev. C **71**, 044603 (2005).

[24] J. M. Laget, private communication.

[25] V. Y. Grishina et al., Eur. Phys. J. **A10**, 355 (2001), hep-ph/0101129.

[26] V. Y. Grishina et al., Eur. Phys. J. **A18**, 207 (2003), nucl-th/0209076.

[27] L. L. Frankfurt, G. A. Miller, M. M. Sargsian, and M. I. Strikman, Phys. Rev. Lett. **84**, 3045 (2000), hep-ph/9904222.

[28] S. J. Brodsky, J. R. Hiller, Phys. Rev. C **28**, 475 (1983).

[29] M. M. Sargsian, T. V. Abrahamyan, M. I. Strikman, L. L. Frankfurt, Phys. Rev. C **71**, 044615 (2005).

[30] R. Schiavilla, R. B. Wiringa, S. C. Pieper, J. Carlson, Phys. Rev. Lett. **98**, 132501 (2007).

[31] M. Alvioli, C. Ciofi degli Atti, H. Morita, Phys. Rev. Lett. **100**, 162503 (2008).

[32] E. Piasetzky, M. Sargsian, L. Frankfurt, M. Strikman, J. W. Watson, Phys. Rev. Lett. **97**, 162504 (2006).

[33] R. Shneor, et al., Phys. Rev. Lett. **99**, 072501 (2007).

[34] R. Subedi, et al., Science **320**, 1476 (2008).

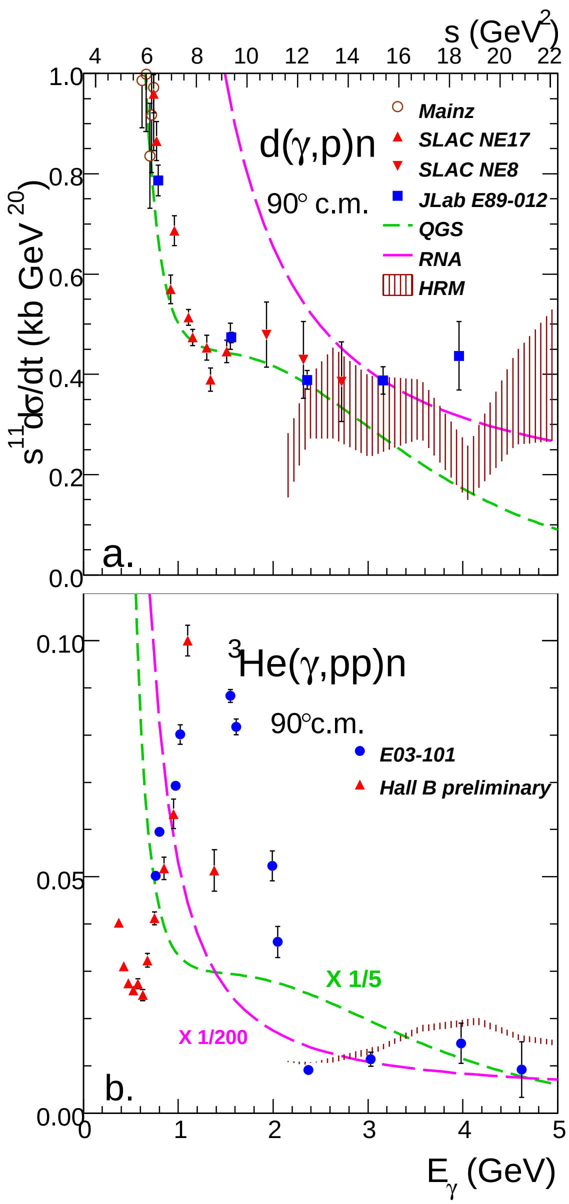

Figure 44: The d(γ,p)n (a) and ^{3}He(γ,pp)n (b) invariant cross section scaled by s^{11}. ^{3}He(γ,pp)n events were selected with $p_n < 100$ MeV/c. Up to 2.1 GeV, the photon energy bins are 70 MeV, and above it 140 MeV. Model predictions are taken from [17, 18]. In (b), RNA is divided by a factor of 200 and QGS by a factor of 5 to be shown on this scale. Error bars represent statistical uncertainty.

3.5 E04-007

Near Threshold Pion Electroproduction

Miha Mihovilovic
for
the E04-007 Collaboration.

A precise knowledge of the energy transfer near pion threshold is very important to the E04-007 experiment to correctly produce the cross section as a function of energy above threshold. To do this, the energy of the incident electrons should be known to a relative accuracy better than 10^{-3} (about 1 MeV absolute). Unfortunately, the beam energy lock was not operational for Hall A during most of this experiment. Consequently, the beam energy was drifting, and significant changes in energy could be observed even within a single run. In order to analyze our data correctly we therefore have to rely on the Tiefenbach energy measurements that are recorded as EPICS information in raw data files every few seconds.

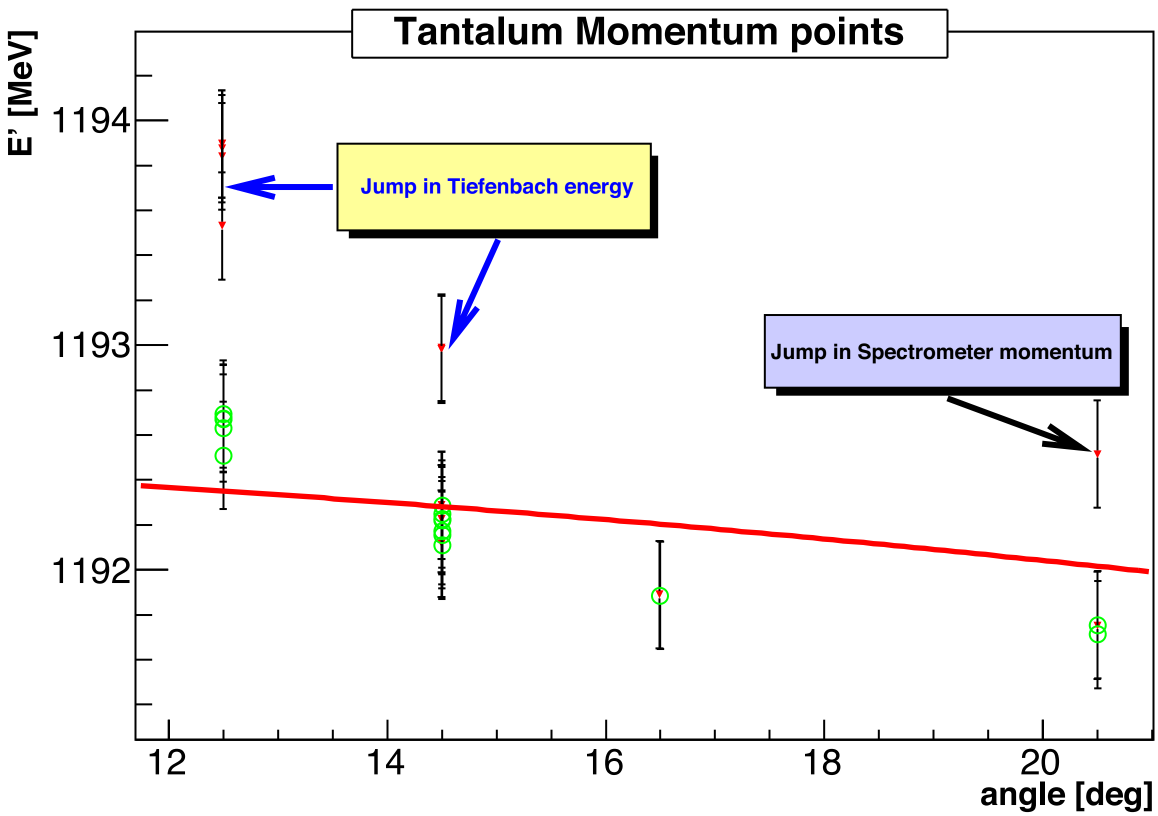

Figure 45: Reconstructed energy of the scattered electrons E' for elastic Tantalum runs taken during the E04-007 experiment at different scattering angles (red points). The red line represents the calculated energy of the scattered electrons, using equation (3) for a fixed beam energy $E_0 = 1192.55$ MeV and fixed momentum of the spectrometer $p_c = 1194.1$ MeV/c. A rough estimation of the energy losses $\Delta E \approx 0.38$ MeV was used. The deviations of the measured points from the theoretical curve represent a change in beam energy or a change in the momentum of the spectrometer for particular runs. After correcting these measurements for the change in p_c and in the Tiefenbach energy, all measured points become consistent (green circles). This indicates that we understand the behavior of the spectrometer and that relative changes in the Tiefenbach energy correspond to relative changes in the true energy.

Since the Tiefenbach readouts were not intended for this purpose, it is important to estimate how accurate the readouts are and to determine the transformation between these values and the true beam energy. The idea is to use the inverse of this transformation to calculate the beam energy from the Tiefenbach energy. To determine this correlation we have used elastic data on tantalum, aluminum, carbon, and hydrogen targets at different scattering angles. The analysis of these data can give us a very precise knowledge of the beam energy. Knowing the central momentum of the spectrometers p_c (this is known to an accuracy of about 5×10^{-5}) and the electron energy losses before and after the scattering ΔE, $\Delta E'$ we can determine the beam energy using the relation:

$$E = \Delta E + \frac{E' + \Delta E'}{1 + \frac{E' + \Delta E'}{M}(1 - \cos\theta_e)} \tag{3}$$

The beam energy analysis is still in progress. At this point we believe that Tiefenbach measurements are relatively correct (see Fig. 45). This implies that there is only a constant difference between the true beam energy and the Tiefenbach readouts. To determine this offset we are currently trying to estimate the energy losses of the electrons on their path from the target to the spectrometer. Once we understand the losses we will be able to determine the difference directly. With the current rough estimate of the energy loss, the difference between the Tiefenbach and the reconstructed beam energy is $E_{Tiefenbach} - E_{elastic} \approx 0.2\,\mathrm{MeV}$ which is well within the 0.5 MeV (dE/E of 5×10^{-4}) that is typically quoted for the accuracy of the Tiefenbach energy.

3.6 E05-015, E05-102, and E08-005

Quasi-Elastic Polarized ^{3}He Family

contributed by
Jin Ge, Ellie Long, Miha Mihovilovic and Ya Wei (Ph.D. Students)
Vince Sulkosky and Bo Zhao (Postdocs)

3.6.1 Introduction

A family of three quasi-elastic polarized ^{3}He experiments(E05-015, E05-102, and E08-005) successfully ran in the summer of 2009 [1, 2, 3] . These experiments will address a number of fundamental issues in nuclear physics including two-photon effects and understanding the three-body wave-function. As the analysis of these data is just beginning, this report focuses on a number of general issues: kinematics and lay-out of the experiment, measurements of the thickness of the glass ^{3}He targets, details of the trigger lay-out, and the optics calibration of the HRS spectrometers.

3.6.2 Quasi-Elastic Family Lay-out

The quasi-elastic family of ^{3}He experiments made use of the two HRS spectrometers for electron detection, the BigBite spectrometer for proton and deuteron detection, and the Hall A Neutron Detector (HAND) for neutron detection. In addition, a new set of Helmholtz coils was added to the ^{3}He target so it could be polarized in three orthogonal directions. A complete list of the setups used during this experiment can be found in Table 8 along with a diagram in Fig. 46.

Table 8: The kinematics settings for the Quasi-Elastic family of experiments. Every new line corresponds to a change in the kinematics during the experiments. In chronological order there are the beam energy E_0, the right HRS central angle, the right HRS momentum p_R, the left HRS central angle, the left HRS momentum p_L), the Hall A Neutron Detector (HAND) central angle, and the BigBite spectrometer central angle.

Date	E_0 [GeV]	RHRS [°]	RHRS [GeV/c]	LHRS [°]	LHRS [GeV/c]	HAND [°]	BigBite [°]
4/26	1.245	-17.0	1.2205	17.0	1.2205	71.0	-74
4/27	1.245	-17.0	1.1759	17.0	1.1759	71.0	-74
4/29	3.605	-17.0	3.0855	17.0	3.0855	54.0	-74
5/6	3.605	-17.0	3.0855	17.0	3.0855	62.5	-74
5/8	2.425	-17.0	2.1813	17.0	2.1813	62.5	-74
5/12	2.425	-16.0	2.2500	14.5	2.3000	62.5	-75
5/15	2.425	-16.0	2.2250	14.5	2.3000	62.5	-75
5/17	2.425	-16.0	2.2250	14.5	2.2770	62.5	-75
5/26	2.425	-18.0	2.1750	14.5	2.2770	62.5	-82
6/1	2.425	-18.0	2.1750	12.5	2.4000	62.5	-75
6/1	2.425	-18.0	2.1750	12.5	2.3200	62.5	-75
6/2	2.425	-18.0	2.1750	12.5	2.4360	62.5	-75
6/3	2.425	-18.0	2.1750	12.5	2.3200	62.5	-75
6/10	2.425	-18.0	1.8650	12.5	2.3200	62.5	-75
6/11	2.425	-18.0	0.7000	12.5	2.3200	54.0	-75
6/11	2.425	-18.0	2.1750	12.5	2.3200	54.0	-75
6/11	2.425	-18.0	2.0250	12.5	2.3200	54.0	-75
6/12	3.606	-17.0	3.0855	12.5	3.3500	54.0	-75

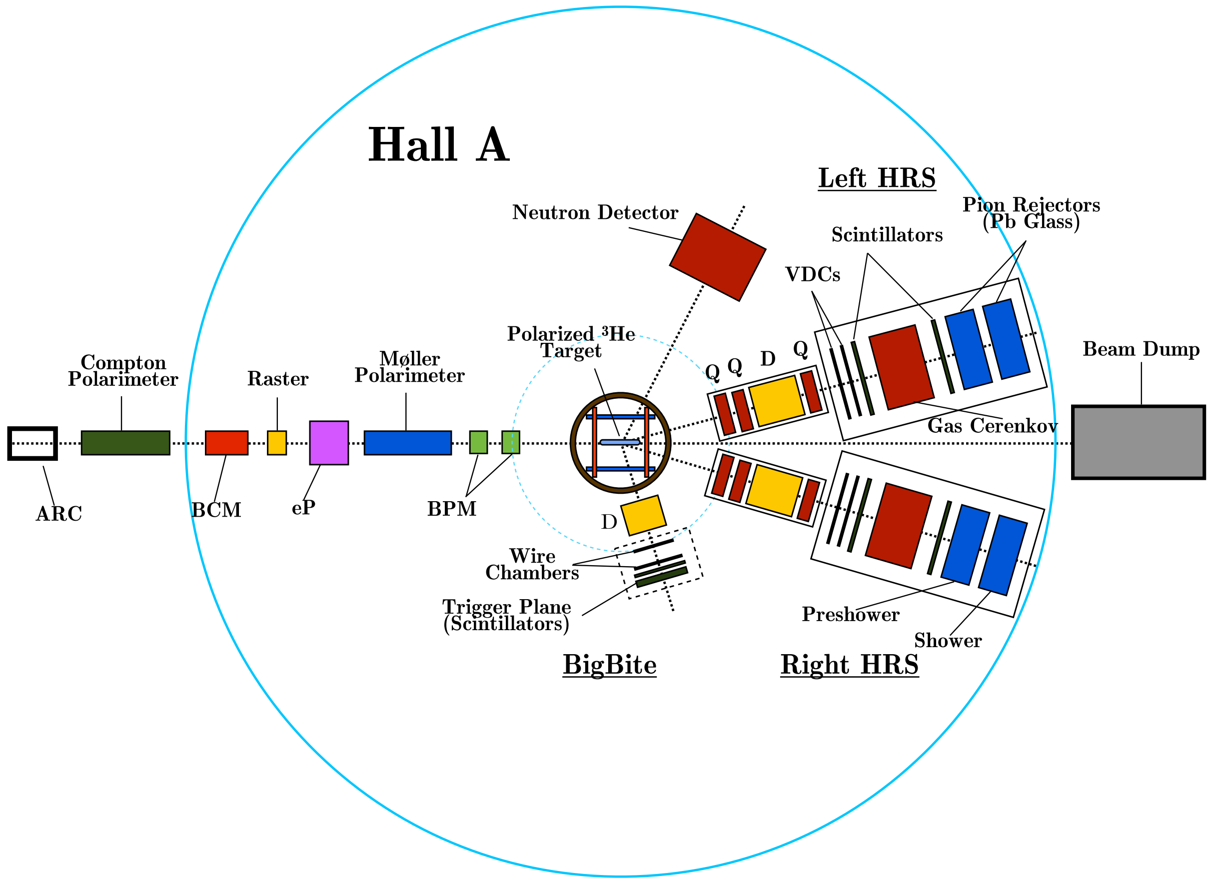

Figure 46: Hall A lay-out during the Quasi-Elastic Family of Experiments. The beam line downstream from the target corresponds to a 0.0° angle. The right HRS was set with central angles between -16.0° and -18.0° with momentum range of 0.7000 to 3.0855 GeV/c. The left HRS was set at central angles between 12.5° and 17.0° with momentum range of 1.1759 to 3.3500 GeV/c. The Hall A Neutron Detector was set at central angles between 54.0° and 71.0°. The BigBite spectrometer was set at central angles between -74° and 82°. More details on the kinematics settings can be found in Table 8. The HRS detector packages consisted of VDCs, S1 and S2 scintillators, a gas Cerenkov, and two layers of lead glass. The BigBite spectrometer contained two multiwire drift chambers, dE scintillator plane, and E scintillator plane. The Hall A Neutron Detector consisted of a layer of veto scintillators and four layers of 10 cm wide scintillators.

3.6.3 Target glass thickness measurement

The objective of the wall thickness study is to determine the thickness of the target cell glass. During the experiment, a polarized ^{3}He target was used, where the incoming and outgoing electrons lose energy when they pass through the cell windows and walls. Knowledge of the cell's thickness is mandatory to perform a reasonable estimate of the radiative corrections.

When two or more sources of light interact with each other in phase space, they produce a series of alternating bright or dark fringes as a result of their constructive or destructive interference, which depends on the relative phase of the interacting waves. The interference pattern occurs when the interacting waves are either correlated or coherent with each other, or they are produced from the same source and have the same frequency.

The measurement of a transparent thin-film thickness is conducted by detecting reflected laser light from the front and the back surface of this film. As is shown in Fig. 47, the incident laser scatters off the glass producing waves that reflect from the front surface and others that refract and then reflect from the back surface. A constructive or destructive interference occurs when the second wave is refracted back through the film and then interferes with the reflected wave from the front surface. The type of interference depends on the optical path length difference; and hence, the relative phase of the interacting waves [5].

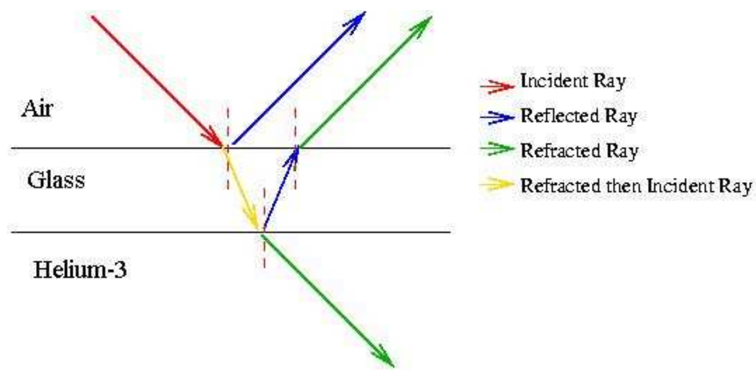

Figure 47: Illustration of the interference phenomenon.

In this study, several data scans have been taken to measure the glass thickness of the polarized ^{3}He and reference cells. The cells that were used during the E05-015 and E05-102 experiments are:

- Reference cell: GMB2 (E05-015 and E05-102)
- ^{3}He cells:
  - Dominic (E05-015)
  - Moss (E05-102).

Tables 9, 10 and 11 provide a summary of the wall and window thicknesses for the three different target cells compared to measurements conducted at the University of Virginia (UVA). The statistical uncertainty for each measurement is about 2%; the main systematic uncertainty is caused by the uncertainty in the laser light's incident angle on the glass, which translates into $< 1\%$ error on the thickness measurements.

Table 9: Reference cell: GMB2 wall and window thickness summary.

Points	Incident Angle [°]	Fitting Results [mm]	UVA Results [mm]
A	14.5	1.679	1.58
B	3	1.699	1.66
C	7.5	1.702	1.67
D	9	1.712	1.51
E	10	1.591	1.61
F	9	1.610	1.48
G	4	1.547	1.70
H	7	1.533	1.78
I	6	1.514	1.61
J	5	N/A	1.63
W1	6.5	0.141	0.151
W2	13	0.134	0.132

Table 10: ^{3}He cell: Dominic wall and window thickness summary.

Points	Incident Angle [°]	Fitting Results [mm]	UVA Results [mm]
A	3	1.691	1.55
B	6.5	1.702	1.62
C	6.5	1.716	1.64
D	8.5	1.691	1.67
E	11.5	1.656	1.67
F	8	1.598	1.62
G	7	1.710	1.72
H	8.5	1.695	1.63
I	9	1.662	1.63
J	8	1.654	1.75
W1	16	0.139	0.132
W2	17.5	0.154	0.150

Table 11: ^{3}He cell: Moss wall and window thickness summary.

Points	Incident Angle [°]	Fitting Results [mm]	UVA Results [mm]
A	8.5	1.607	1.61
B	10.5	1.606	1.58
C	11	1.625	1.64
D	11	1.601	1.59
E	8.5	1.698	1.68
F	7.5	1.678	1.68
G	10	1.633	1.62
H	6.5	1.651	1.66
I	6	1.596	1.58
J	6.5	1.679	1.67
W1	14	0.134	0.131
W2	16	0.149	0.150

3.6.4 BigBite Trigger Electronics Checkout

For the E05-102 experiment a new coincidence trigger was designed in order to record coincidence events from the $(e, e'p)$ and $(e, e'd)$ reactions. In addition, a re-timing circuit was used. With this circuit we precisely specified how relative time measuring should work already in hardware (Fig. 48). It was designed such, that the time of each signal was always measured with respect to the proton or deuteron in the BigBite spectrometer. This means that a raw coincidence peak should directly be seen from the time distribution of the electron trigger, without any additional analysis.

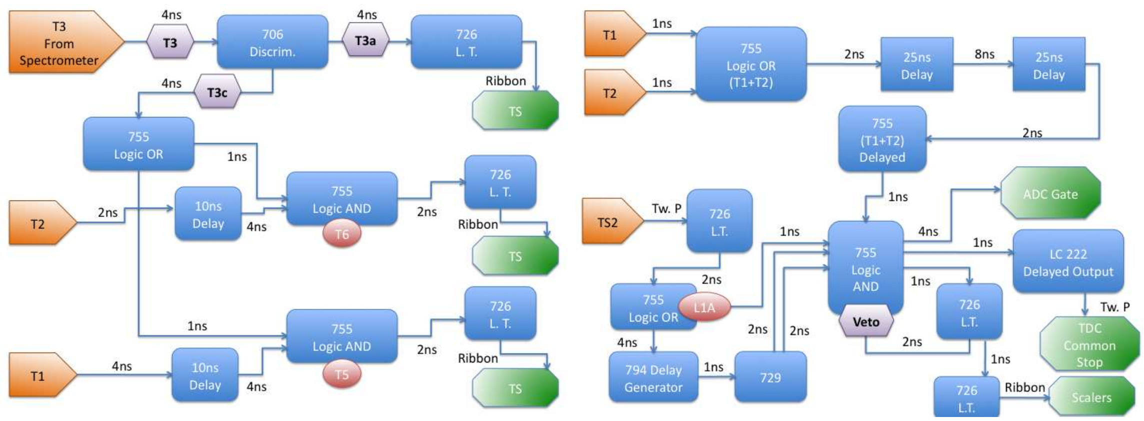

Figure 48: BB-re-timing scheme: Trigger T1 and T2 from BigBite and T3 from HRS-L are first led to Trigger supervisor (TS) which decides whenever to accept a given event or not. Afterwards the signal from (TS) goes to the BigBite re-timing where it is properly manipulated so that the final output signal which triggers the ADC and TDC modules is always timed off BigBite triggers.

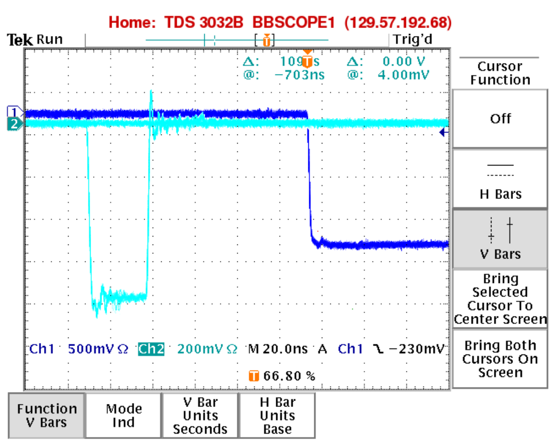

Figure 49: Plot shows the time difference between T1 and BigBite re-timing on the input to the scalers. The time difference is approximately 110 ns. According to the left scheme in Fig. 48 the time difference should be: $1+8++25+8+25+2+8+1+8+1+5+1+3 = 103$ ns. Since the error of our readout from the scope plot is at least 5 ns this is a good match. Note that the position of the BigBite re-timing signal does not move relative to the T1: the circuit is designed such that the BigBite re-timing pulse is always timed relative to T1.

Before and during the experiment we made a series of measurements with the simulated signals and the oscilloscope which were used to check if the triggers work properly. For these trigger tests we used artificial signals that simulated real physical processes. For that purpose we used two Event Dead Time Monitor modules (EDTM), one situated in the HRS-L, and configured as master,and the other in the BigBite weldment, configured as a slave. The master EDTM sends out simulated pulses to the HRS-L electronics and one pulse to the slave-EDTM. The slave module was programmed such that the simulated signals arrive to the BigBite electronics with the delay that corresponds to a delay, that corresponds to a real physical event. In order to do that, we had to consider the difference in flight paths and flight times of the proton

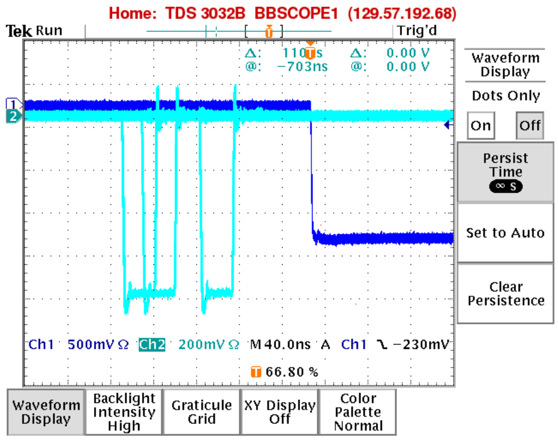

Figure 50: Time difference between the BigBite re-timing signal (blue) and the T3 trigger (cyan) on the input to the scalers. Since the re-timing is always relative to T1, the time difference between T3 and BigBite re-timing is not constant. Consequently we get different pulses corresponding to this time-difference variation.

and electron, as well as the length of the cables going from the HRS-L to the BigBite weldment. Figures 49 and 50 show two examples of scope plots that we got as results of this calibrating simulation.

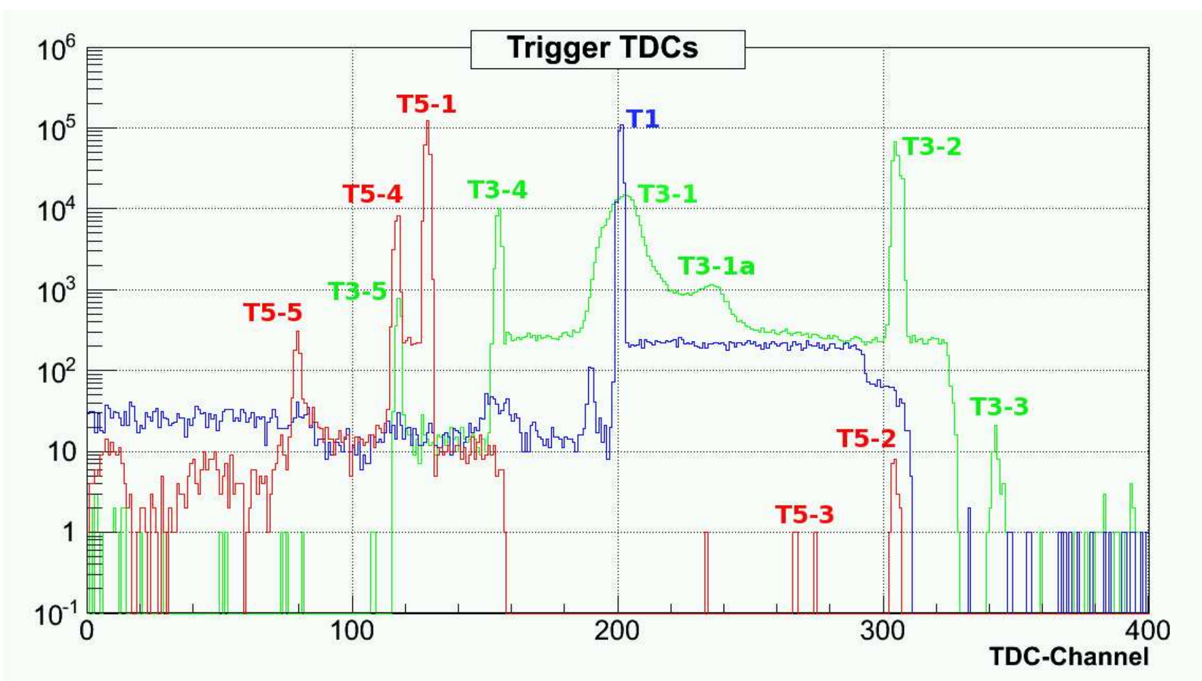

Figure 51: TDC spectra of raw T1, T3 and T5 triggers relative to the BigBite re-timing pulse.

Another set of tests was made during the $^3\vec{\mathrm{He}}(\vec{e}, e'd)$ production running using the TDC and scaler data from all triggers. Using this information we were able to check if the real triggers work the way we tried to design them. Plot 51 shows the TDC spectra of T1, T3 and T5 triggers relative to the BigBite re-timing pulse for the elastic deuteron run. Looking at the plot we realize, that the trigger response is far more complicated than we have anticipated. Peak $T3 - 1$ corresponds to the electron single events, where there was no detected proton/deuteron in BigBite. In this case, the output pulse from TS was timed off T3 and therefore this peak is sharp. Peaks $T3 - 1$ and $T3 - 1A$ correspond to coincidence peaks. We believe that the T3-1 peak represents coincidence protons from the $^3\vec{\mathrm{He}}(\vec{e}, e'p)pn$ and $^3\vec{\mathrm{He}}(\vec{e}, e'p)d$ processes, while the smaller peak T3-1A on its right represents elastic deuterons. We can see that the time difference between peaks T3-1 and T3-3 is approximately 53 ns. This difference agrees with the results from the scope test. We do not know the origin of the T3-3 peak, but we can see that these events happen very rarely and can therefore be neglected.

In addition, two sharp peaks T3-4 and T3-5 on the left of the coincidence peaks can be observed. These two peaks cause two additional peaks in the T5 coincidence trigger spectrum. Because the peaks are sharp, we can assume that in these two cases the BigBite re-timing pulse was timed off T3 instead off T1. One can see that by making a cut on these two peaks one generates a plateau at the right of the T1 peak, corresponding to random coincidences. From the detailed analysis of the scope plots we determined, that because of the different lengths of the pulses and delays set in the electronics, it can in some random cases happen that the BigBite re-timing pulse is timed off T3 although there was a T1 present.

Apart from the rare and specific timing occurrences described above, which generate additional peaks in the timing spectra that were not anticipated, the BigBite trigger appears to work properly and in accordance with the original design.

3.6.5 HRS Optics Calibration

The goal of HRS optics calibration is to connect focal-plane variables with target-coordinate variables. This work is practically performed by expanding focal-plane variables in polynomials and the coefficients of these polynomials are recorded as matrix elements in HRS databases.[4]

People always try to avoid over-optimization, during which target-coordinate variables are calculated correctly at and only at selected kinematics regions. Over-optimization usually happens when people use excessive high-order terms and when they can not test their matrices at different kinematics settings. In order to avoid over-optimization, a universal matrix for all kinematics settings was sought for this experiment. Since lower-order matrix terms would lead to better universality of optimization, matrix elements in this optimization were tried to be lower ordered than a simple database used back in 1989. This simple matrix was a classic and it achieved great success for its own use.

θ and ϕ parts of the matrix were optimized by HRS sieve run data. The target y part of the matrix was optimized by carbon foil runs. The software that was used was Nilanga Liyanage and Jin Huang's optimization code. In the software sample events were selected from typical optimization regions and the optimization code tried to fit a polynomial that minimizes the RMS of the difference between reconstructed and real data.

The momentum optimization was a different procedure. At the time of optimization the momentum part of the matrices already performed reasonably before optimization within 4 MeV error range. At this error level the reconstructed momentum peaks should have a good shape, all that needed to be done was to fine tune zeroth and first order matrix terms by hand. A modified momentum, *dp_kin*, was calibrated from elastic electron carbon scattering at different carbon excited states. The virtue of *dp_kin* is that it is a quantity independent of the electron scattering angle.

One last step is to check the momentum calibration and to fine tune the ϕ part of the matrix. Since there was not a perfect sieve position survey, one would expect an error of 2 mrad in sieve positioning. This could be rectified from hydrogen elastic-scattering data, by comparing the reconstructed scattering momenta with corresponding theoretical values. It is known that the offsets of momentum and ϕ reconstruction are closely correlated by a simple scattering formula. With the confidence of momentum reconstruction, one could tune the offset term of the ϕ matrix by hand in order to align the reconstructed and theoretical values.

After optimization this universal matrix was tested at different kinematic settings, which have beam energies ranging from 1 up to 3 GeV, LHRS angle ranging from 12.5^o to 17^o, RHRS angle ranging from 16^o to 18^o. Plots of RHRS are not shown in this report but they are very similar to those of LHRS.
Figure 52 shows the left arm vertex reconstruction at 17^o when the beam energy is 1.245 GeV. Figure 53

shows the left arm momentum dp versus vertex reconstruction for the same run. It is expected that vertex reconstruction is independent of the momentum dp reconstruction.

Figure 54 shows the LHRS sieve reconstruction from a typical carbon foil with a 2.4 GeV beam at a 12.5^o angle. The outcome of the momentum reconstruction and the ϕ tuning is shown in Fig. 55. In this figure the black lines are the theoretical hydrogen elastic-scattering momenta at different HRS momentum settings, while the colored peaks are the reconstructed momenta by matrix.

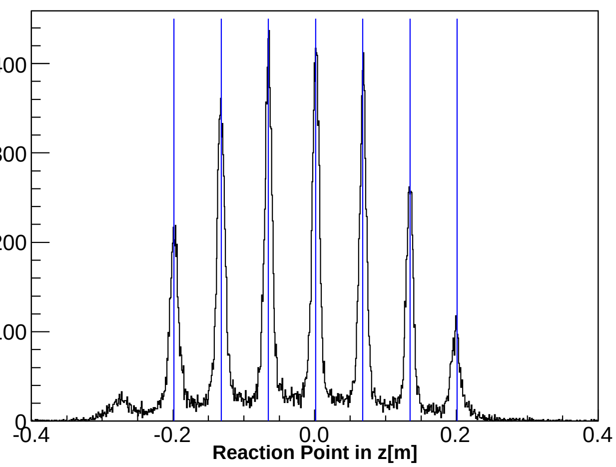

Figure 52: Reaction point reconstructed from the seven foil optics target. The small peak to the left of the seventh foil is the BeO alignment target.

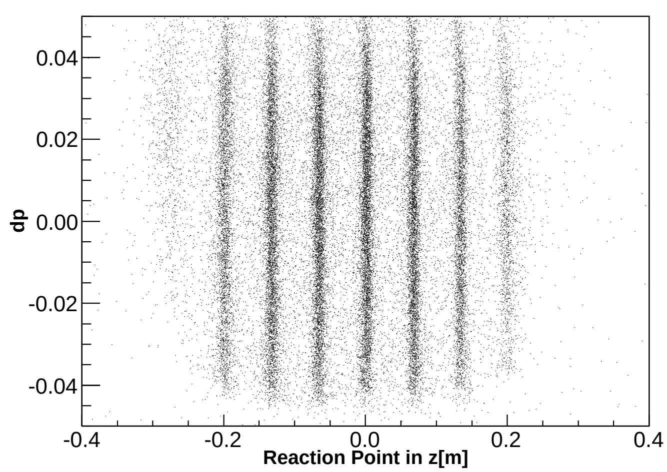

Figure 53: Momentum reconstruction vs. the reaction point for a first pass run.

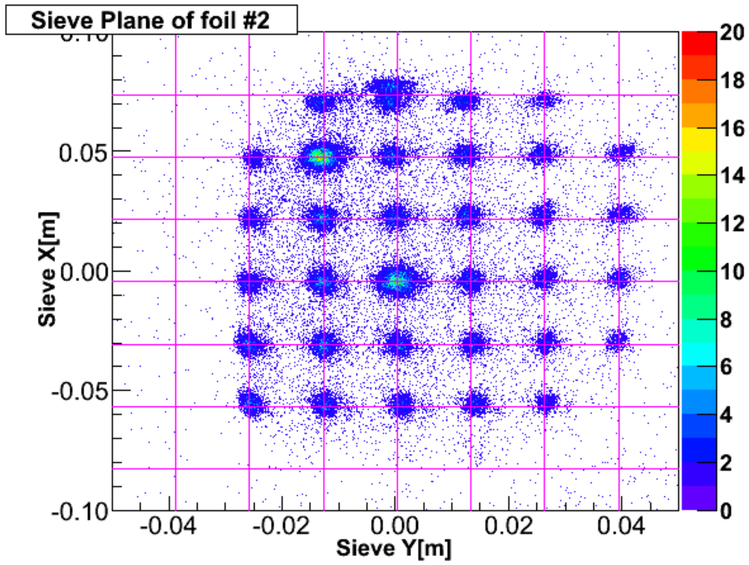

Figure 54: LHRS reconstructed sieve pattern.

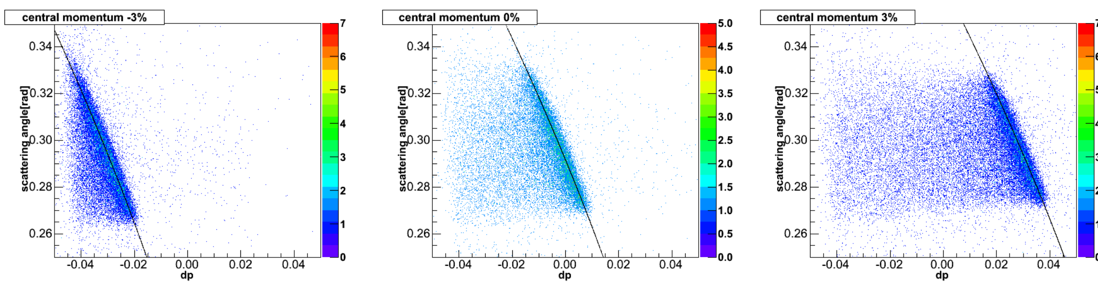

Figure 55: Momentum reconstruction from hydrogen elastic data for three different momentum settings.

References

[1] T. Averett, J.-P. Chen, and X. Jiang, spokespersons of E05-015: Measurement of the Target Single-Spin Asymmetry in Quasi-Elastic ^{3}He↑(e,e').

[2] S. Gilad, D.W. Higinbotham, W. Korsch, B.E. Norum, S. Širca, spokespersons of E05-102: Measurement of the A_x and A_z asymmetries in the polarized quasi-elastic ^{3}He(e,e'd) reaction.

[3] T. Averett, D.W. Higinbotham and V.A. Sulkosky, spokespersons of E08-005: Measurements of the Target Single-Spin Asymmetry A_y in the quasi-elastic ^{3}He↑(e,e'n) reaction.

[4] J. Alcorn *et al.*, Nucl. Instrum. Meth. **A522**, 294 (2004).

[5] E. Hecht, *Optics* (Addison-Wesley, San Francisco, 2002).

3.7 E06-010

Measurement of Single Target-Spin Asymmetry in Semi-Inclusive Pion Electroproduction on a Transversely Polarized ^{3}He Target

J.-P. Chen, E. Cisbani, H. Gao, X. Jiang, J.-C. Peng co-spokespersons,
and
the Hall A Collaboration.

contributed by K. Allada, E. Cisbani, C. Dutta, J. Huang, X. Jiang, X. Qian, V. Sulkosky and Y. Wang.

3.7.1 Physics goals and a summary of the experiment.

Experiment E06-010 was merged from two experiments: E06-010 and E06-011, which were approved at PAC29 in 2006. The experiment was previously approved as experiment E03-004 in 2003 at PAC23. The experiment collected data in Hall A from Oct. 24, 2008 to Feb. 5, 2009, with 23 days of scheduled machine down time in Dec. 2008 and Jan. 2009.

The goal of this experiment is to provide the first data of neutron target single-spin asymmetry (SSA) A_{UT}^{nh} in the semi-inclusive deep inelastic $(e, e'h)$ reaction $(h = \pi^+, \pi^-, K^+, K^-)$. The asymmetries will be separated into Collins-type and Sivers-type through angular dependence. Earlier in time, the HERMES experiment [1, 2] reported a rather large target SSA on a transversely polarized proton target, at the several percent level, for both Sivers and Collins type asymmetries. However, the COMPASS experiment [3] reported close to zero SSA on a deuteron target for both Collins and Sivers. Furthermore, in mid-2007, COMPASS reported preliminary SSA on a proton target [4]; while the Collins-type asymmetry is consistent with HERMES within large statistical uncertainties, the Sivers-type asymmetry was reported to be close to zero. Given the present status of the existing data, independent SSA data for the neutron are urgently needed, which is more sensitive to d-quark (assuming isospin symmetry from the proton case) contributions.

3.7.2 Experiment layout and preparations

The experiment used the BigBite spectrometer, used earlier during the G_E^n experiment [5], as the electron arm (left panel of Fig. 56) in coincidence with the left high-resolution spectrometer (L-HRS) as the hadron arm. BigBite was placed at an angle of 30° with respect to the right-side of the beam line with the magnetic field set to 1.2 T. The drift distance from the target to the BigBite dipole magnet was 1.5 m. The BigBite electron detector package consisted of two front wire chambers, followed by a threshold gas Cherenkov detector, a third wire chamber, a layer of lead-glass preshower blocks, timing scintillators and an array of lead-glass shower blocks.

An optics test run with BigBite at 1.5 m drift distance was carried out at the end of the G_E^n experiment in mid-2005 to confirm the optics properties ahead of the time. Based on the operation experience during the G_E^n run, a decision was made to use the LeCroy-1877 Time-to-Digital Converters (TDCs) and FASTBUS crates for chamber read-out. The middle chamber was upgraded by UVa to be a full chamber with six wire-planes. The shower blocks were also baked and refurbished to optimize the performance. The BigBite detector package was set up in the test lab, and extensive cosmic ray tests were carried out for over two years. In addition, extensive beam tests of major elements, except for the gas Cherenkov, were carried out during the threshold-π^0 [6] and the low-Q^2 G_E^p [7] experiments in early 2008.

The L-HRS, located at 16° with respect to the left-side of the beam line and set to a central momentum of 2.35 GeV/c, was used to detect hadrons in coincidence with the electrons. The L-HRS's polarity was changed several times so that data of both positively and negatively charged hadrons were collected. The L-HRS detector package consisted of two vertical drift chambers (VDCs), scintillator S1 plane, an aerogel detector A1, a short-version of the gas Cherenkov, a refurbished RICH detector, scintillator S2m plane, followed by two layers of lead-glass detectors, which are commonly referred to as the "pion rejector".

The Hall A polarized ^{3}He target system was modified to provide vertical and transverse in-plane target polarization. Most importantly for this experiment, a capability of spin reversal at 20 minute/flip was implemented using RF-flip, while the target holding field was kept unchanged.

3.7.3 Commissioning of the experiment

First and second pass beam energies were used during the commissioning stage of the experiment prior to the fifth-pass 5.9 GeV production running. The calibration runs included:

- Carbon foil runs for vertex calibration.
- Sieve slit (1.5" thick lead) runs with carbon foil targets for angle reconstruction.
- Reference cell runs with hydrogen gas for H(e, e') elastic reaction to calibrate the gains of the shower blocks.
- Reference cell runs for H$(e, e'p)$ elastic reaction to set up the coincidence timing.
- Polarized ^{3}He elastic and Δ-production runs to check "well-known" asymmetries.

3.7.4 BigBite Spectrometer

The detector package consists of three sets of multi-wire drift chambers (MWDC) for precise kinematics reconstruction, a scintillator plane for timing information, and a lead-glass calorimeter consisting of a preshower and shower for particle identification (PID) and trigger. The electrons are identified by cutting on the 2-D distribution of the preshower energy vs. E/p (total energy over reconstructed momentum). A typical PID plot is shown in the right panel of Fig. 56. A GEANT3 model was developed to help understand the backgrounds and contamination to the electron identification.

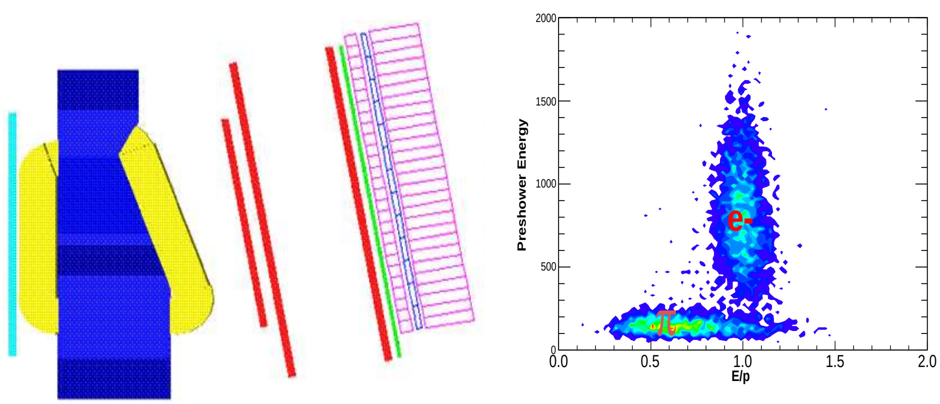

Figure 56: Left: BigBite spectrometer schematic for E06-010. Right: Preshower energy vs. E/p with polarized ^{3}He production data with 5.892 GeV, 12 μA incident beam.

Multi-Wire Drift Chambers

This experiment requires precise knowledge of the momentum of the scattered electron in the range of 0.6 - 2.5 GeV/c. For this purpose, three MWDCs were used to reconstruct the scattered particle's track with new tracking software (developed by Ole Hansen) based on pattern matching. The on-line tracking efficiency was found to be higher than 85%. A spatial resolution of 180 μm was achieved with an off-line calibration of MWDC. The optics model for both positive and negative charged particle was developed by X. Qian. The interaction vertex was calibrated with carbon foils (Fig. 57 left panel), which were mounted along the 40 cm target length. The average vertex resolution through the entire momentum coverage is about 0.72 cm. A custom designed 1.5" thick sieve plate (Fig. 57 middle/right panel) made of lead was used to calibrate the angles. An angular resolution better than 10 mrad was achieved. The momentum reconstruction (Fig. 58) was calibrated with hydrogen elastic data at two incident beam energies 1.231 and 2.306 GeV. The final momentum resolution is about 1%.

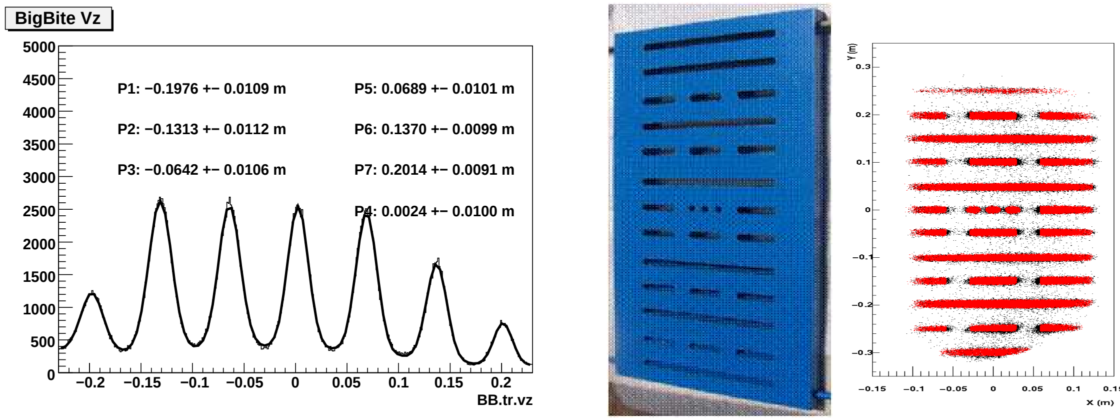

Figure 57: Left: BigBite vertex reconstruction of seven carbon foils; Middle: BigBite sieve; Right: Reconstructed BigBite sieve pattern.

Scintillator Plane

A scintillator plane was placed between the preshower and shower detectors and was primarily used for measuring the time of the hits in the BigBite spectrometer; when combined with the S2m scintillator timing in the left HRS, the coincidence time of the event can be determined. The coincidence time-of-flight in the left HRS is used as PID to identify hadrons. The BigBite scintillators were calibrated by J. Huang, and a timing resolution of about 250 ps was achieved. See Section 3.7.6 for more details on the timing calibration.

Preshower and Shower

Calorimeter detectors made of lead glass were used both for particle identification and the electron trigger in the BigBite spectrometer. Dimensions of the preshower/shower blocks are 8.5 cm × 37 cm × 8.5 cm. The preshower consists of two columns with 27 blocks in each column, while the shower consists of seven columns with 27 blocks in each column. The calorimeter was calibrated by K. Allada with both 1.231 and 2.306 GeV incident beam energies using the hydrogen elastic reaction with reconstructed electron momentum. An energy resolution of about 8% was achieved (Fig. 58).

3.7.5 Trigger and Data Acquisition

A coincidence trigger was set up between the BigBite spectrometer and L-HRS by K. Allada and V. Sulkosky. Overlapping layers of the lead-glass calorimeter were used for the BigBite electron trigger; whereas, the S1 and S2m scintillators provided the trigger in the L-HRS. A re-timing circuit was implemented in both the spectrometers. The coincidence window was 140 ns wide, and the timing for the coincidence trigger (T5) was provided by the BigBite singles trigger (T1). Three different triggers were constructed for the BigBite package: a low threshold on the total-sum of lead-glass layers as a primary trigger (T1), a high threshold trigger T6 and an overlap between the lead glass and BigBite gas Cerenkov as T2. The later two triggers, T2 and T6, were used by the parasitic measurements. The BigBite scintillators, which provide timing information for the coincidence time-of-flight calculation, were read out using JLab custom-made F1 TDCs in high resolution mode (60 ps), and the wire chambers were read out using FASTBUS 1877 TDC modules. In the L-HRS, the scintillators were read out using a FASTBUS 1875 TDC module, which has a resolution of 50 ps. For all other detectors, low resolution (0.5 ns) 1877 modules were used.

Scaler Setup

The scaler set-up was designed by taking into consideration the needs of the parasitic measurements and to provide enough cross-checks on important signals. We used one ungated scaler module and four gated scaler modules for target-spin and beam helicity combinations: ++, +- , -+ and --. We used two identical

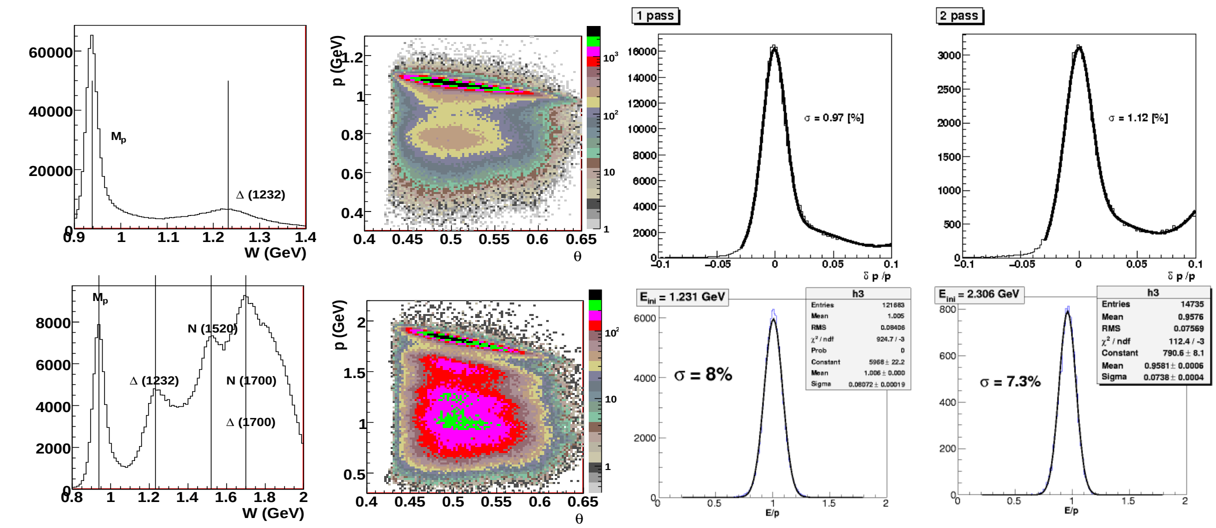

Figure 58: BigBite optics reconstruction (left four panels): The top (bottom) left panel shows the reconstructed missing mass with 1.231 (2.306) GeV incident beam energy. The top (bottom) right panel shows the 2-D plot of reconstructed momentum vs reconstructed polar angle with 1.231 (2.306) GeV. BigBite momentum/energy reconstruction (right four panels): The top left (right) panel shows the reconstructed momentum resolution with 1.231 (2.306) GeV. The bottom left (right) panel shows the calibrated energy over reconstructed momentum with 1.231 (2.306) GeV.

copies of the gated and ungated scalers in the two spectrometers for cross-checking purposes. Scalers were read out using SIS 38xx modules in 3800 mode. The scaler channels were read out every 100 events as an "event-scaler" and every two seconds as event type 140. A set of important signals such as beam current and triggers were also read out for every event. An online scaler cross-checking software was implemented to check scalers on a run-by-run basis.

Major Problems/Issues

The experiment encountered a few problems related to the data acquisition. Here we list the major ones:

1. During January 2009, the level-1 accept signal on the L-HRS was found to be intermittently double pulsing due to a flaky cable. This issue affected about 56 runs. Less than 10% of the events in each of these runs were affected. The problem was identified and fixed by replacing the cable. The affected events were later identified in the software by doing various studies and cut away in the analysis.

2. A gain drop was observed on the BigBite lead-glass detector due to radiation damage, especially on the preshower. There was about a 15% drop on the preshower and less than 5% on the shower. Since the threshold on the primary trigger T1 was set much lower ($\sim$ 300 MeV) than the energy of the scattered electron in which we are interested ($>$ 600 MeV), the effect was small. However, this issue severely affected the higher threshold trigger T6. A position-dependent correction was later done in the software to take care of this degradation.

3.7.6 Coincidence Time Calibration

For experiment E06-010, the target single-spin asymmetry was measured by detecting the hadrons in the L-HRS, which are in coincidence with the electrons detected in the BigBite spectrometer. A coincidence time (CT) between this two spectrometers is defined as the time difference between when two particles are created in the reaction. Therefore, a perfect system should show a CT with a sharp peak at 0 ns. In case of multiple final states, a CT is calculated with respect to a specific species of particle in each arm. The coincidence of different species of particle would appear at different locations in a CT spectrum.

The major goal of the CT calibration for E06-010 is zeroing offsets of $(e, e'h)$ CT peaks as well as minimizing their widths. This calibration brings about the following benefits:

- Reducing random coincidence background: besides true $(e, e'h)$ events, a percentage of the final random coincidence contamination is proportional to the width of the CT peaks.
- Helping particle identification (PID) on the hadron arm: assuming electron events are selected with the Bigbite spectrometer, the CT peak location will be related to the time-of-flight (TOF) of hadrons detected by the L-HRS. Therefore, the kaon peak will be ~ 1.8 ns apart from that of the pion, and the proton-pion peak separation is ~ 6 ns. This separation is important to obtain a clean kaon data sample.

In the calculation, the CT can be separated into three parts:

$$\mathrm{CT} = \mathrm{RF\ Time}_{\mathrm{LHRS}} - \mathrm{RF\ Time}_{\mathrm{Bigbite}} - \mathrm{Trigger\ Time\ Difference}\,, \tag{4}$$

where Trigger Time Difference is the time difference between two single arm triggers, and RF $\mathrm{Time}_{\mathrm{Spectrometer}}$ is defined as the amount of time between a vertex reaction and single arm trigger. RF $\mathrm{Time}_{\mathrm{Spectrometer}}$ includes contributions from

- Time-of-Flight: amount of time for a particle to travel from the reaction point to the timing detector.
- Response time of timing detector: including detector response time, cable delay and electronic process time.
- Time difference between timing detector signal and trigger signal. These values are recorded using high resolution (60.2 ps on Bigbite and 50.0 ps on L-HRS) TDCs.

The RF $\mathrm{Time}_{\mathrm{Spectrometer}}$ is named after its calibration procedures: during E06-010, the beam radio frequency (RF) signal, which characterizes the beam bunch time, is recorded in TDCs (noted as t_{RF}), relative to the single-arm trigger signal. Therefore, when the spectrometer's angle is small, RF $\mathrm{Time}_{\mathrm{Spectrometer}} - t_{\mathrm{RF}}$ (also called RF or RF Structure for short in later section) would appear as sharp peaks every 2 ns (beam bunch spacing). By minimizing the width of these peaks, RF $\mathrm{Time}_{\mathrm{Spectrometer}}$ is calibrated separately for each arm .

In the following subsections, a summary of the calibration of RF $\mathrm{Time}_{\mathrm{Spectrometer}}$ for both spectrometers and the final CT are presented.

L-HRS Single Arm Timing Calibration

In the L-HRS, the time reference was defined by the S2m scintillators. The 2 ns RF structure of the beam bunch was used as a reference for the analysis. In order to achieve a resolution at a level of a few hundred picoseconds in the RF structure, various factors have to be corrected and implemented, which include the pathlength corrections, scintillator time offset corrections and timewalk corrections. Once the pathlength corrections were done for a single paddle, the timing structure could be seen for that particular paddle by plotting a quantity, RF, defined as:

$$\mathrm{RF} = t_{\mathrm{RF}} - \frac{(t_{\mathrm{Left}} + t_{\mathrm{Right}})}{2} + \frac{\mathrm{Pathlength}}{c}\,, \tag{5}$$

where t_{Left} (t_{Right}) is the scintillator time from the left-side (right-side) of the paddle, and c is the speed of light. Then this procedure was extended to all 16 paddles of the S2m scintillator to obtain the resolution for the whole plane. In order to do that, time-walk corrections were applied to each paddle for pions, and then all paddles were aligned. The time-walk correction for each paddle was evaluated by looking at the dependence of the quantity RF as a function of the average of the left and right ADCs as shown in Fig. 59. Figure 60 shows the time-walk effect corrected for that particular paddle.

Once the time-walk corrections were applied to all paddles, a final alignment of the offsets was performed. Even though the time-walk effect was considerably small, 20 to 30 ps, the resolution could still be improved,

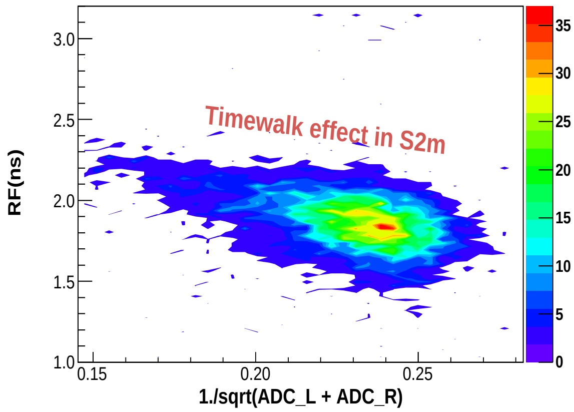

Figure 59: Time-walk effect for S2m.

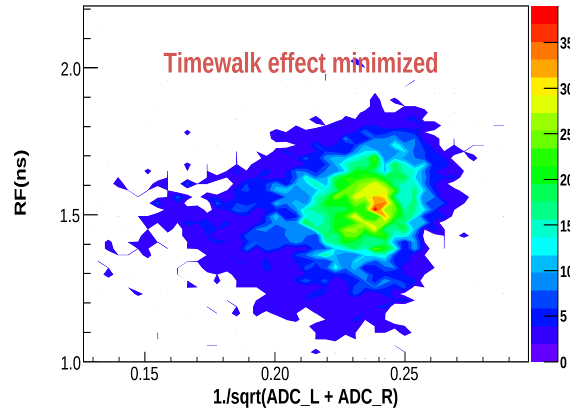

Figure 60: Corrected time-walk effect for S2m.

and the tails of the spectrum were also reduced to some extent. Finally, when all these corrections were applied, the timing resolution from the L-HRS side was improved to ∼140 ps for pions and ∼135 ps for electrons, as shown in Figs. 61 and 62, respectively.

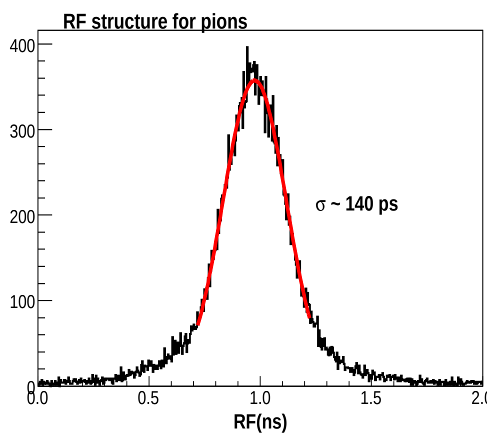

Figure 61: RF structure for pions.

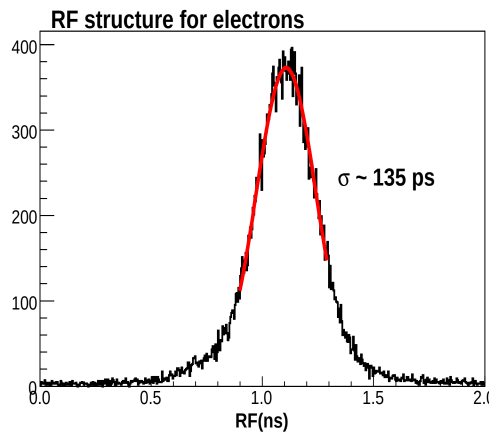

Figure 62: RF structure for electrons.

Bigbite Single Arm Timing Calibration

RF Time$_{\mathrm{Bigbite}}$ is simpler due to its shorter pathlength and similarity of speed of particles detected. Two series of RF times are generated for electron and photon candidates.

The timing detector inside the Bigbite spectrometer is a 13-bar scintillator plane inserted between the preshower and shower lead-glass detectors. A PMT is mounted on each end of the scintillator bars, whose signals are recorded by measuring both timing and amplitude information. The timing response of a single bar is $\sim$ 230 ps. For an electron event, the primary electron, as well as secondary particles from an electromagnetic shower inside the preshower detector, will fire at least one of the scintillator bars and probably one of the neighboring bars.

The calibration procedure is separated into the following major steps:

1. Scintillator bar offset and time-walk effect correction. First, events firing only two neighboring scintillator bars are selected. The timing difference between these two bars are optimized toward 0 by

applying a time offsets for each PMT as well as a time-walk correction. The time-walk effect on each PMT was found to be similar so that a single formula, Eq. 6, is good enough to apply on all PMTs:

$$\Delta t_{\text{time walk}} = -17.9(\text{ADC} - \text{pedestal})^{-0.140}\text{ns}\,. \tag{6}$$

2. Pathlength calibration: A simple linear correlation is used to correct pathlength differences: (Eq. 7)

$$\Delta L_{\text{time-walk}}/c = 1.4 * \theta_{\text{MWDC}}\,, \tag{7}$$

where θ_{MWDC} is the tangent of the vertical track angle measured by the MWDC, which is also highly correlated with the vertical hit position on the chamber. Up to second order, further polynomial terms on additional tracking parameters were found not to bring a notable improvement to this correction. Instead, a second iteration of bar-by-bar offset alignment is performed to take out leading non-linear vertical dependent corrections.

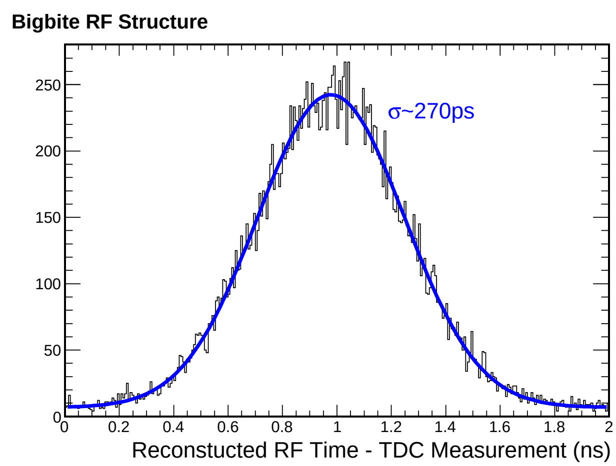

Figure 63: RF $\text{Time}_{\text{Bigbite}} - t_{\text{RF}}$ for single arm electron events.

The final resolution of the RF time for the Bigbite spectrometer was calibrated to $\sim$ 270 ps (1σ), as shown in Fig. 63. Further improvements are limited by the intrinsic resolution of the scintillator and the open geometry of the Bigbite magnet.

In a parallel study, the trigger detector (total shower detector) timing was also calibrated to achieve a better tracking performance in the drift chambers. The FWHM uncertainty of the trigger was reduced from $\sim$ 8 ns down to $\sim$ 4 ns, which is a $\sim$ 10% improvement on the tracking quality flag, χ^2/n_{DOF}.

Two Arm Coincidence Time Calibration

The last term in Eq. 4 is measured by a TDC with a resolution of 60.2 ps. A typical CT spectrum with the L-HRS detecting positive hadrons is shown in Fig. 64. Accounting for all terms, the total CT reached a resolution of $\sim$ 340 ps (1σ) for $(e, e'\pi)$ reaction and $\sim$ 400 ps (1σ) for $(e, \gamma\pi)$ events.

- Compared to the DAQ coincidence window of $\sim$ 200 ns, a ± 1 ns (3σ) cut will suppress random coincidence events by an factor of 100.

- By cutting on the kaon CT with a window of ± 1 ns, pion rejection can reach $> 25:1$. Most of the pion leakage comes from non-Gaussian tails in the timing peaks. Further improvement is expected to be achievable by applying a two-dimensional CT vs A1 (Aerogel Cherenkov Detector) graphical cut and tighter timing quality cuts.

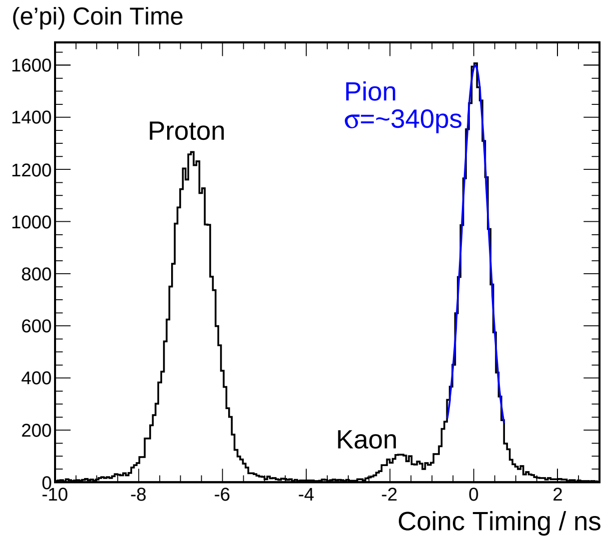

Figure 64: $(e, e'\pi)$ CT spectrum for L-HRS at positive polarity.

3.7.7 HRS Optics Calibration

General Approach

Following the general procedure of reference [8], the goal of this study is to calibrate the following HRS optics properties:

- y_{tg} and z_{react} : for vertex coincidence with Bigbite spectrometer, suppressing random coincidence background
- θ_{tg} and ϕ_{tg} : for angular information of Semi-inclusive Deep Inelastic Scattering (SIDIS) hadrons and angular separation of asymmetries
- δ_{tg} : for better background rejection on elastic studies, including ^{3}He elastic asymmetry and pressure curve study.

The available data include an optics target (7 carbon foils that cover the total target cell length of 40 cm) with sieve-slit plate on/off L-HRS and elastic reference cell runs of ^{3}He, H_2 and N_2.

A new optimization routine is established for the E06-010 L-HRS optics calibration. The website is under construction at [9]. This new code features

- To ensure that the optimization code performs the exact same calculation as the analyzer, the calculation routine is converted from the optics code `THaVDC` [10]
- Minimization routine is based on the more advanced package `MINUIT2` [11]
- Automatically visualize results after optimization
- Multiple self-consistency checks.

Vertex, Angular and Momentum Calibration

The calibration process is divided into the following sections, each performed independently:

- The vertex is calibrated according to the pre-surveyed carbon foil locations. As shown in Fig. 65 all foil peaks are aligned to their actual positions. The average z_{react} resolution is 6 mm with the spectrometer at 16° for a 40 cm long target. The L-HRS and Bigbite vertices are consistent to the level of 1 cm (1σ) for coincidence events.

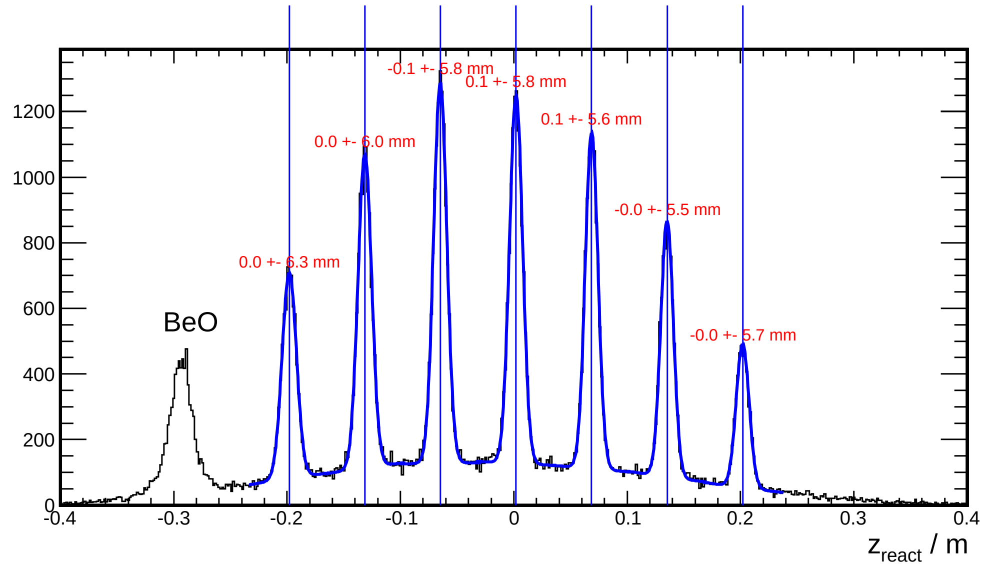

Figure 65: Reconstructed z_{react}: Each carbon peak is fitted and compared to its expected location. The left-most peak is the beryllium oxide foil.

- With carbon foil runs and the sieve-slit inserted, each good event corresponds to a specific carbon foil and one of the holes in the sieve-slit. For this study, a near white spectrum run was selected. By referencing to survey information [12], the actual angle of the vertex trajectory is known. The out-of-plane (θ_{tg}) and in-plane (ϕ_{tg}) angles are optimized by minimizing the difference between the calculated angle and the actual one. The final reconstructed sieve-slit is shown in Fig. 66
- A set of similar runs, as those used for the angular calibration, is also used for the momentum calibration. The full momentum range of the spectrometer is covered by moving the carbon elastic peak across the focal plane in a δ-scan: $p_0 = 0\%$, $\pm 2\%$ and $\pm 4\%$. For each momentum setting, a specific carbon ground state or excitation state is selected. An optimization is performed with all momentum settings at the same time. The final results are shown in Fig. 67 with an achieved resolution better than 5×10^{-4}.

Extended Target Correction and Raster Correction

The optics matrix, which is calibrated as described earlier, does not include all information for the optics reconstruction, rather than corresponding to the case with the spectrometer angle at 90° and the beam propagating along the hall center line. However, for the HRS whose acceptance is small, a set of simple corrections, so called Extended Target Correction, can be applied. It has been shown [13] that the leading-order correction is linearly correlated with the vertical beam position. Therefore, this correction is also called the raster correction.

The Hall A beam is rastered along two independent directions: horizontal or x and vertical or y. The raster magnet's current, which is proportional to the beam position is read out by the DAQ from an Analog-to-Digital Converter (ADC). During the analysis, the ADC signal cable was discovered to be swapped before experiment E06-010. A new raster database with the correct cable map was produced and presented to fellow Hall A collaborators [14].

3.7.8 Left HRS Performance: Gas Cherenkov and Lead Glass Counter

Experiment E06-010 requires a clear and efficient separation of pions from electrons detected in the L-HRS. Both the gas Cherenkov and lead-glass counter have been used to reject the electrons in the L-HRS. The performance of both detectors was fairly stable and reasonably efficient. The calibrations and the overall

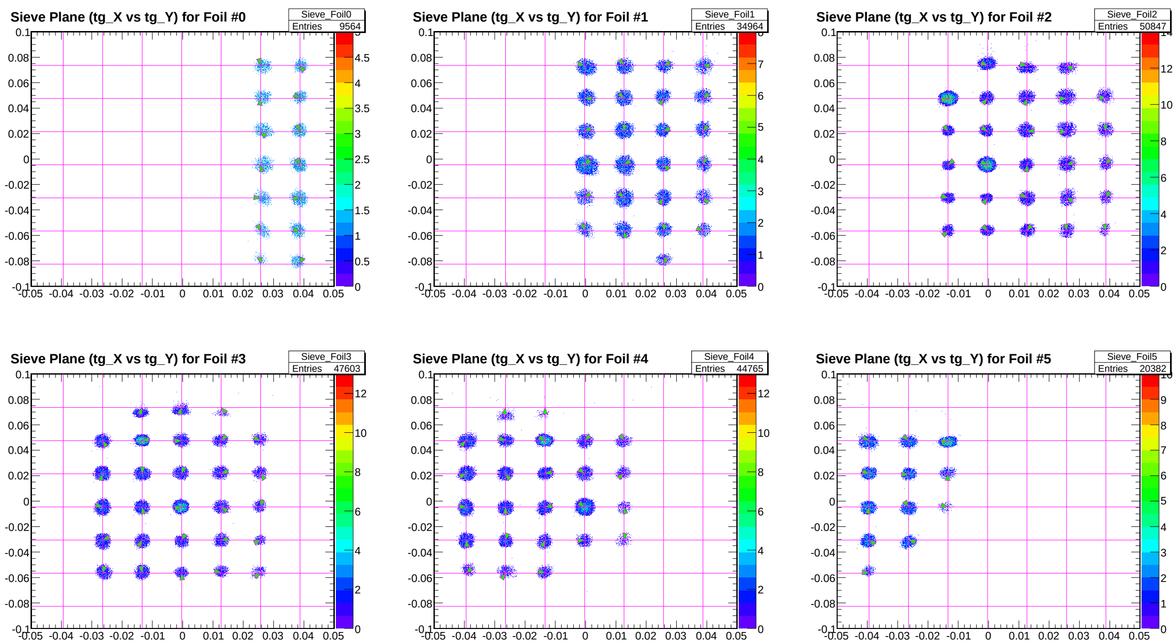

Figure 66: The reconstructed sieve-slit pattern (vertex trajectory projection at the sieve-slit plane): each plot is a single carbon foil; each crossing of pink lines represents the physical location of a sieve hole.

stability of the detectors will be discussed in the following subsections.

Gas Cherenkov

The gas Cherenkov detector in the L-HRS consists of 10 spherical mirrors in a 2×5 array layout. Each of the mirrors is coupled to a PMT where the incident light is converted to an electronic signal, which in turn is read out by an ADC. The summed signal of all the ADCs corresponds to the total light emitted by the particle. The gas Cherenkov is a powerful detector that was used for particle identification during E06-010 to separate electrons, which were the largest background in the L-HRS, from hadrons. The calibration of the gas Cherenkov involved aligning the single photoelectron peak of each ADC to channel 200 so that the sum of all 10 ADCs would be at channel 200. The purpose of the alignment was to make sure that all events that were not electrons and assumed to be mostly pions were peaked at one specific ADC channel; this allows a cleaner separation of electrons, which are at a higher ADC channel, from non-electrons. Since there were no high-voltage changes during the experiment, one calibration was adequate for the entire experiment. Before the experiment, the high voltage was set in such a way that all single photoelectron peaks for all ADCs were aligned near channel 200. After the experiment, the calibration procedure involved fitting each single photoelectron peak with a Gaussian to see if the mean was at channel 200 and then calculating the amplitude factor to perform a software gain match at 200. In other words, if the single photoelectron peak was already at 200, then the calibration would give an amplification factor of 1. The left panel of Fig. 68 shows the calibrated ADC sum for the gas Cherenkov. After the calibration, a detailed cut efficiency study was performed, and a cut on the ADC sum < 250 was used to reject electrons with 99% efficiency from pions for the final analysis.

After all calibrations were done, an extensive stability check was performed on a run-by-run basis for all production runs. The right panel of Fig. 68 shows the mean of the main electron peak in the ADC sum spectrum as a function of run number. As can be seen from the plot, the gas Cherenkov was reasonably stable during the entire period of data taking. Note that for the runs when the L-HRS was in positive polarity mode, there are few positron events; hence, those runs are not displayed in the figure.

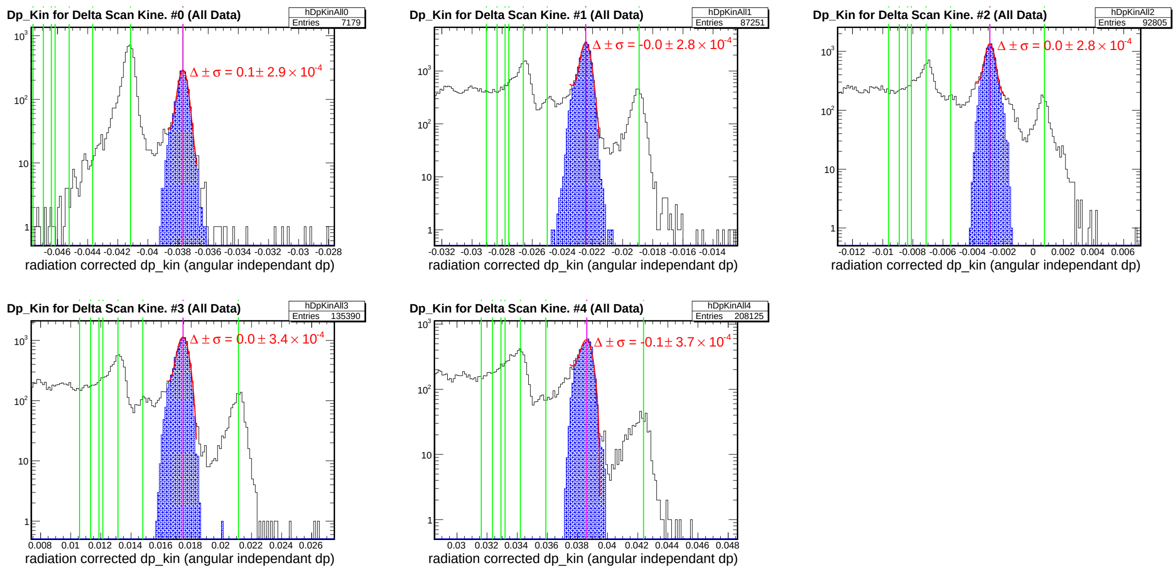

Figure 67: The reconstructed momentum of carbon elastic data for 5 momentum settings. The black curve is data, within which, the blue shaded area shows the data selected to be optimized toward the expected value (marked by magenta vertical lines). The blue areas are fitted and compared to the expectation, which is colored by red. The green lines mark out ground and other excitation states that were not optimized. These peaks also agree well with the reconstruction.

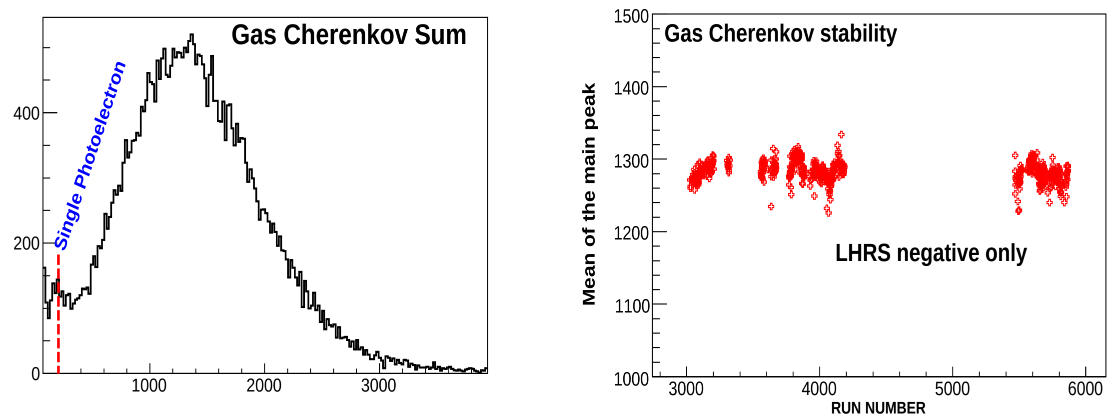

Figure 68: Left: A typical gas Cherenkov ADC sum for L-HRS negative polarity data. Right: The gas Cherenkov stability for L-HRS negative polarity data.

Lead-Glass Counter

Lead-glass counters (pion rejector) were used for additional particle identification with the gas Cherenkov to reject electrons and select pions in the L-HRS. The lead-glass counters consist of two layers, each comprising of 17 short blocks and 17 long blocks of lead glass, forming a 2×17 (transverse $\times$ dispersive) array. The energy distribution for hadrons is at low ADC channels; whereas, the energy distribution for electrons is at high ADC channels. Similar to the gas Cherenkov, there were no high-voltage changes for the lead-glass counters during the experiment; hence, one calibration was sufficient. The calibration procedure involved aligning the hadron (pion) peak to the channel 100 for each ADC, thus making a clear separation between the pion and the electron peak in the energy over momentum spectrum E/p. Figure 69 shows the calibrated lead-glass counter energy over momentum spectrum. After a detailed cut efficiency study, a cut of $E/p < 0.65$ is applied to select pions for the final analysis. Figure 70 shows the mean of the pion (left panel) and the electron (right panel) peaks, respectively, as a function of run number for all production runs for experiment E06-010. Clearly, both peaks were reasonably stable with respect to time, and the counters behaved efficiently during the experiment.

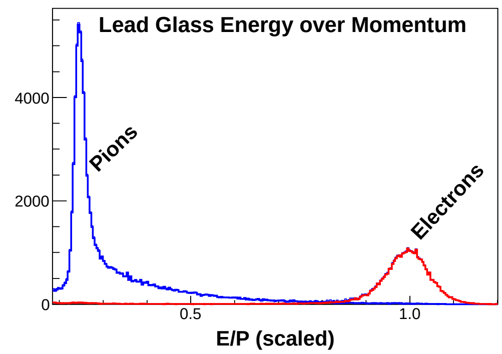

Figure 69: Lead-glass E/p spectrum after calibration.

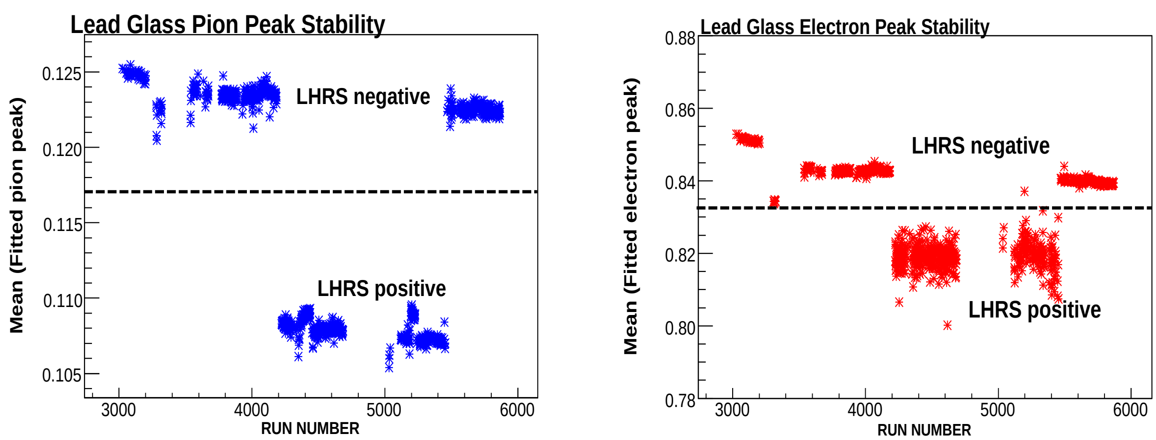

Figure 70: Lead-glass pion (left panel) and electron (right panel) stability for the entire period of data taking.

3.7.9 Performance of Aerogel Cherenkov

Experiment E06-010 required stringent particle identification to separate coincidence kaon events from a large pion and proton background. The aerogel detector was used in this experiment as a first step to separate the kaons from pions. Then, the coincidence time-of-flight (TOF) and the RICH detector (see Section 3.7.10 for details) were used to further separate kaons from pions and protons. The performance of the aerogel Cherenkov was very stable and performed with high efficiency. The calibration and overall stability of the aerogel detector will be discussed in this subsection.

When particles pass through the aerogel detector (A1), the photoelectrons generated by the aerogel are collected by the PMTs. There are a total of 24 photomultiplier tubes (PMTs) installed in A1. The index of refraction of the aerogel is 1.015. With the L-HRS momentum set at 2.35 GeV/c, only pions can trigger the detector; hence, kaons and protons are not directly detected by the Cherenkov.

Before the experiment, cosmic rays were used to select relatively good PMTs; these PMTs were installed in the A1 detector. At the start of the experiment, the single photoelectron peaks for each PMT were aligned by setting the high voltage. During the three plus months of running the experiment, only one PMT's high voltage was changed. In addition, the gain of two other PMTs degraded a bit throughout the experiment.

During the calibration, the amplitude coefficients were adjusted for all 24 PMTs to align the single photoelectron peak to channel 100. The calibration procedure was performed for six separate time periods; however, because the photoelectron peak was already aligned with high voltage adjustments, the coefficients of 21 PMTs are the same for all six periods. Only three PMTs required noticeable modifications to their coefficients. In Fig. 71, the calibrated ADC sum for the aerogel Cherenkov is shown for positive (left panel) and negative (right panel) L-HRS polarities. The sharp peak at channel 100 for positive polarity is mostly due to protons. During the experiment, the average number of photoelectrons for the A1 Cherenkov was $\sim$ 6. After calibration, the ADC sum is to used to determine the cut to separate kaons and protons from pions.

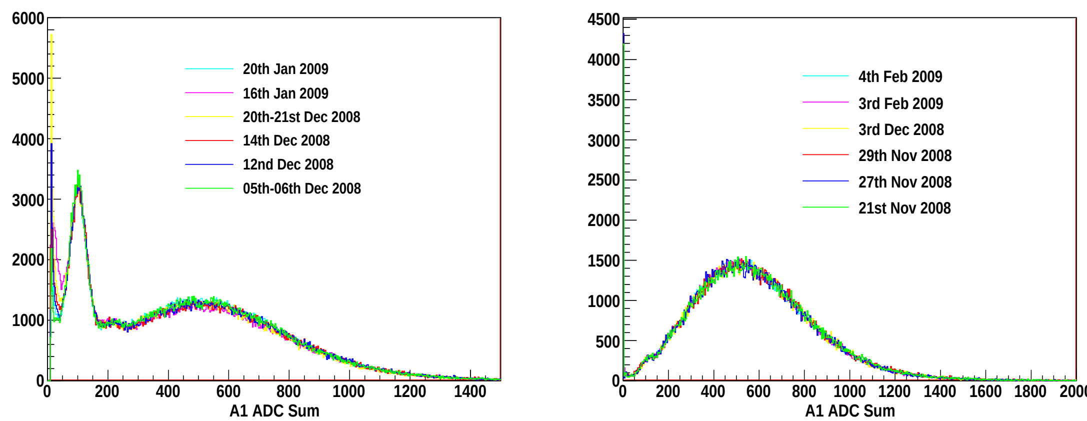

Figure 71: A1 spectrum in positive (left) and negative (right) L-HRS polarity.

With a cut on the ADC sum < 150 channels, 97% of the pions are rejected.

A run-by-run stability check was also performed for all production runs. The region between ADC channels 200 and 700 was selected and fit to obtain the mean value. Figure 72 shows that the A1 performance was reasonably stable throughout the experiment, which can be split into two time periods: L-HRS in negative polarity (run numbers: 3026 - 4212 and 5475 - 5871) and positive polarity (run numbers: 4223 - 5435). Clearly, there is a small shift in the mean between the two HRS polarities. Some of the fluctuations near run number 5200 were caused by the level-one accept issue mentioned in Section 3.7.5.

3.7.10 Proximity RICH Analysis

The new Hall A proximity focusing RICH (upgrade of the original RICH used for the Hypernuclear spectroscopy experiments), has been operated in the Transversity experiment to help identify the final-state hadrons generated in the deep inelastic events: protons, kaons and pions up to 2.5 GeV/c.

The detector uses 15 mm thick C_6F_{14} liquid freon at standard temperature and pressure as a Cherenkov radiator.

After traveling a proximity gap of 159 mm, Cherenkov photons in the ultraviolet region (160-220 nm, mean freon refractive index=1.287) are converted (with $\sim$ 25% quantum efficiency) into electrons by a 300 nm layer of CsI. The CsI is deposited on top of 19200 8×8.4 mm^2 pads of the 2×0.6 m^2 multipad proportional chamber, which is filled by CH_4 at standard temperature and pressure. The positive ions, which are produced by the converted electrons and their secondaries in the electrostatic field ($10.5 - 11.5$ kV/cm) in the 2 mm chamber gap, are collected by the pads and read out by front-end electronics based on the Gassiplex chip. The chamber has been operated stably between 2100 and 2300 V with very marginal discharge events.

At 2.4 GeV/c particle momentum, the expected Cherenkov angles for electron, pion, kaon and proton are respectively: 0.680, 0.678, 0.654 and 0.583 rad.

Cumulated detected Cherenkov rings are represented in Fig. 73. The rings are well represented by a circle, demonstrating the proper geometrical set-up of the detector.

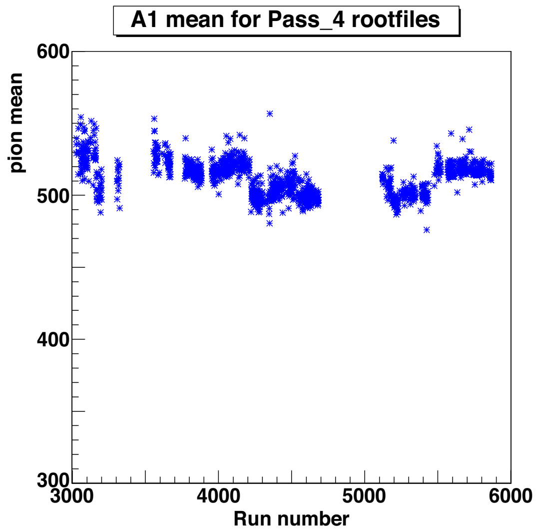

Figure 72: A1 stability check for production runs throughout experiment E06-010. There are two time periods: L-HRS in negative polarity and positive polarity (between run numbers 4223 and 5435).

The detector performance in terms of the number of detected photoelectrons (partially unfolded by the noisy hits) is reported in Fig. 74 as a function of the run number. In the last period of data taking, where the photoelectrons are expected to come almost exclusively from true Cherenkov photons, the mean number of photoelectrons is slightly larger than 9. This number is lower than the expected 12 (according to the quantum efficiency measured right after the deposition of the CsI photo-converter)[2]. The lower number of detected photoelectrons explains the larger angular resolution: from the expected ~ 6 mrad to the observed ~ 7 mrad which is close to $6 \times \sqrt{12}/\sqrt{9} = 6.9$.

The stability of the detector combined with the reconstruction algorithm is summarized in Fig. 75, where the reconstructed angle and its resolution are shown. The better performance of the detector in the last period of data taking is likely due to the refill of the freon and an improvement of the trigger logic.

In fact, during the experiment, the RICH suffered one major and only partially solved problem: a significant number of events was affected by a very large number of noisy hits; this noise has been studied as a function of single channel collected charge threshold without showing noticeable effect. Moreover, no HV dependence has been observed, which excludes an internal (to the chamber) origin of the multiple-hit events. The most likely source of these disturbing events may be represented by a tricky malfunctioning of one of the trigger logic components, such as the digital delay unit that was used to delay the track and hold signal sent to the Gassiplex front-end cards.

Analysis is underway to optimize the detector performance and complete the detector characterization; the detector will be used in combination with the Aerogel counter and Time of Flight information to extract the kaon production and asymmetry as well as antiproton production.

References

[1] HERMES measurements of Collins and Sivers asymmetries from a transversely polarised hydrogen target, arXiv:0706.2242.

[2] A. Airapetian *et al.*, [HERMES Collaboration], Phys. Lett. B **679** (2009) 100.

[3] M. Alekseev *et al.*, [COMPASS Collaboration], Phys. Lett. B **673** (2009) 127.

[2] The lower number of photoelectrons may come either from a degradation of the CsI deposition due to unintentional exposition to air and humidity during the fixing of one broken wire, which required the opening of the RICH, or a worse transparency of the freon radiator.

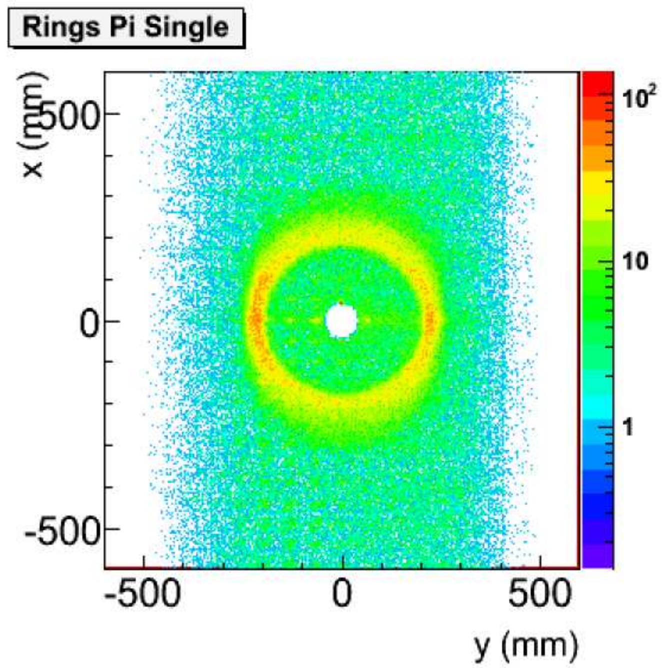

Figure 73: Cumulated Cherenkov rings generated by charged pions at 2.4 GeV/c ±5% ; the central region contains the intense signal produced by the charge particle (as minimum ionizing particle) which has been masked to enhance the ring pattern.

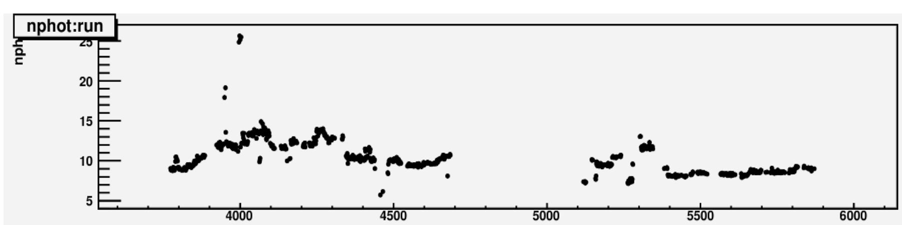

Figure 74: Number of detected Cherenkov photoelectrons, partially unfolded by the noisy hits. The true number of photoelectrons (signal) $N_{PE} \sim 9$ has been estimated in the last period of data taking (refer also to Fig. 75).

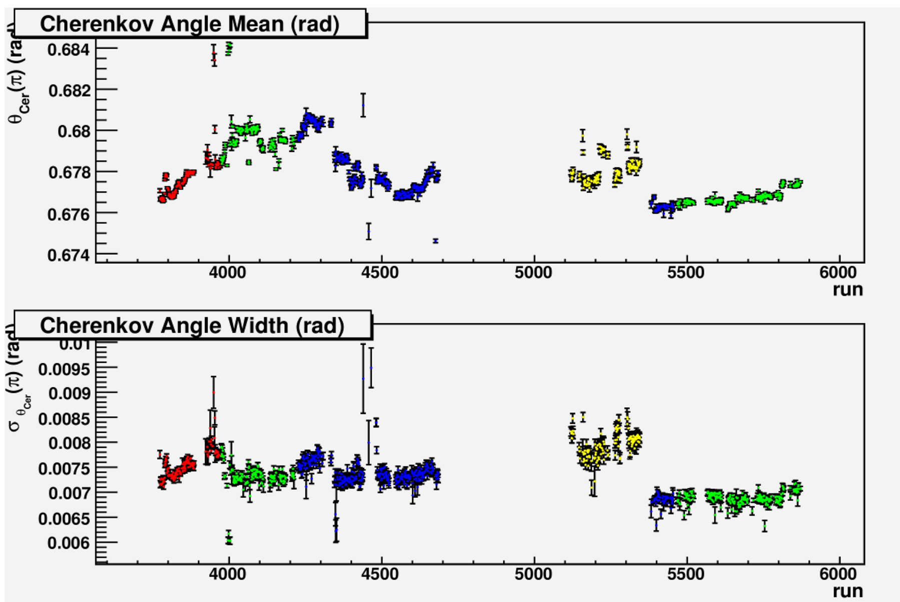

Figure 75: Reconstructed Cherenkov angle for pions (upper plot), and its resolution (lower plot); note that the variation of the reconstructed angle is largely within the angular resolution. The different colors correspond to different particle polarities (green=negative, blue=positive) or different conditions: red points have been acquired before a 45 ns change in the GATE signal delay which has significantly lowered the detector efficiency; yellow points malfunctioning due to a bad configuration of the trigger logic. The large gap around run 5000 corresponds to the Christmas shutdown. A net improvement in the angular resolution is evident after the refilling of the liquid radiator, when it drops below 7 mrad. No minimum photoelectron detection is applied to the data.

[4] Single Spin Asymmetries on a transversely polarised proton target at COMPASS, arXiv:0808.0086.

[5] JLab E02-013, Measurement of the Neutron Electric Form Factor G_E^n at High Q^2, G. Cates, N. Liyanage and B. Wojtsekhowski, spokespersons.

[6] JLab E04-007, Precision Measurements of Electroproduction of π_0 near Threshold: A Test of Chiral QCD Dynamics, J. Annand, D. Higinbotham, R. Lindgren, B. Moffit, V. Nelyubin and B. Norum, spokesperson.

[7] JLab E08-007, Measurement of the Proton Elastic Form Factor Ratio at Low Q^2, J. Arrington, D. Day, R. Gilman, D. Higinbotham, G. Ron and A. Sarty, spokesperson.

[8] N. Liyanage, Jefferson Lab Tech Note, **JLAB-TN-02-012**

[9] http://www.jlab.org/~jinhuang/HRSOptics

[10] http://hallaweb.jlab.org/root/doc/html_v15/THaVDC.html

[11] http://seal.web.cern.ch/seal/MathLibs/Minuit2/html/index.html

[12] C. Curtis *et al.*, Jefferson Lab Alignment Group Data Transmittal, **A1189, A1197, A1198 and A1208**

[13] J. Huang, Transversity Analysis Log, **173**
http://www.jlab.org/~jinhuang/Meeting/2009.09.25

[14] J. Huang, Hall A Weekly Meeting Talk
http://www.jlab.org/~jinhuang/Meeting/2009.09.15

3.8 E06-014

A Precision Measurement of d_2^n: Probing the Lorentz Color Force

S. Choi, X. Jiang, Z.-E. Meziani, B. Sawatzky, spokespersons, and
the d_2^n and Hall A Collaborations.
Contributed by D. Flay.

3.8.1 Overview

Physics Motivation

To date, extensive work has been done investigating the spin structure function g_1 within the context of the Feynman Parton Model and pQCD. However, far less is known about the g_2 structure function. It is known to contain quark-gluon correlations, and its study could possibly yield a better understanding of the nature of confinement. It represents a spin-flip Compton amplitude, and may be written as:

$$g_2\left(x,Q^2\right) = g_2^{WW}\left(x,Q^2\right) + \bar{g}_2\left(x,Q^2\right), \tag{8}$$

where g_2^{WW} is the Wandzura-Wilczek term, which may be expressed entirely in terms of g_1 [1]:

$$g_2^{WW}\left(x,Q^2\right) = -g_1\left(x,Q^2\right) + \int_x^1 \frac{g_1\left(y,Q^2\right)}{y}dy. \tag{9}$$

The second term is given as:

$$\bar{g}_2\left(x,Q^2\right) = -\int_x^1 \frac{1}{y}\frac{\partial}{\partial y}\left[\frac{m_q}{M}h_T\left(y,Q^2\right) + \xi\left(y,Q^2\right)\right]dy, \tag{10}$$

where h_T is the transverse polarization density, and ξ is a twist-3 dominated term arising from quark-gluon correlations. Here, h_T is suppressed by the ratio of the quark mass m_q to that of the target mass M. Therefore, a measurement of $\bar{g}_2$ provides access to twist-3 effects inside the nucleon [2].

Subsequently, a measurement of both g_1 and g_2 allows for the determination of the quantity d_2^n, which is formed as the second moment of a linear combination of g_1 and g_2:

$$d_2^n\left(Q^2\right) = \int_0^1 x^2\left[2g_1\left(x,Q^2\right) + 3g_2\left(x,Q^2\right)\right]dx = 3\int_0^1 x^2\bar{g}_2\left(x,Q^2\right)dx. \tag{11}$$

d_2^n also appears as a matrix element in the operator product expansion [3]:

$$g\langle P,S \mid \bar{\psi}_q\left(0\right)G^{+y}\left(0\right)\gamma^+\psi_q\left(0\right) \mid P,S\rangle = 2MP^+P^+S^x d_2^n, \tag{12}$$

where $G^{+y} = \frac{1}{\sqrt{2}}\left(B^x - E^y\right)$. We see from Eq. 11 that d_2^n is a direct measure of quark-gluon interactions. Eq. 12 may be written in component form,

$$\langle P,S \mid \psi_q^\dagger \vec{\alpha}\times g\vec{E}\psi_q \mid P,S\rangle = 2M^2\chi_E\vec{S} \quad \text{and} \quad \langle P,S \mid \psi_q^\dagger g\vec{B}\psi_q \mid P,S\rangle = 2M^2\chi_B\vec{S}, \tag{13}$$

from which d_2^n may be written as $d_2^n = \frac{1}{8}\left(\chi_E + 2\chi_M\right)$.

In the limit of low Q^2 where the virtual photon wavelength is larger than the nucleon size, the electromagnetic field of the virtual photons associated with g_2 in the interaction will appear as uniform over the nucleon volume. Consequently, d_2^n is seen to be connected with spin polarizabilities [4].

Recent work has shown [4, 5] that at high Q^2, d_2^n is more appropriately seen as a color Lorentz force averaged over the volume of the nucleon. This is given by the expression of the transverse (color) force on the active quark immediately following its interaction with a virtual photon:

$$F^y\left(0\right) \equiv -\frac{\sqrt{2}}{2P^+}\langle P,S \mid \bar{\psi}_q\left(0\right)G^{+y}\left(0\right)\gamma^+\psi_q\left(0\right) \mid P,S\rangle = -\frac{1}{2}M^2 d_2^n. \tag{14}$$

This theoretical interpretation reveals how g_2 and subsequently d_2^n will allow us to examine some of the properties of confinement with great precision.

Current Status and Goals

While bag and soliton model calculations of d_2 for the neutron yield numerical values consistent with those of Lattice QCD, current experimental data differs by roughly two standard deviations. One of the intentions of our experiment is to improve the experimental error on the value of d_2^n by a factor of four. It subsequently provides a benchmark test on Lattice QCD calculations.

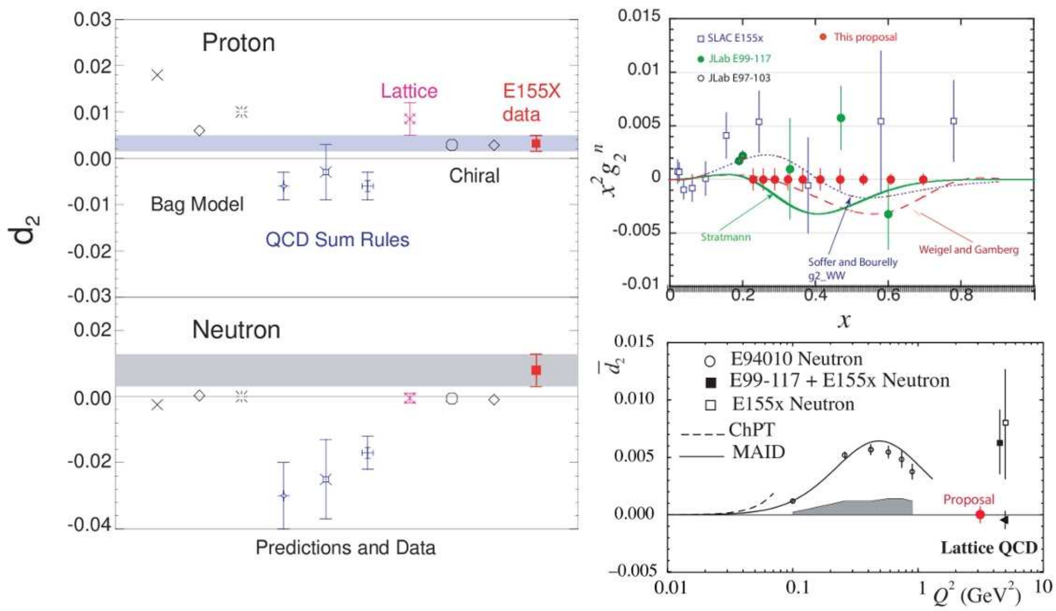

Figure 76: On the left are the current world data on d_2 [6]. There is a need for more precise neutron data, which E06-014 addresses. On the right is the projected error on both $g_2(x)$ (top) and d_2^n $(\sim 3\ \text{GeV}^2)$ (bottom).

3.8.2 The Experiment

The experiment ran in Hall A of Jefferson Lab from February to March of 2009, with two beam energies of $E = 4.73$ and 5.89 GeV, covering the resonance and deep inelastic valence quark regions, characterized by $0.2 \leq x \leq 0.7$ and $2 \leq Q^2 \leq 6\ \text{GeV}^2$.

In order to calculate d_2^n, we scattered a longitudinally polarized electron beam off of a ^{3}He target, in two polarization configurations – longitudinal and transverse. ^{3}He serves as an effective neutron target since roughly 86% of the polarization is carried by the neutron. This is due to the two protons in the nucleus being primarily bound in a spin singlet state [7, 8].

We measured the unpolarized total cross section σ_0 and the asymmetries $A_\parallel$ and $A_\perp$. The cross section was measured by the Left High-Resolution Spectrometer (LHRS), while the asymmetries were measured by the BigBite Spectrometer. Both the LHRS and BigBite were oriented at scattering angles of $\theta = 45°$ to the left and right of the beamline, respectively.

Expressing the structure functions entirely in terms of these experimental quantities, we have the expression for d_2^n:

$$d_2^n = \int_0^1 \frac{MQ^2}{4\alpha^2} \frac{x^2 y^2}{(1-y)(2-y)} \sigma_0 \left[\left(3 \frac{1 + (1-y)\cos\theta}{(1-y)\sin\theta} + \frac{4}{y} \tan(\theta/2) \right) A_\perp + \left(\frac{4}{y} - 3 \right) A_\parallel \right] dx, \tag{15}$$

where $x = Q^2/2M\nu$, $\nu = E - E'$ is the energy transfer to the target, E' is the scattered electron energy, and $y = \nu/E$ is the fractional energy transfer to the target. The asymmetries are given by:

$$A_{\parallel} = \frac{\sigma^{\downarrow\Uparrow} - \sigma^{\uparrow\Uparrow}}{2\sigma_0} \quad \text{and} \quad A_{\perp} = \frac{\sigma^{\downarrow\Rightarrow} - \sigma^{\uparrow\Rightarrow}}{2\sigma_0}.$$

3.8.3 Analysis Progress

The Left High-Resolution Spectrometer

Before we can begin to identify particles in the LHRS, we need to calibrate our detectors. Both the gas Čerenkov and the pion rejector have been calibrated so that we may be able to discern electrons from pions.

First, each of the ten photomultiplier tubes (PMTs) in the gas Čerenkov were gain-matched by use of our Hall A Analyzer database, so that each of their one photoelectron peaks aligns to a specified value in their corresponding ADC spectrum. This allows us to determine the average photoelectron yield of each PMT. In the pion rejector, a similar process was followed for each PMT corresponding to each of the thirty four blocks in each layer of the pion rejector. We used the gas Čerenkov to identify pions in the pion rejector, and gain-matched each block's pion ADC spectrum to an arbitrary specified value. This was carried out for one particular momentum setting in the LHRS [9]. The resulting calibration coefficients were then applied to all other kinematics. The calibration is carried out in this fashion since pions will deposit roughly the same amount of energy in the pion rejector regardless of their momentum.

Currently, work is being done to determine the electron detection, pion rejection, and cut efficiencies for both the gas Čerenkov and the pion rejector. Figure 77 shows the pion rejection (cut) efficiency of the gas Čerenkov in the LHRS. A pion sample is selected in the pion rejector (N_i) and those events that pass the given cut in the Čerenkov (N_f) have their corresponding Čerenkov spectrum plotted. Then, the ratio $r = N_f/N_i$ is calculated. The formula for the efficiency of rejecting pions for the particular cut position in the gas Čerenkov is then written as $\epsilon_{\text{cer}}^{\pi-\text{rej.}} = 1 - r$, as this quantity reflects the percentage of pions removed by a cut in the gas Čerenkov. These quantities will be a contributing factor in the determination of the unpolarized total cross section, σ_0.

Simulation work concerning the pion rejector is also being carried out to better understand the momentum dependence observed in our E/p distribution as a function of p (Fig. 77).

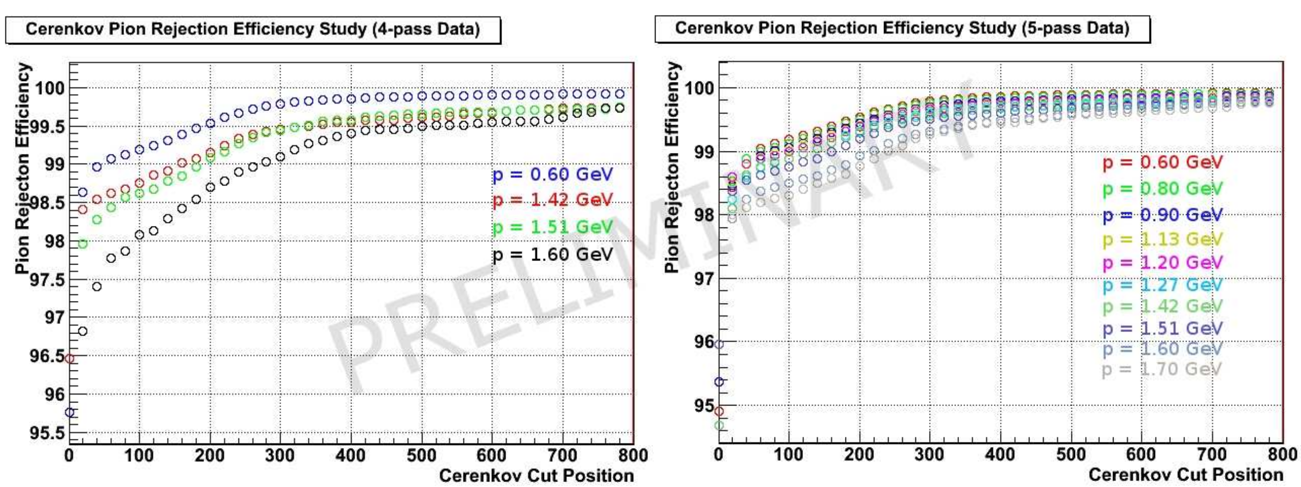

Figure 77: Gas Čerenkov pion rejection efficiency study for 4- and 5-pass data.

The BigBite Spectrometer

In addition to the multiwire drift chambers and the shower calorimeters, this experiment was one of the first to use the gas Čerenkov detector in the BigBite detector package. The Čerenkov detector uses C_4F_{10} as the radiator gas. The Čerenkov radiation is focused from two sets of ten mirrors into twenty PMTs, each of which views one mirror. The Čerenkov detector is needed for electron detection and added pion rejection.

The Čerenkov detector is calibrated by gain-matching the one photoelectron peak for each PMT to a particular ADC channel by adjusting the gain of the PMT during LED runs taken during the running of d_2^n. The photoelectron yield per electron track during the production mode of the experiment is approximately six. Figure 78 shows the ADC signal from one of the PMTs. The plot on the left shows an electron signal. The green curve has no TDC cuts, while the blue curve has cuts on the main timing peak of the corresponding TDC spectrum. The red curve has a cut outside the main timing peak in its TDC spectrum. The plot on the right shows the effect of mirror cuts in addition to the aforementioned TDC cuts. The electron signal is shown in green, which requires a reconstructed track to pass through the mirror associated with that particular PMT. The red curve shows background effects, and requires a reconstructed track to *not* pass through the mirror associated with this particular PMT.

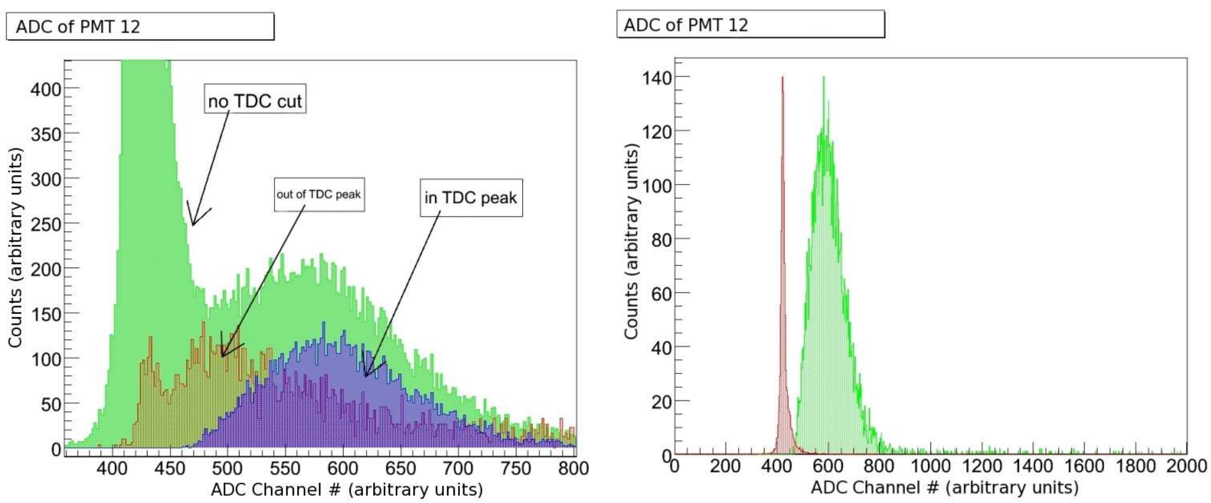

Figure 78: Sample histograms of a calibrated Čerenkov ADC spectrum for one of the mirrors. The plot on the left shows the effect of TDC cuts. The plot on the right shows the effect of TDC and mirror cuts.

Currently, work is being done to calibrate the preshower and shower calorimeters. Once this detector is calibrated, a study of electron detection, pion rejection, and cut efficiencies will be carried out. In addition to identifying electrons for the calculation of the asymmetries $A_\parallel$ and $A_\perp$, this study will also determine the magnitude of the pion background which may be removed from the gas Čerenkov and the total shower calorimeter.

The Compton Polarimeter

During the experiment, beam polarization was measured by the Møller polarimeter and by a partially upgraded Compton polarimeter. Although the Compton electron detector was disabled, the photon detector – a single cylinder of GSO crystal – allowed much higher resolution than the lead tungstenate array it replaced, especially at low energies. A comparison between Compton photon data from d_2^n and a Monte Carlo simulation led to the discovery of a misalignment in the Compton photon beamline, which was corrected over the summer.

This experiment also saw the commissioning of a new, integrating data acquisition system for the photon detector signal, as well as a corresponding suite of analysis software. Figure 79 shows preliminary results from this analysis for a month of d_2^n running. The four accelerator configurations for the experiment – each with a different nominal polarization – can be clearly distinguished. We are refining our Monte Carlo to compute the analyzing power of the Compton polarimeter, which will allow us to translate the raw Compton asymmetries to absolute beam polarizations.

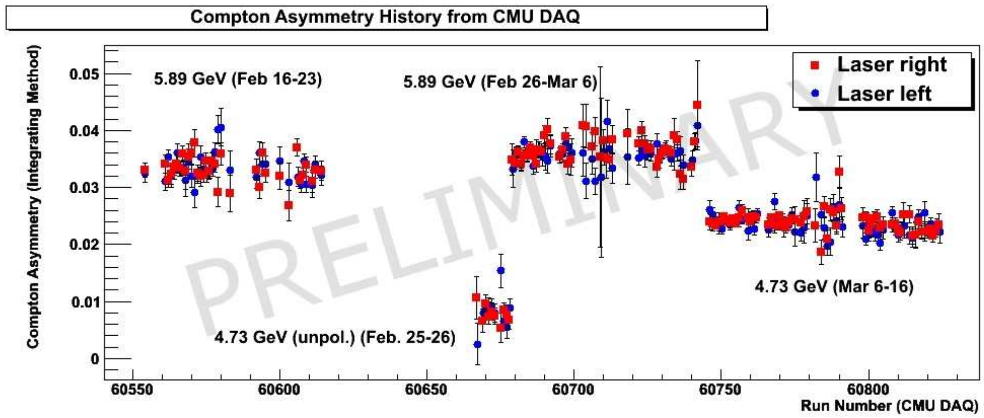

Figure 79: The asymmetry in the Compton beam polarimeter during the running of d_2^n.

References

[1] S. Wandzura and F. Wilczek, Phys. Lett. B **72**, 195 (1977).

[2] R.L. Jaffe, Comm. Nucl. Part. Phys. **19**, 239 (1990).

[3] B.W. Filippone and Xiandong Ji, hep-ph/0101224v1.

[4] M. Burkardt, hep-ph/0905.4079v1.

[5] M. Burkardt, hep-ph/0902.0163v1.

[6] S. Choi, Z.-E. Meziani, X Jiang, B. Sawatzky, *et al.*, Jefferson Lab, 2005; PR-06-014.

[7] J.L. Friar *et al.*, Phys. Rev. C **42**, 6 (1990).

[8] F. Bissey, A.W. Thomas and I.R. Afnan, Phys. Rev. C **64**, 024004 (2001).

[9] D. Flay, E06-014 Technical Note, in preparation.

3.9 PREX Developments in 2009

R. Michaels

The Lead Radius Experiment (PREX) will run at Jefferson Lab for two months starting in March 2010. The parity-violating asymmetry in elastic scattering $A = (\sigma_R - \sigma_L)/(\sigma_R + \sigma_L)$ arises from the the interference of the Z^0 boson amplitude of the weak neutral interaction with the photon amplitude. The asymmetry is sensitive mainly to the neutron radius R_n because the weak charge of the neutron is much larger than that of the proton [1].

In PWIA, the relationship between the asymmetry and the neutron form factor is given by equation (16)

$$A_{LR} = \frac{G_F Q^2}{4\pi\alpha\sqrt{2}}\left[1 - 4\sin^2\theta_W - \frac{F_n(Q^2)}{F_p(Q^2)}\right] \tag{16}$$

where G_F is the Fermi constant, $\alpha = \frac{1}{137}$ is the fine structure constant, θ_W is the Weinberg angle, and $F_n(Q^2)$ and $F_p(Q^2)$ are the neutron and proton form factor of the nucleus. Thus A_{LR} is a direct measurement of the ratio of neutron to proton form factors. The measurement is clean and can be interpreted with as much confidence as electron scattering measurements of the proton radius R_p [2]. Coulomb distortions are the largest correction and have been calculated by Horowitz[3].

The ^{208}Pb experiment will run at a 1.05 GeV energy with a new room-temperature septum magnet at 5°. The magnet was fabricated in 2009 and is ready to install. The two HRS focus elastically scattered electrons onto quartz Cerenkov detectors in their focal planes. The final concept for the detectors were tested during the initial days of HAPPEX-III in September 2009. It will work well and have an acceptable resolution.

A 50 μA, 80% polarized beam with a 240 Hz helicity reversal will scatter from a foil of lead which is sandwiched between sheets of diamond to improve the thermal characteristics. Separate studies at lower rates are required to measure backgrounds, acceptance, and Q^2. The beam polarization P_e is measured twice a week by a Møller polarimeter, and monitored continuously with the Compton polarimeter. The raw asymmetry $P_e\ A$ of 0.5 ppm must be measured to 3% accuracy. Both the absolute error (15 ppb) and the relative accuracy (3%) are challenging to achieve.

A new collimator is being made, see Fig. 80. It fits in the entrance of Q1 and defines the acceptance; simulations have been used to confirm that no other aperture defines the acceptance. The collimator will be carefully aligned by a survey so that the two HRS, without septa, have identical scattering angles. A placement error of 1 mm can be achieved and is sufficient to suppress a possible transverse asymmetry arising from a residual vertical polarization. This will work if the septum magnet is built up with reasonable symmetry. This leaves the possible problem of horizontal polarization, i.e. a component in the plane of the floor. To become sensitive to this, we have a new trick: an Beryllium block(8 % radiation length) is placed at a "large" vertical angle inside the collimator. Electrons that pass through this block lose a few MeV of energy and end up in the focal plane displaced from the elastic peak, though with background from the radiative tail. A special detector will measure the asymmetry from these events, giving a bound on the horizontal polarization systematic.

A new "double-Wien filter" has been fabricated and will be installed at the injector beamline in Jan 2010 by the Polarized Injector Group. This device allows us to flip the helicity (about once a week) using an arrangement of solenoids that should, to a good approximation, flip the helicity without changing any other parameter of the beam. This will be important for understanding and canceling subtle higher-order effect in the asymmetry such as a possible helicity-correlated change in the spot size. Laser table measurements at UVa have also studied this helicity-correlated spot size variation and placed bounds on its anticipated size.

Simulations are being performed to understand the sensitivity of the experiment to different physics models. The relationship between the measured asymmetry A_{meas} and theory A_{theory} is

$$A_{\text{meas}} = \frac{\int d\Omega \epsilon(\theta,\phi)\frac{d\sigma}{d\Omega}A_{\text{theory}}}{\int d\Omega \epsilon(\theta,\phi)\frac{d\sigma}{d\Omega}} \tag{17}$$

where $\epsilon(\theta, \phi)$ is the acceptance of the spectrometer.

The simulated acceptance function, averaged over azimuth ϕ is shown in Fig. 81. This function will be measured precisely during the experiment and published together with the measured asymmetry. To match theory with experiment one must integrate the theoretical asymmetry using Eq. 17. A preliminary study of

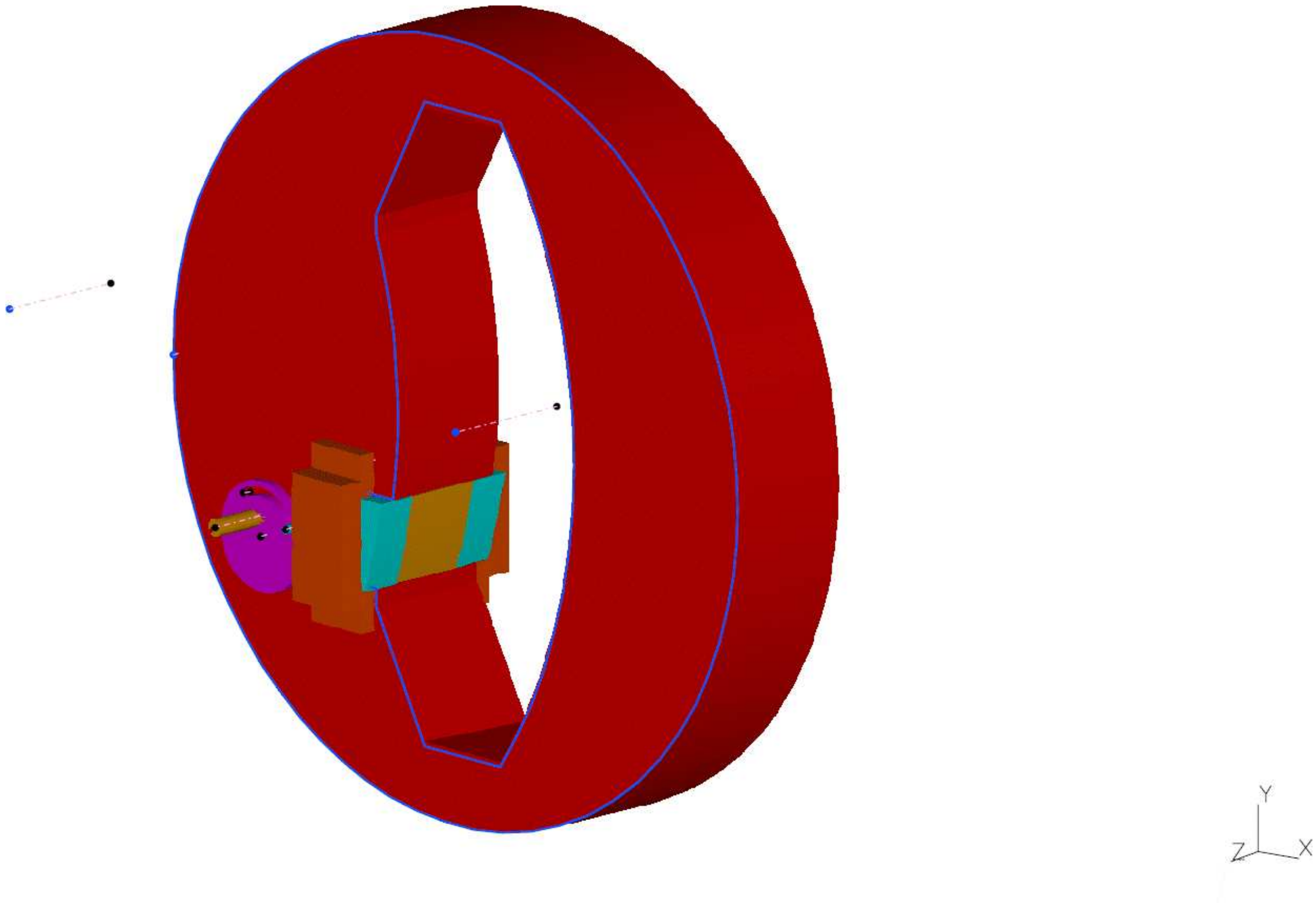

Figure 80: Conceptual drawing of the PREX collimator. The Be plug is shown near the bottom of the aperture. It can be blocked by a remotely actuated tungsten plug.

this matching has been done with published models [4], see Fig. 82. This shows the discriminating power of the experiment. A forthcoming publication will address this issue and the application to other nuclei.

Upgrades to our polarimeters are of vital importance. Tests of the Compton integrating photon DAQ have been successful and a new Silicon microstrip detector (Edet) has been installed to detect the scattered electrons. The Edet worked fairly well during HAPPEX-III, providing a calibration of the response function of the photon detector and an independent measurement of the asymmetry. Unfortunately, during PVDIS the Edet was swamped with background (about 100:1) and did not work. It remains to be seen how well the Edet works during PREX.

The Møller polarimeter is being upgraded to use a 4 T field which saturates the target foil and reduces the systematic error following the design of Ref. [5]. In addition, a new FADC-based DAQ has been deployed to reduce the dead time and understand pile-up effects in detail. This new DAQ has been commissioned during the PVDIS experiment and is now providing reasonable results.

At the time of this writing the January shutdown is about to begin and we have a tremendous amount of work to do to mount this experiment.

References

[1] T.W. Donnelly, J. Dubach, and I. Sick, Nucl. Phys. A**503**, 589 (1989).

[2] H. de Vries, C. W. de Jager, and C. de Vries, Atomic and Nuclear Data Tables, **36**, 495 (1987).

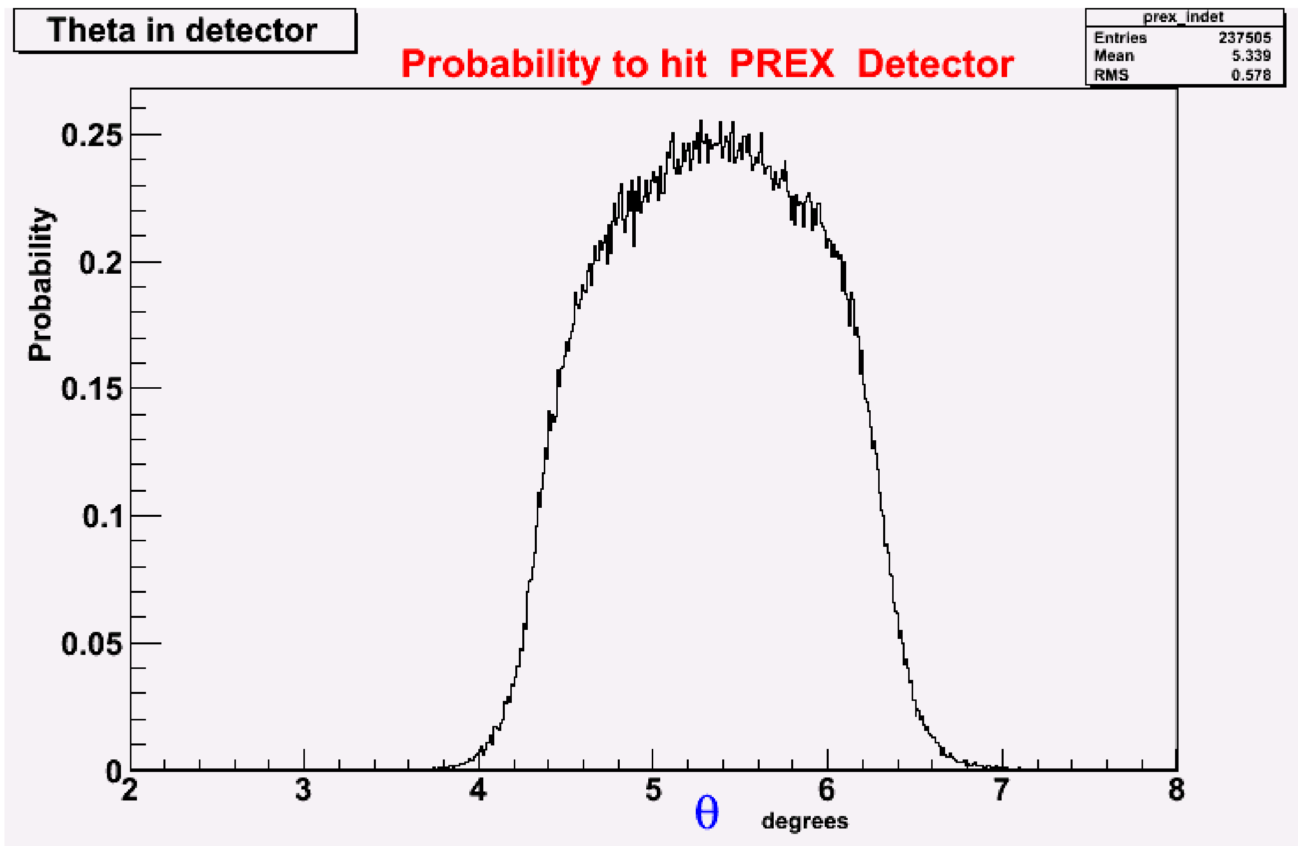

Figure 81: Simulated acceptance function for the HRS with 5° septum magnet integrated over azimuth. This will also be measured.

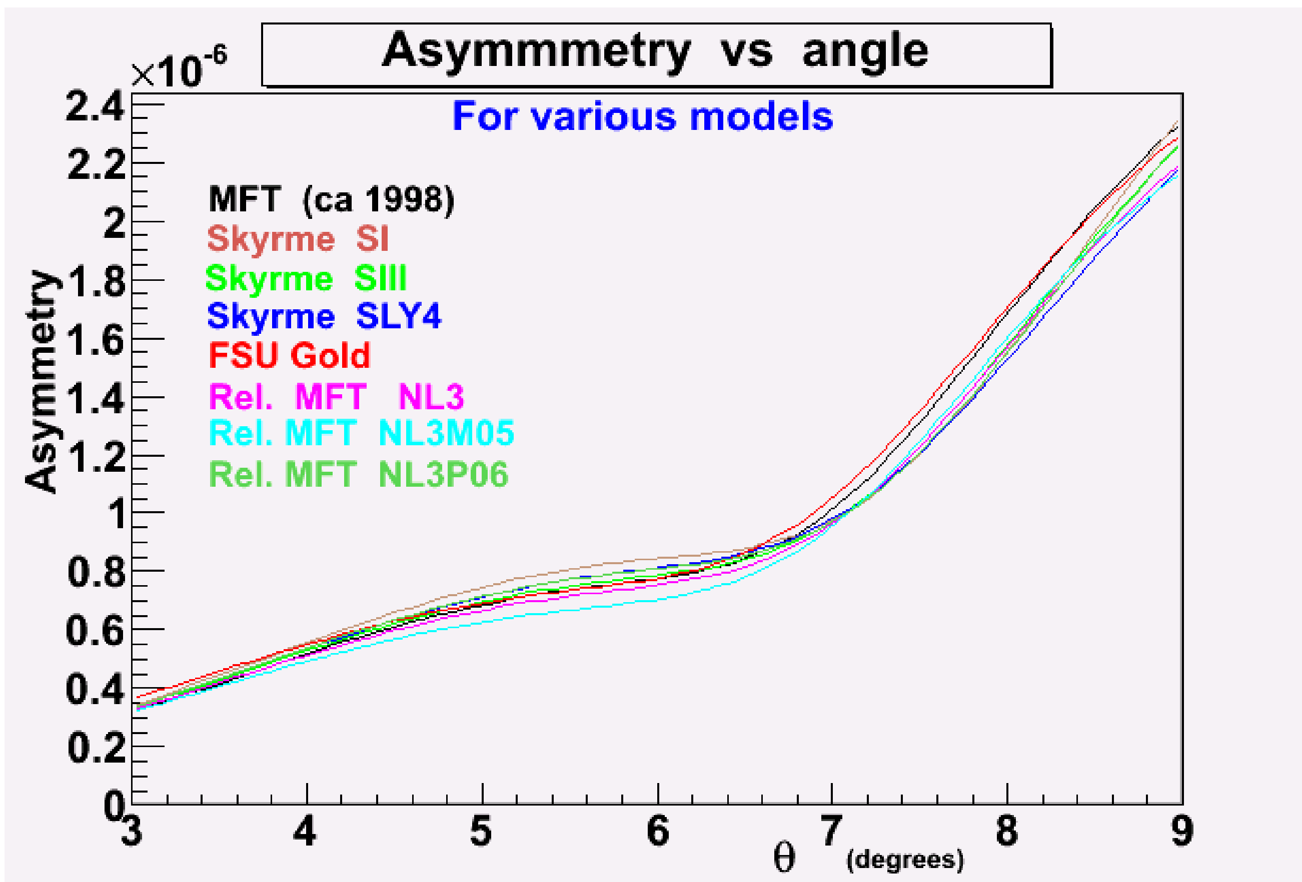

Figure 82: Asymmetry models from published literature by C.J. Horwitz. See reference in text.

[3] C. J. Horowitz, Phys. Rev. C **57**, 3430 (1998).

[4] C. J. Horowitz, private communication.

[5] M. Hauger *et al.* Nucl. Instrum. Meth. A**462** 382 (2001).

3.10 E07-013

A Measurement of the Target Normal Single-Spin Asymmetry in Inclusive DIS Scattering

Todd Averett, Tim Holmstrom, Ron Gilman and Xiaodong Jiang, spokespersons,
and
the Hall A Collaboration.
contributed by Joseph Katich

The Experiment

E07-013 aims to measure the target single-spin asymmetry (SSA) in inclusive DIS scattering of electrons from a vertically polarized ^{3}He target. The reaction channel is a clean window into the realm of 2γ physics, as the asymmetry is identically zero in the Born approximation. A non-zero asymmetry would be a clear indication of a 2γ effect. The experiment ran parasitically to E06-010 ('Transversity') from late October 2008 until early February of 2009, during which more than 16 C of 'good' vertical-target production data were acquired.

^{3}He Target

E07-013 implemented recently developed 'hybrid' ^{3}He cells; the second experiment to do so. This modification to the cells allows the in-beam target polarization to reach nearly 50%. Further, the usual FAP Coherent lasers here replaced with narrow-band lasers that better match the absorption spectrum of Rubidium. This is the first experiment to use these lasers with the ^{3}He set-tup, and the result was another increase of in-beam polarization, reaching better than 60% (absolute).

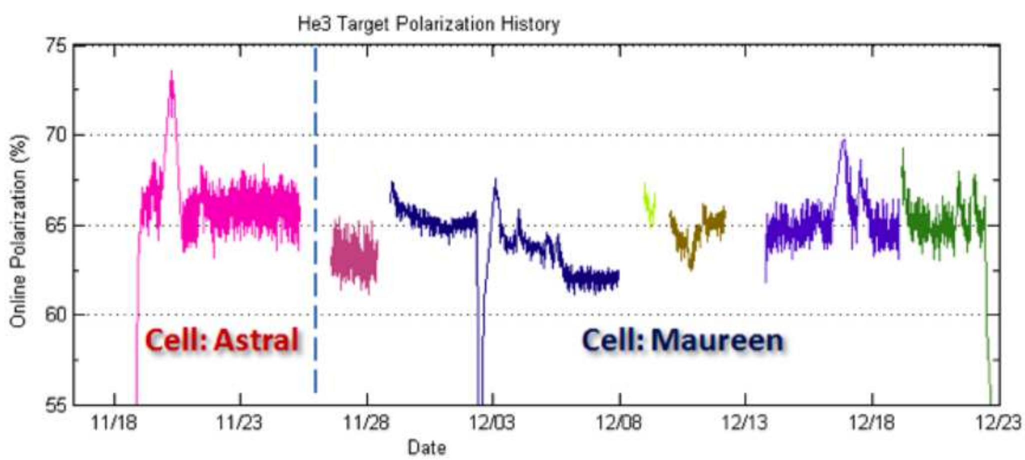

Figure 83: Target Polarization for November '08 through December '08

The experiment also took advantage of a highly modified ^{3}He oven and laser set-up that was designed to provide target polarization along any of X,Y or Z axes. This new feature allowed not only for the vertical (out of scattering plane) target polarization that is needed to maximize the 2γ signal, but also transverse (in-plane) polarization for a systematic check.

Analysis Progress

The biggest challenge regarding data analysis is the separation of electrons from background in the BigBite detector. The experiment originally called for use of a Cherenkov detector as the main means of P.I.D. Unfortunately, this detector was unavailable at the time of running, and we are left with the BigBite preshower and shower detectors as our only source of particle identification. Despite this complication, we have managed to achieve what we believe to be very reliable separation of particles thanks to an excellent detector calibration. Once calibrated, a cut on preshower, momentum and E/p combined with tracking and optics cuts lead to an electron sample with less than 5% π^- contamination.

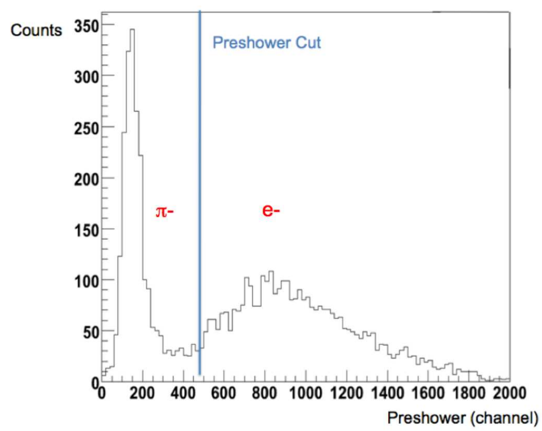

Figure 84: BigBite preshower spectrum, cut shown in blue

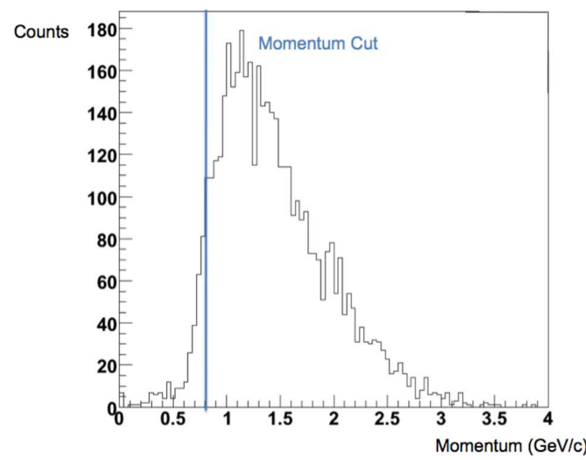

Figure 85: BigBite momentum spectrum, cut shown in blue

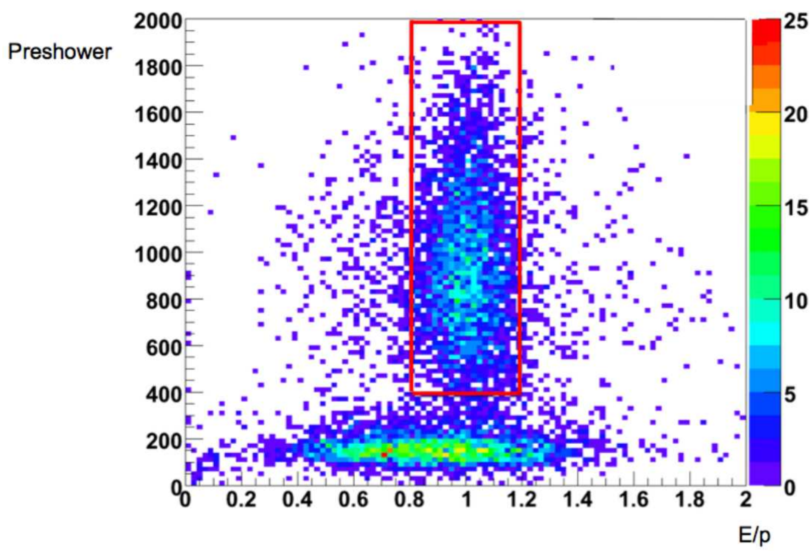

Figure 86: BigBite preshower vs. E/p spectrum, cut shown in red

Preliminary Results

Preliminary raw asymmetries are plotted in Fig. 3.10. Only statistical error is shown. Target polarization and other dilution factors are yet to be accounted for. The top plot is for trigger 1, which is a combination of BigBite preshower and shower. The lower plot is trigger 6, which is the same as T1, but with a higher threshold to reduce the pion acceptance.

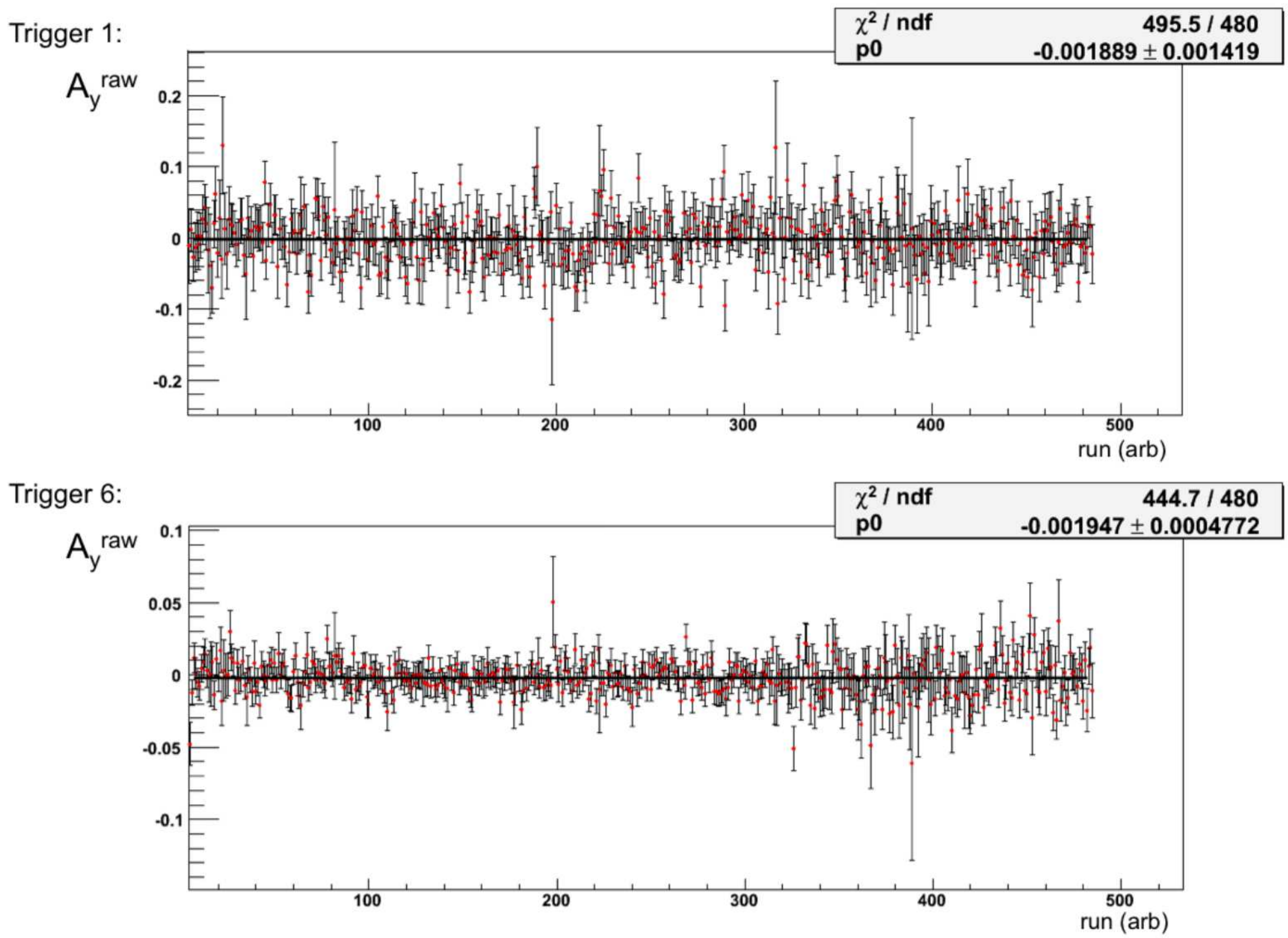

Figure 87: Single-Spin Asymmetry A_y vs. run, vertically polarized ^{3}He target

Remaining Tasks

- estimation of π^0 contamination
- finalize and incorporate target polarization and dilution factors
- apply radiative corrections
- estimation of systematic errors

3.11 E08-007

Measurement of the Proton Elastic Form-Factor Ratio at Low Q^2

X. Zhan, J. Arrington, D. Day, R. Gilman, D.W. Higinbotham, G. Ron, A.Sarty
for the Hall A Collaboration

3.11.1 Introduction

Polarization-transfer data at $Q^2 > 1$ GeV^2 have indicated a strong deviation of the proton form-factor ratio from unity [1]. Recent data [2, 3] at low Q^2 have indicated there may be deviations of the ratio from unity even at Q^2 <1 GeV^2. The goal of E08-007 is to vastly improve the knowledge of the proton form-factor ratio at low Q^2 (0.3 GeV^2 - 0.7 GeV^2) through the recoil polarization method. In combination with separate cross-section data, it will also allow significant improvements in the knowledge of the individual form factors.

Beyond the intrinsic interest in the structure of the nucleon, improved knowledge of the form factor also has implications for DVCS, the proton Zemach radius, and the extraction of the strange quark content of the nucleon through parity violation experiments. The new data also may have implications for two-photon calculations. In order to cancel a divergence, box diagrams have always been included in radiative correction calculations [4] though with approximations. Modern calculations are now making more complete calculations, such as [5], but it is difficult to calculate the state between the two virtual photons as it does not need to be an on-shell proton. Differences between polarization data and cross-section data at low Q^2 would imply incompleteness in the radiative corrections as the polarization data should be little affected by this correction.

3.11.2 Experiment

The experiment ran 15 May 2008 through 9 June 2008 with beam polarization ∼80% and a beam energy of 1.192 GeV. The left high-spectrometer (HRS) to detect the recoil protons in coincidence with the elastic scattered electrons detected by BigBite. The focal-plane polarimeter installed in HRS was used to measure the recoil polarization of the proton. Table 12 lists the measured kinematics. The experiment was able to achieve < 1% statistical uncertainties for all the kinematics.

Table 12: Kinematics for HRSL and BigBite. For each Q^2, there are 3 different spectrometer momentum settings (centering the protons at about δ=-2%, 0%, and +2%) to cover different regions on the focal plane.

Q^2 GeV^2	θ_p [deg]	P_p [GeV/c]	θ_e [deg]	P_e [GeV/c]
0.30	60.0	0.565	30.0	1.03
0.35	57.5	0.616	30.0	1.01
0.41	55.0	0.668	35.0	0.978
0.45	53.0	0.710	35.0	0.954
0.50	51.0	0.752	40.0	0.928
0.55	49.0	0.794	40.0	0.901
0.60	47.0	0.836	45.0	0.874
0.70	43.5	0.913	50.0	0.823

For each kinematic setting, only the region of the BigBite shower blocks that were being hit by elastic electrons were turned on to maximize the number of good elastic events written to tape. For each setting, aluminum dummy data were taken for background estimation.

3.11.3 Analysis

The analysis of the Al dummy data have shown that the Al contributes a background of less then 0.3%. The accidental background is also small (< 0.3%). Many different optics databases have been used to check the HRS data. In particular, an old database from Higinbotham and Rvachev as well as new databases from

Jin Huang and Jin Ge. These high-quality databases not only gave nearly identical results for the proton; it also shows the stability of the HRS system as the databases were made nearly ten years apart in time.

The major source of uncertainty comes from the proton spin precession inside the spectrometer, which is crucial in determining the form factor ratio; never-the-less, the errors on all the data points (statistical and systemic) is at the $1-2\%$ level.

3.11.4 Results

The new data indicate that the form-factor ratio does indeed continue to be less than one even in the range of Q^2 from 0.3 to 0.7 GeV^2. Since this are the highest precision proton form-factor ratio data in this Q^2-range, it is interesting to see how it effects the previously reported difference in the low missing momentum D$(e,e'p)$ data and H$(e,e'p)$ elastic data. In Table 13, one can see how the new data improves the agreement between D$(e,e'p)$ data at low missing momentum and the free proton. Thus, it was the proton and not the deuteron that was causing the disagreement that was noted in the publication [6].

Table 13: The results from B. Hu [6] along with the new proton form-factor data from E08-007. By including the new data the χ^2/n of the data for a flat line goes from 1.7 to 0.7, thus becoming consistent with the low-p_m $(e,e'p)$ reaction from deuterium being nearly equal to the free proton case. Do note that for the high Q^2-point of 1.61, there are large systematics errors in determining the individual ratios that cancel in the ratio.

Q^2 GeV^2	$\mu G_E/G_M$ D$(e,e'p)$	$\mu G_E/G_M$ H$(e,e'p)$	Old Ratios P_d/P_{free}	$\mu G_E/G_M$ New Data	New Ratio P_d/P_{free}
0.43	0.92 ± 0.03	0.99 ± 0.03	0.92 ± 0.04	0.93 ± 0.01	0.99 ± 0.03
1.00	0.88 ± 0.01	0.88 ± 0.02	1.00 ± 0.03		
1.61	0.93 ± 0.04	0.87 ± 0.04	1.08 ± 0.07		

The collaboration is working on the paper describing these results and a draft will be available to the Hall A collaboration in early in 2010.

References

[1] V. Punjabi *et al.*, Phys. Rev. C **71**, 055202 (2005).

[2] C.B. Crawford *et al.*, Phys. Rev. Lett. **98**, 052301 (2007).

[3] G. Ron *et al.*, Phys. Rev. Lett. **99**, 202002 (2007).

[4] L. W. Mo and Y. S. Tsai, Rev. Mod. Phys. **41**, 205 (1969).

[5] A. V. Afanasev, S. J. Brodsky, C. E. Carlson, Y. C. Chen and M. Vanderhaeghen, Phys. Rev. D **72**, 013008 (2005).

[6] B. Hu *el al.*, Phys. Rev. C **73** 064004 (2006).

3.12 E12-07-109

Large-Acceptance Proton Form-Factor Ratio Measurements to 15 GeV^2 Using the Recoil-Polarization Method

E. Brash, E. Cisbani, M. Jones, M. Khandaker, L. Pentchev, Ch. Perdrisat, V. Punjabi, B. Wojtsekhowski (spokespersons),
and
The Electromagnetic Form Factor and Hall A Collaborations
(contributed by Vina Punjabi and Mahbub Khandaker)

3.12.1 Introduction

Nucleons are the building blocks of almost all ordinary matter in the universe. The challenge of understanding the nucleon's structure and dynamics has occupied a central place in nuclear physics, and experimental and theoretical physicists have spent a considerable amount of effort in the last five decades to understand it. A break-through was made towards this goal in the last decade, when the two JLab Hall A experiments obtained the elastic electromagnetic form-factor ratio of the proton, G_E^p/G_M^p, from measured recoil proton polarization components, using the recoil polarization method [1, 2]. An important realization of the double-polarization approach to obtain the ratio at the large momentum transfer by measuring two polarization components simultaneously was first proposed at JLab in 1989 [3]; it is based on a combination of spin precession in a magnetic spectrometer and uses a proton polarimeter. The major advantage of the method, compared to cross-section measurements, is that in the Born approximation the form-factor ratio, G_E^p/G_M^p, is directly proportional to the measured transverse and longitudinal proton polarization components P_t/P_ℓ. Hence, only a single measurement is necessary, strongly decreasing the systematic uncertainties.

The results of the GEp(1) and GEp(2) experiments [4, 5, 6] in Hall A have stimulated a huge amount of theoretical activity, as evidenced by the nearly 1000 combined citations of these papers, and by a revival of this field. An entirely new picture of the structure of the proton has emerged after the GEp(1) and GEp(2) experiments showed that the ratio G_E^p/G_M^p was in fact not constant, $\mu_p G_E^p/G_M^p \approx 1$, as suggested by the Rosenbluth separation method [7], but decreased by a factor of ~ 3.7 over the Q^2-range of 1 to 5.6 GeV^2. Recently, a third experiment, GEp(3) [8], measured the ratio to Q^2 of 8.5 GeV^2 in a Hall C experiment using the same recoil polarization method [1, 2]. The results from all three experiments are illustrated in Fig. 1, where they are also compared with Rosenbluth separation data [9, 10, 11, 12].

The meaning of the results of the GEp(1) and GEp(2) experiments seen in Fig. 1 is that the spatial distribution of the electric charge of the proton is "softer", *i.e.*, larger in extent (in the Breit frame) than its magnetization current distribution, which is definitively not intuitive. However, the relativistic boost required to transform these spatial distributions back to the laboratory frame are not trivial and only the form factors themselves are the relativistic invariants. Recently, G.A. Miller [13] has shown that a model independent charge distribution can only be defined on the wave front; the two-dimensional charge density on the wave-front is the Fourier transform of the Dirac form factor, F_1.

The preliminary results from the GEp(3) experiment show that the decreasing trend observed in the GEp(1) and GEp(2) experiments, may be slowing down. Although the ratio still decreases with Q^2, all of the new data come in higher than the linear fit to the Hall A data.

3.12.2 Experiment E12-07-109

The measurement of nucleon form factors to the highest possible Q^2 is one of the prime tenets of the JLab 12 GeV upgrade. Figure 89 makes it clear that the only way to achieve clarity in discriminating between theoretical explanations of the form-factor data is to measure the proton form- factor ratio with considerable precision to high values of Q^2.

The PAC32 in August of 2007 approved experiment **E12-07-109 (GEp(5))** [14] which will measure the proton's electromagnetic form factor ratio, G_E^p/G_M^p, to 15 GeV^2 using the recoil polarization technique. The experiment will use a large-acceptance spectrometer, to detect the recoil protons. A schematic representation of the experiment is shown in Fig. 90.

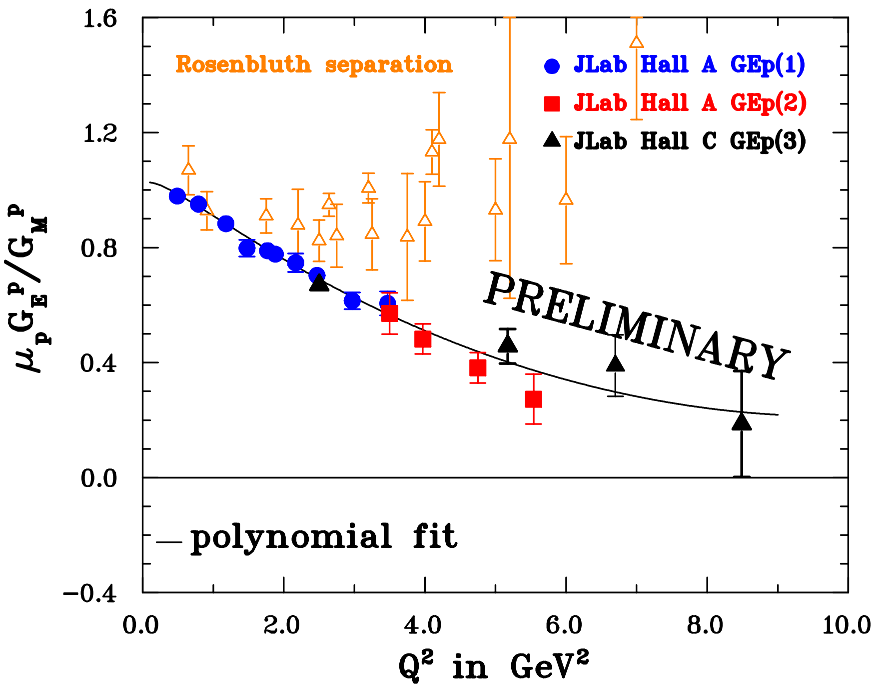

Figure 88: Results of GEp(1) (filled circles), GEp(2) (filled squares), and GEp(3) (filled triangles) experiments are shown as $\mu_p G_E^p / G_M^p$. The Rosenbluth separation data (empty triangles) are shown for comparison. The error bars on the data points are statistical only.

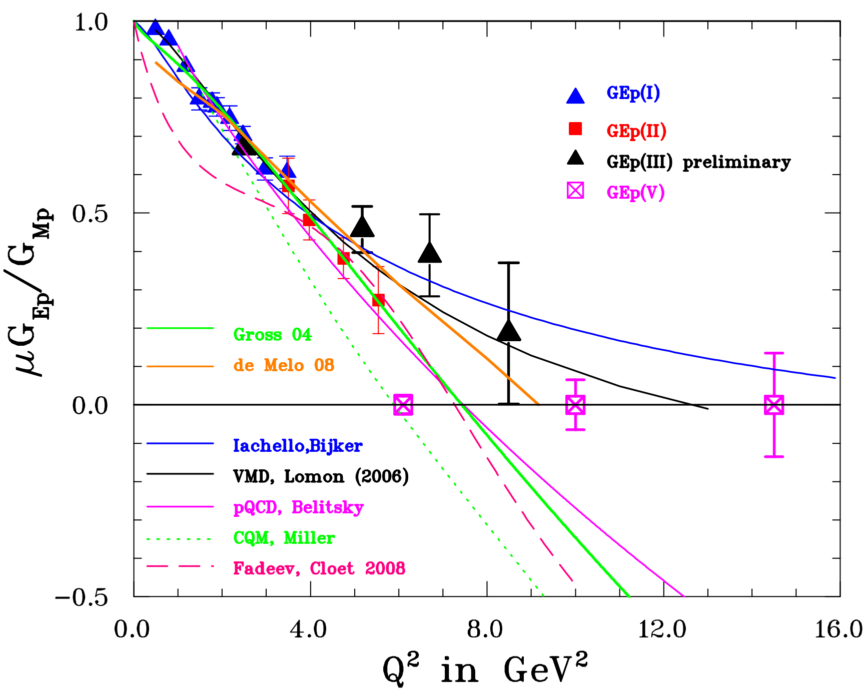

Figure 89: The published results of GEp(1) [4, 5], GEp(2) [6], preliminary results from GEp(3) [8] and the projected results of GEp(5) in a 60-day run [14] are shown here. Theoretical predictions are from Refs. [15, 16, 17, 18, 19, 20, 21]

.

Proton form factors ratio, GEp(5): E12–07–109

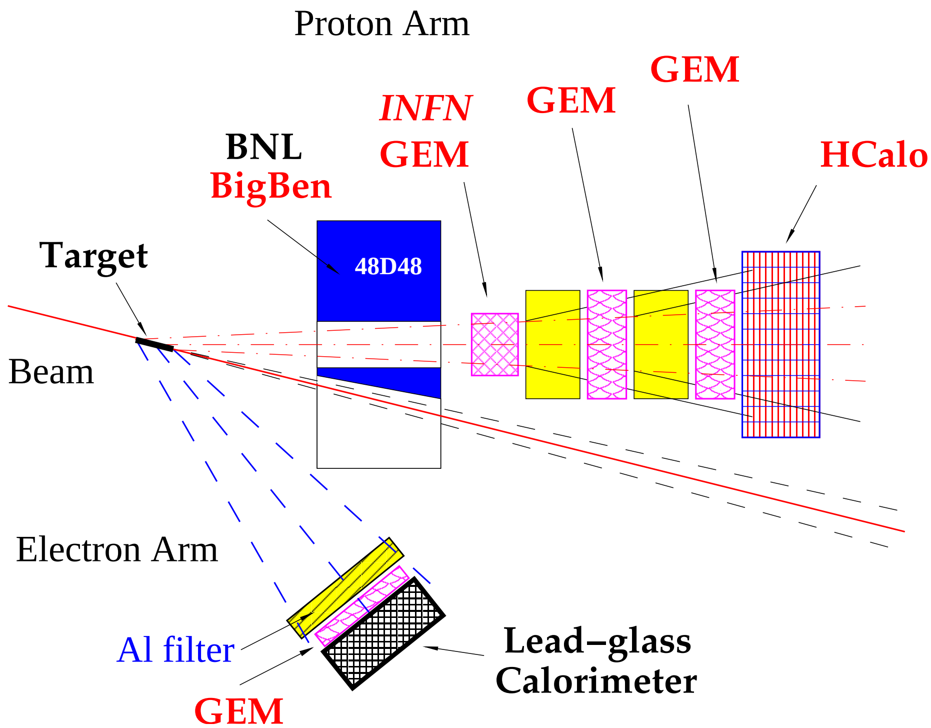

Figure 90: A schematic but scaled representation of the set-up that will be used for GEp(5) (E12-07-109). The proton arm (set at a central scattering angle of 12°) incorporates a double polarimeter instrumented with GEM trackers and a highly-segmented hadron calorimeter. The electron arm uses the existing "BigCal" electromagnetic calorimeter based on lead glass.

The measurement of the ground-state electromagnetic form factors of the proton becomes quite challenging at high momentum transfers, because the effective rate drops as roughly E^2_{beam}/Q^{16}. The polarization-transfer method also requires very large statistics because of the relatively low analyzing power of the recoil polarimeter. The GEp(5) experiment meets these challenges through an innovative approach. The spectrometer in the proton arm is based on a large open-geometry dipole magnet that is placed quite close to the target, and at a small angle, a configuration that provides large solid angle. The placement of the dipole at small angle is made possible by incorporating a cut in the magnet yoke for the beam line. The spectrometer will also be equipped with a double focal-plane polarimeter (FPP), instrumented with gas electron multiplier (GEM) trackers, that provides improved efficiency, and a highly-segmented hadron calorimeter which will be part of the trigger and will help reduce the event rate. The electron will be detected in coincidence by an existing electromagnetic calorimeter, "BigCal". It will also be equipped with a GEM tracker to further improve its position resolution. The GEp(5) experiment will use the 11 GeV polarized electron beam and a 40-cm long liquid hydrogen target [22].

3.12.3 The Super Bigbite apparatus

The Super-Bigbite apparatus will be used in GEp(5) as a large-acceptance spectrometer, a Super Bigbite spectrometer (SBS). The plan is based on an existing, resistive-coil dipole magnet, 48D48, available from Brookhaven National Laboratory. It will provide angular coverage up to ∼70 msr, with a detector package that will be capable of operating at the largest possible luminosity, almost 10^{39} electron/s×nucleon/cm^2. The use of a simple dipole placed close to the target allows one to achieve the high acceptance in the spectrometer. Such an installation is made possible by a deep cut through the iron yoke of the magnet for the beam line. The magnet deflects charged particles vertically and will be used with a field integral up to 2.5 T·m. The field in the beam line will be reduced to an acceptable level by specially developed magnetic shields. The relatively small bend angle is compensated for by the high coordinate resolution (70 μm) of the front GEM-based chambers resulting in a momentum resolution of $\sim 0.5\%$ at 8 GeV/c in GEp(5) with the 40-cm long LH_2 target. The GEM technology solves the main challenge of this spectrometer, the very high counting rates, allowing tracking at very high background rates. **These features, combined with target length of 40 cm will give SBS at least a factor of 10 advantage compared with any existing or proposed spectrometer at Jefferson Lab for nucleon form-factor measurements.**

The hadron calorimeter (HCalo), positioned at the end of the SBS detector package will be used to trigger the DAQ, in coincidence with the signals from the elastic electrons detected in the electromagnetic calorimeter (BigCal). In addition, these two calorimeters will provide coordinate information that will be used to locate the proton track in the front tracker and in the FPP trackers by applying kinematic constraints. The energy and coordinate resolutions of BigCal of about 5-7% and 7 mm, respectively, for 2.5 GeV electrons satisfy the trigger and tracking requirements. We expect 20% energy resolution and 2-cm coordinate resolution for 8 GeV protons in the hadron calorimeter [23].

The lead-glass blocks of the BigCal calorimeter will be rearranged in a matrix 20×75, a shape optimized for the largest acceptance at $Q^2 = 14.5$ GeV^2. The electronics for the calorimeter, including the custom-built summing modules, the HV supply, the FASTBUS ADC and TDC (which were used in the GEp(3) experiment) will be re-used in the GEp(5) experiment. BigCal will be installed 3 m from the target at a central angle of 39° (at the largest Q^2). It will be shielded from the target by a 20 cm Al plate to reduce the radiation dose on the lead glass. This also reduces the hit rate in the coordinate detector, a two-plane GEM-based chamber, placed in front of the BigCal.

The angular correlation between the scattered electron and the recoil proton will be measured very accurately, especially the angle between the electron scattering plane and the proton recoil plane. Because of the small size of the electron beam, the angles of the electron and of the recoil proton can be determined with a good accuracy of ∼0.5 mrad. This corresponds to a 5 MeV/c uncertainty in the perpendicular momentum balance. Such an uncertainty is much smaller than the typical out-of-plane momentum for inelastic events, 150 MeV/c, which results in a powerful suppression of the background. In order to achieve this, a 1 mm coordinate accuracy is required for the scattered electron which will be achieved by using the coordinate detector.

3.12.4 Updated kinematics of the measurements

Q^2 [GeV^2]	E_{beam} [GeV]	beam time [days]	p_p [GeV]	θ_{SBS} [deg]	E_e [GeV]	θ_{BigCal} [deg]	$\Delta[\mu G_E/G_M]$
optics	6.6	4		28.0			
5.0	6.6	1	3.48	28.0	3.94	26.3	0.023
10.0	8.8	10	6.20	16.7	3.47	35.3	0.065
14.5	11.	45	8.61	12.0	3.27	39.0	0.135

Table 14: The kinematics of the proposed data points.

Because of the importance of the *precise* measurements at high Q^2, we have decided to have one precise measurement at 14.5 GeV^2 (instead of two neighboring points at 13 and 15 GeV^2 as in the original proposal) and two points at about 5 and 10 GeV^2. This will be achieved by reducing the horizontal sizes of the detectors and thus, effectively reducing the Q^2-acceptance, but increasing the vertical sizes and the event rates per unit Q^2-interval, keeping the detector area and the number of channels the same.

The optimized acceptance and use of beam time provides more power to discriminate among different theoretical predictions, while keeping the same total beam time as in the original proposal. The kinematical quantities and anticipated errors for these points are summarized in Table 14. Including four days for optical and spin transport studies, we have in total 60 days of beam on target, as it was requested in the approved GEp(5) experiment E12-07-109.

3.12.5 Technical progress toward realizing the experiment

During the last several years significant efforts have been directed toward realization of the form-factor program in Hall A.

Collaboration and coordination: The proposal for this experiment was approved by PAC32 in August 2007. Understanding the importance of precise high-Q^2 measurements, the spokespersons of the two proton form-factor ratio experiments with 11 GeV beam, E12-07-109 and E12-09-001, decided to consolidate behind the GEp(5) experiment. Two new spokespersons were added to the E12-07-109 team and a coordinated plan of measurements was formulated.

In November 2008 the SBS project was reviewed by a technical committee. The Conceptual Design Report (CDR) and the technical review reports can be found in [23]. A funding proposal to DOE was submitted in November 2009 that will cover the whole experimental apparatus needed for all the nucleon form-factor experiments in the SBS physics program: E12-07-109, E12-09-016, and E12-09-019.

Funding of the project: In September 2007 the Italian institute INFN approved the development and construction of the front tracker for the Super Bigbite for the total amount of €720k. The request for SBS funding was submitted by the University of Glasgow group to the UK STFC for the amount of $200k.

The collaboration submitted a funding request [22] to DOE for the amount of $2.4M (detectors of the SBS project) and to JLab for the amount of $1.4M (the magnet and Hall A infrastructure).

Magnet design: The magnet configuration was analyzed with 3D field calculations [24]. The magnet will be used with an excitation current of 2 kA, which is half the nominal value of the original 48D48 magnet. Therefore, the cross section of the new coils cab be reduced. It was demonstrated that for the required main field along the central trajectory of 2.5 T·m, the field inside the beam line will have a transverse component below 200 Gauss, and its integral will be on the level of 0.005 T·m, which have very little effect on the 11 GeV beam and the background rate in the detectors of the SBS apparatus. The power supply of Q_{weak} will be used to energize the SBS magnet.

GEM chamber design and prototyping: The actual design of the GEM chamber is proceeding at INFN by the Roma group. Both the electronics and the GEM readout board for the 40×50 cm^2 unit are in the prototyping stage. All APV25 chips for processing the signals from the GEM strips required for the SBS trackers have already been purchased. In 2010 the actual size prototype GEM chamber will be tested in Hall A.

JLab in collaboration with the University of Glasgow has already constructed and tested small GEM chambers which were used for initial studies in Hall A. The UVa group is preparing two small chambers with readout electronics for use during the PREX experiment (Hall A, April 2010) in the HRS spectrometers.

Calorimeters: The existing lead-glass calorimeter BigCal was successfully used in four experiments in Hall C. The UV curing procedure that is planned to be used in the GEp(5) experiment was tested several times during these experiments. The detector will be re-stacked, increasing the vertical aspect ratio, but keeping the same number of channels and total area. The electron arm will be equipped with a two-plane GEM chamber in front of BigCal and behind a 20-cm Al absorber.

Collaboration with the Dubna group was organized for the design and construction of the hadron calorimeter. A Monte Carlo simulation of the HCalo calorimeter was performed for a few GeV protons, neutrons, and pions. The Monte Carlo simulation was also used to find the counting rate of the detector by using the DINREG event generator [25].

Simulations: New features were included in the simulation of the elastic events that made it possible to optimize the detector configuration.

Based on the results from the double polarimeter in the GEp(3) experiment, the scattering of the polarized protons in the analyzers was simulated and an analyzing power was assigned for each event. Thus, the polarimeter figure-of-merit, $FOM = \varepsilon(\theta) A_Y^2(\theta)$, where $\varepsilon(\theta)$ is the efficiency for a scattering angle θ and A_Y is the analyzing power, was calculated event by event and used to optimize the geometrical sizes of the detectors. We modified the geometrical sizes of the trackers and the two calorimeters to increase the elastic event rate per unit Q^2-interval. This was achieved by increasing the vertical to horizontal aspect ratio to about 3:1, which was possible after reconfiguring the coils of the magnet as explained above. Advanced simulation of the π° photoproduction, the main physical background, has been performed. It demonstrated that the detector resolutions will allow us to reduce this background to a few percent level.

Trigger configuration: A Flash ADC was developed by the JLab electronics group. It was used successfully for the Gas Cherenkov counter of the BigBite spectrometer and currently in the detector of the Möller polarimeter. We plan to implement 16 such FADCs in the readout of the hadron calorimeter. A detailed design of the trigger logic based on the FADC and FPGA logic was developed [23].

The polarimeter measurements at JINR: An experimental study of the analyzing power is under way at JINR (Dubna). It will be done with a 7-8 GeV/c polarized proton beam. A set of 25 hadron calorimeter blocks will be used for the triggering as in the GEp(5) experiment.

References

[1] A.I. Akhiezer *et al.*, JETP **33**, 765 (1957); Sov. J. Part. Nucl. **3**, 277 (1974).

[2] R. Arnold *et al.*, Phys. Rev. C **23**, 363 (1981).

[3] C.F. Perdrisat, V. Punjabi and M. Jones, "Electric Form Factor of the Proton by Recoil Polarization", Jefferson Lab experiment 89-014 and 93-027 (1993).

[4] M.K. Jones *et al.*, Phys. Rev. Lett. **84**, 1398 (2000).

[5] V. Punjabi *et al.* Phys. Rev. C **71** (2005) 055202.

[6] O. Gayou *et al.*, Phys. Rev. Lett. **88**, 092301 (2002).

[7] M.N. Rosenbluth, Phys. Rev. **79**, 615 (1950).

[8] C.F. Perdrisat, V. Punjabi, M.K. Jones, E. Brash, "Measurement of G_{Ep}/G_{Mp} to $Q^2 = 9$ GeV^2 via Recoil Polarization", Jefferson Lab experiment 04-108 (2004).

[9] L. Andivahis *et al.*, Phys. Rev. D **50** 5491 (1994).

[10] M.E. Christy *et al.*, Phys. Rev. C **70** 015206 (2004).

[11] I.A. Quatan *et al.*, Phys. Rev. Lett. **94** 142301 (2005).

[12] J. Arrington, Phys. Rev. C **69**, 022201 (2004).

[13] G.A. Miller, arXiv:0705.2409 (2007); and Phys. Rev. Lett. **99**, 112001 (2007).

[14] E. Brash, E. Cisbani, M. Jones, M. Khandaker, L. Pentchev, Ch. Perdrisat, V. Punjabi, B. Wojtsekhowski, "Large Acceptance Proton Form Factor Ratio Measurements at 13 and 15 (GeV/c)^2 Using Recoil Polarization Method", Jefferson Lab experiment E12-07-109 (2007).

[15] F. Gross and P. Agbakpe, Phys. Rev. C **73**, 015203 (2006).

[16] J. P. B. de Melo, T. Frederico, E. Pace, S. Pisano and G. Salme, Phys. Lett. B **671**, 153 (2009) [arXiv:0804.1511 [hep-ph]].

[17] R. Bijker and F. Iachello, Phys. Rev. C **69**, 068201 (2004).

[18] E.L. Lomon, Phys. Rev. C **64**, 035204 (2001), Phys. Rev. C **66**, 045501 (2002) and arXiv:nucl-th/0609020 (2006)..

[19] A.V. Belitsky, X. Ji and F. Yuan, Phys. Rev. Lett. **91**, 092003 (2003).

[20] M.R. Frank, B.K. Jennings, and G.A. Miller, Phys. Rev. C **54**, 920 (1996).

[21] I.C. Cloet and C.D. Roberts, arXiv:0811.2018 [nucl-th]

[22] "Electromagnetic Form Factors of the Nucleon using the 12-GeV CEBAF", C.W. de Jager *et al.*, Funding Proposal submitted to The United States Department of Energy, http://www.jlab.org/~bogdanw/EMFF.pdf

[23] The Super-Bigbite Spectrometer (SBS) Conceptual Design Report and SBS Technical review report can be found on the web-page
http://hallaweb.jlab.org/12GeV/SuperBigBite/SBS-CDR/

[24] S. Mikhailov and B. Wojtsekhowski, report given at "Magnet design workshop" at Particle Accelerator Conference, May 2009.

[25] P.V. Degtyarenko, M.V. Kossov, H-P. Wellisch, Chiral Phase Space Event Generator, Eur. Phys. J. A **8**, 217 (2000).

4 Hall A Collaboration Member List

Argonne National Lab
John Arrington
Frank Dohrmann
Paul Reimer

Budker Institute of Nuclear Physics
Dima Nikolenko
Igor Rachek

Cairo University
Hassan Ibrahim

California Institute of Technology
Steffen Jensen
Cathleen Jones

California State University
Konrad A. Aniol
Juan Carlos Cornejo
Martin B. Epstein
Dimitri Margaziotis

Carnegie Mellon University
Gregg Franklin
Megan Friend
Diana Parno
Brian Quinn
Luminita Todor

The Catholic University
Tanja Horn

China Institute of Atomic Energy (CIAE)
Xiaomei Li
XinHu Yan
Shuhua Zhou

College of William and Mary
David S. Armstrong
Todd Averett
Keith Griffioen
Joe Katich
Aidan Kelleher
Lubomir Pentchev
Charles Perdrisat
Bo Zhao

DAPNIA/SPhN
Etienne Burtin
Christian Cavata
Nicole d'Hose
Jean-Eric Ducret

Stephanie Escoffier
Bernard Frois
Sophie Kerhoas
David Lhuillier
Jacques Marroncle
Damien Neyret
Stephane Platchkov
Thierry Pussieux
Franck Sabatie
Antonin Vacheret
Pascal Vernin

Duke University
Steve Churchwell
Haiyan Gao
Calvin Howell
Min Huang
Xin Qian
Yi Qiang
Richard Walter
Qiujian Ye

Faculté des Sciences de Monastir (Tunisia)
Malek Mazouz

Florida International University
Armando Acha
Werner Boeglin
Luminiya Coman
Marius Coman
Hari Khanal
Laird Kramer
Pete Markowitz
Brian Raue
Joerg Reinhold

Fudan University
Xiaofeng Zhu

General Electric
Jianguo Zhao

Gent State University
Natalie Degrande
Luc Van de Hoorebeke
Robert Van de Vyver

Gesellschaft fur Schwerionenforschung (GSI)
Javier Rodriguez Vignote

Hampton University
Leon Cole
Ashot Gasparian
Peter Monaghan

Harvard Medical School
Hong Xiang

Harvard University
Richard Wilson

INFN/Bari
Raffaele de Leo

INFN/Catania
Vincenzo Bellini
Concetta Maria Sutera
Antonio Guisa
Francesco Mammoliti
Giuseppe Russo
Maria Leda Sperduto

INFN/Roma
Marco Capogni
Francesco Cusanno
Salvatore Frullani
Franco Garibaldi
Franco Meddi
Guido Maria Urciuoli
Evaristo Cisbani
Rachele di Salvo
Mauro Iodice

Institut de Physique Nucléaire
Louis Bimbot

ISN Grenoble
Serge Kox
Jean Mougey
Gilles Quemener
Eric Voutier

Jefferson Lab
Alexandre Camsonne
Larry Cardman
Jian-Ping Chen
Eugene Chudakov
Kees de Jager
Alexandre Deur
Ed Folts
David Gaskell
Javier Gomez
Ole Hansen
Douglas Higinbotham
Mark K. Jones
John Lerose
Bert Manzlak
David Meekins

Bob Michaels
Bryan Moffit
Sirish Nanda
Noel Okay
Lester Richardson
Yves Roblin
Arun Saha
Brad Sawatzky
Jack Segal
Dennis Skopik
Patricia Solvignon
Riad Suleiman
Stephanie Tysor
Bogdan Wojtsekhowski

Jozef Stefan Institute
Miha Mihovilovic
Simon S̃irca

Kent State University
Bryon Anderson
Mina Katramatou
Elena Khrosinkova
Elena Long
Richard Madey
Mark Manley
Gerassimos G. Petratos
Andrei Semenov
John Watson

Kharkov Institute of Physics and Technology
Oleksandr Glamazdin
Viktor Gorbenko
Roman Pomatsalyuk

Kharkov State University
Pavel Sorokin

Lanzhou University
Yi Zhang

Longwood University
Tim Holmstrom
Keith Rider
Jeremy St. John
Wolfgang Troth

Los Alamos Laboratory
Lei Guo
Xiaodong Jiang
Han Liu
Ming Xiong Liu
Andrew Pucket

LPC Clermont-Ferrand (France)
Pierre Bertin
Helene Fonvielle
Eric Fuchey
Florian Itard
Bernard Michel
Carlos Munoz Camacho

Mississippi State University
Dipangkar Dutta
Amrendra Narayan
Nuruzzaman Nuruzzaman

MIT
Bill Bertozzi
Shalev Gilad
Jin Huang
Vincent Sulkosky
Navaphon Tai Muangma
Kai Pan
Nikos Sparveris
Wang Xu
Xiaohui Zhan
Cesar Fernandez Ramirez

Negev Nuclear Research Center
Sharon Beck
Arie Beck

NIKHEF
Jeff Templon

Norfolk State University
Vina Punjabi

North Carolina Central University
Benjamin Crowe
Branislav (Branko) Vlahovic

Northwestern University
Issam Qattan
Ralph Segel

Ohio University
Julie Roche

Old Dominion University
Gagik Gavalian
Wendy Hinton
Jeff Lachniet
Larry Weinstein
Charles Hyde

Pacific Northwest National Lab
Kathy McCormick
Brian Milbrath

Princeton University
Ioannis Kominis

Regina University
Alexander Kozlov

Renaissance Tech
Robert Lourie
Joseph Mitchell
Paul Ulmer

Rutgers University
Lamiaa El Fassi
Ron Gilman
Gerfried Kumbartzki
Ronald Ransome

Saint Norbert College
Michael Olson

Seoul National University
Seonho Choi
Byungwuek Lee

Smith College
Piotr Decowski

St Mary's University
Adam Sarty
Jackie Glister

SUBATECH
Jacques Martino

Syracuse University
Zafar Ahmed
Richard Holmes
Abdurahim Rakhman
Paul A. Souder

Tel Aviv University
Nathaniel Bubis
Or Chen
Igor Korover
Jechiel Lichtenstadt
Eli Piasetzky
Ishay Pomerantz
Ran Shneor

Temple University
David Flay
Sebastian Incerti
Zein-Eddine Meziani
Matthew Posik
Elaine Schulte
Huan Yao

Tohoku University
Kouichi Kino
Kazushige Maeda
Teijiro Saito
Tatsuo Terasawa
H. Tsubota

Universidad Complutense de Madrid (UCM)
Joaquin Lopez Herraiz
Luis Mario Fraile
Maria Christina Martinez Perez
Jose Udias Moinelo

Università di Pavia
Sigfrido Boffi

Università La Sapienza (Rome)
Fulvio De Persio

University of Glasgow
John Annand
David Hamilton
Dave Ireland
Ken Livingston
Dan Protopopescu
Guenther Rosner

University of Illinois
Ting Chang
Areg Danagoulian
Alan Nathan
J.C. Peng
Mike Roedelbronn
Youcai Wang
Lingyan Zhu

University of Kentucky
Kalyan Allada
Dan Dale
Chiranjib Dutta
Tim Gorringe
Wolfgang Korsch
Piotr Zolnierczuk

University of Lund
Kevin Fissum

University of Maryland
Elizabeth Beise
Fatiha Benmokhtar
Herbert Breuer
George Chang
Nicholas Chant
Harry Holmgren
Philip Roos

University of Massachusetts, Amherst
Krishna S. Kumar
Dustin McNulty
Luis Mercado
Jon Wexler

University of New Hampshire
John Calarco
Greg Hadcock
Bill Hersman
Maurik Holtrop
Donahy John
Mark Leuschner
Sarah Phillips
Karl Slifer
Timothy Smith

University of Regina
Ed Brash
Garth Huber
George Lolos
Zisis Papandreou

University of Saskatchewan
Ru Igarashi

University of Science and Technology of China (USTC)
Yi Jiang
Hai-jiang Lu
Yunxiu Ye

University of South Carolina
Simona Malace
Mike Paolone
Steffen Strauch

University of Virginia
Khem Chirapatpimol
Brandon Craver
Mark Dalton
Xiaoyan Deng
Gordon D. Gates
Mitra Hashemi Shabestari
Ge Jin

Sudirukkuge Tharanga Jinasundera
Richard Lindgren
Nilanga Liyanage
Vladimir Nelyubin
Blaine Norum
Kent Paschke
Seamus Riordan
Oscar Rondon
Rupesh Silwal
Jaideep Singh
Ramesh Subedi
Kebin Wang
Diancheng Wang
Krishni Wijesooriya
Xiaochao Zheng
Jiayao Zhou

Lawrence Berkeley National Lab
Guy Ron

Yamagata University
Seigo Kato
Hiroaki Ueno

Yerevan Physics Institute
Nerses Gevorgyan
Edik Hovhannisyan
Armen Ketikyan
Vahe Mamyan
Samvel Mayilyan
Artush Petrosyan
Albert Shahinyan
Hakob Voskanian

Past Members
Mattias Anderson
Maud Baylac
Hachemi Benaoum
J. Berthot
Tim Black
Alexander Borissov
Vincent Breton
Zhengwei Chai
Pibero Djawotho
Kim Egiyan
Catherine Ferdi
Robert Feuerbach
Mike Finn
Oliver Gayou
Charles Glashausser
Brian Hahn
Riccardo Iommi
Stephanie Jaminion
Lisa Kaufman

James D. Kellie
Ameya Kolarkar
Norm Kolb
Kevin Kramer
Elena Kuchina
Serguei Kuleshov
Geraud Lavessiere
Antonio Leone
Meihua Liang
Justin McIntyre
Wilson Miller
Pierre Moussiegt
Roberto Perrino
Bodo Reitz
Rikki Roche
David Rowntree
Gary Rutledge
Marat Rvachev
Neil Thompson
Dan Watts
Jingdong Yuan
Jingdong Zhou

5 Publications

1. **"Virtual Compton Scattering and Neutral Pion Electroproduction in the Resonance Region up to the Deep Inelastic Scattering Region at Backward Angles"**
   Geraud Laveissière *et al.*
   Phys. Rev. C **79**, 015201 (2009), arXiv:0811.3867 [nucl-ex]

2. **"High Resolution Spectroscopy of $^{16}N_{\Lambda}$ by Electroproduction"**
   F. Cusanno *et al.* [Jefferson Lab Hall A Collaboration]
   Phys. Rev. Lett. **103**, 202501 (2009), arXiv:0810.3853 [nucl-ex]

3. **"Performance of the Two Aerogel Cherenkov Detectors of the JLab Hall A Hadron Spectrometer"**
   S. Marrone *et al.*
   Nuovo Cim. **124B**, 99 (2009), arXiv:0810.4630 [physics.ins-det]

4. **"Proton Polarimeter Calibration between 82 and 217 MeV"**
   J. Glister *et al.*
   Nucl. Instrum. Meth. A **606**, 578 (2009), arXiv:0904.1493 [nucl-ex]

5. **"Hard Photodisintegration of a Proton Pair"**
   I. Pomerantz *et al.* [JLab Hall A Collaboration]
   Phys. Lett. B **684**, 106 (2010), arXiv:0908.2968 [nucl-ex]

6. **"Cross sections and Rosenbluth separations in 1H(e, e'K^+)Lambda up to Q2=2.35 GeV2"**
   M. Coman *et al.*
   submitted to Phys. Rev. C, arXiv:0911.3943 [nucl-ex]

7. **"Update of High Resolution (e,e'K^+) Hypernuclear Spectroscopy at Jefferson Lab's Hall A"**
   F. Cusanno *et al.*, arXiv:0911.4930 [nucl-ex]

6 Theses

1. Jackie Glister, *"Polarization Observables in Low Energy Deuteron Photodisintegration"* St. Mary's University & Dalhousie University

2. Michael Paolone, *"Polarization Transfer in* $^4He(\vec{e},e'\vec{p})^3H$*"* University of South Carolina

3. Jonathan Miller, *"Measurement of the Electric Form Factor of the Neutron at High Momentum Transfer"*, University of Maryland, November, 2009

4. Aidan Kelleher, *"A Measurement of the Neutron Electric Form Factor at Very Large Momentum Transfer Using Polarized Electrons Scattering from A Polarized Helium-3 Target"*, College of William and Mary, December, 2009

5. Albert Shahinyan, *" The Detector Systems for Investigation of the Parton Structure of the Nucleons"*, Yerevan Physics Institute, October, 2009

6. Byungwuek Lee, *"New Precision Measurements of Deuteron Structure Function A(Q) at Low Momentum Transfer"*, Seoul National University